Theory of Excitation Energy Transfer in Pigment-Protein Complexes

DISSERTATION

zur Erlangung des akademischen Grades des

Doktors der Naturwissenschaften

(Dr. rer. nat.)

eingereicht am

Fachbereich Biologie, Chemie, Pharmazie

FREIE UNIVERSITÄT BERLIN

vorgelegt von

Dipl.-Phys. Julian Adolphs

aus Düsseldorf

März 2008

1. Gutachter: Prof. Dr. Ernst-Walter Knapp, FU Berlin
2. Gutachter: Dr. habil. Volkhard May, HU Berlin

Disputation am 20.05.2008

Contents

Introduction

The main challenge of the 21st century is the solution of the worlds energy problem. Amazingly in every hour more solar energy hits the surface of the earth, than the human population of the earth consumes in one year. The direct conversion from light energy to electric energy (photovoltaics) unfortunately has a relatively low energy efficiency (6 % to 18 %), and the conventional solar cells are relatively expensive due to the high production effort. A cheaper alternative to the silicon photovoltaics might be organic solar cells in the future. The process with nearly 100 % quantum efficiency[1] is the approach used by plants, bacteria and algae. Although it still might be a long way to a technical adaptation of photosynthesis[2], it is a fascinating process, created and optimized by evolution over more than 2 billion years. In photosynthesis energy from the sunlight is converted to chemical energy (Fig 1). The photons of the sunlight are absorbed by so-called antenna pigments (chlorophylls, bacteriochlorophylls and carotenoids) and the excitation energy is transferred to the photosynthetic reaction center, where transmembrane charge transfer reactions are driven. In the oxygenic photosynthesis water is used as an electron source and the electron transfer is accompanied by proton gradients, which drive the production of ATP (Adenosine triphosphate), the universal energy currency, from ADP (Adenosine diphosphate). In this way light energy is converted to chemical energy. As a by-product of the water-fission, oxygen is released, which forms a basis of our life. The oxygenic photosynthesis is performed by higher plants, algae and cyanobacteria. The water splitting of oxygenic photosynthesis requires a relatively high redox potential, which is achieved with two reaction centers connected in series. These two reaction centers are called photosystem I and II (PSI and PSII). Both photosystems receive energy from antenna pigments or from direct optical excitation. PSII is the first one in the serial connection and it is the water splitting part while PSI is the second part and the one where the proton gradient drives the NADP+ to NADPH synthesis. The well known overall reaction scheme for the oxygenic photosynthesis reads:

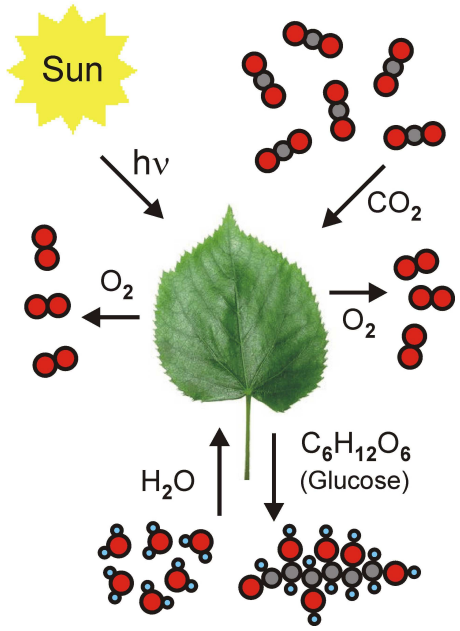

Figure 1: Cartoon of photosynthesis.

$$6\ CO_2 + 12\ H_2O \xrightarrow{h\nu} C_6\,H_{12}\,O_6 + 6\ O_2 \tag{1}$$

where $h\nu$ is the energy of a photon with frequency ν and h is Planck's constant and $C_6\,H_{12}\,O_6$ is the

[1] The quantum efficiency is the fraction of absorbed photons that engage in photochemistry. The energy efficiency is a measure of how much energy in the absorbed photons is stored as chemical products. In photosynthesis about a fourth of the energy of each photon is stored, hence the energy efficiency is around 25 % [1]. .

[2] $\varphi\bar{\omega}\varsigma$, $ph\bar{o}s$ = light; $\sigma\acute{\upsilon}\nu\theta\varepsilon\sigma\iota\varsigma$, $s\acute{y}nthesis$ = composition.

chemical formula for glucose. Another, in the sense of evolution older process[3] , is the anoxygenic photosynthesis, performed by anaerobic bacteria, such as green sulfur bacteria. In contrast to the organisms performing oxygenic photosynthesis, they have only one reaction center. It is called bacterial reaction center (bRC) and is structurally similar to PSI. It is able to oxidize hydrogen sulfide (H_2S) and similar compounds. Its overall reaction scheme reads:

$$CO_2 + 2\ H_2S \xrightarrow{h\nu} CH_2O + 2S + H_2O \tag{2}$$

where CH_2O is the chemical formula of formaldehyde. Although the overall scheme of the primary photosynthetic reaction is well understood, the molecular mechanisms are still unclear in many cases. A combined approach by high-resolution structure determination, optical spectroscopy and theory is necessary to understand the building principles of photosynthetic systems and how function and structure of these nano-machines are related. This progress was initiated by the first high-resolution X-ray structure (2.8 Å) determination of a photosynthetic pigment-protein complex by Fenna and Matthews in 1975 [2]. In 1988 the Nobel Prize in chemistry was awarded to Deisenhofer, Huber and Michel for the determination of the first three-dimensional structure of a photosynthetic reaction center [3], namely the reaction center of the purpur bacteria *Rhodopseudomonas viridis*, which performs anoxygenic photosynthesis.

[3]The ability to convert light energy into chemical energy is a huge advantage in evolution. Photosynthesis came up very early in the history of life on earth, which began around 3.5 billion years ago. Oxygenic photosynthesis arose approximately 2 billion years ago, as geological evidence suggests. Anoxygenic photosynthesis came up even earlier.

Chapter 1

Photosynthetic Pigment – Protein Complexes

The first step of photosynthesis is the capture of light by a grid of protein bound pigments. These pigment-protein complexes are therefore termed light-harvesting complexes or antenna complexes.

In 1932 Emerson and Arnold [4] estimated from experiments investigating the oxygen production efficiency of algae that only a tiny fractional amount (less than 0.05 %) of the pigments contributes directly to the photochemical reactions. Antenna pigments transfer excitation energy with high quantum yield to the reaction centers, where it is used to drive charge transfer or, more generally, to drive chemical reactions, which store the light energy in chemical form. To channel the excitation energy flow in a defined direction, there has to be an energetic sink, i.e., pigments in the target region must have lower absorption energies than the initially excited pigments. Unfortunately, the idea of energy transfer in analogy of water flowing downhill is too simple. A precondition for energy transfer is the existence of excitonic couplings, due to Coulomb interactions, between local excited states. These couplings cause the excited states of the pigment-protein complex to be delocalized, i.e., the exciton state wave function contains contributions of a number of pigments of the complex. Adjusted energy transport follows from energetic relaxation, transferring population between exciton states of different spatial extends. Because the latter depends crucially on excitonic couplings and local transition energies, also the excitation energy transfer of the light harvesting system depends on them.

Figure 1.1: Antennas collect signal of low density and concentrate it on a central acceptor.

The pioneering work of biochemists and crystallographers has resulted in high resolution crystal structure data of membrane proteins of astonishing size containing some ten thousands of atoms. Among the largest pigment-protein complexes are those of photosystem I [5] and photosystem II [6, 7]. These structures open the way for an understanding of the molecular mechanisms of complex reaction schemes like light-harvesting and primary charge separation in photosynthesis. A challenging question that should eventually be answered with these structures is how proteins succeed in functionalizing the same type of cofactor in different ways. Whereas chlorophylls act as light harvesting pigments in the antennae, they perform charge transfer in the reaction center. Clearly, the inter-pigment distances are important, but also the tuning of the optical and electrochemical properties of the pigments by their protein environments.

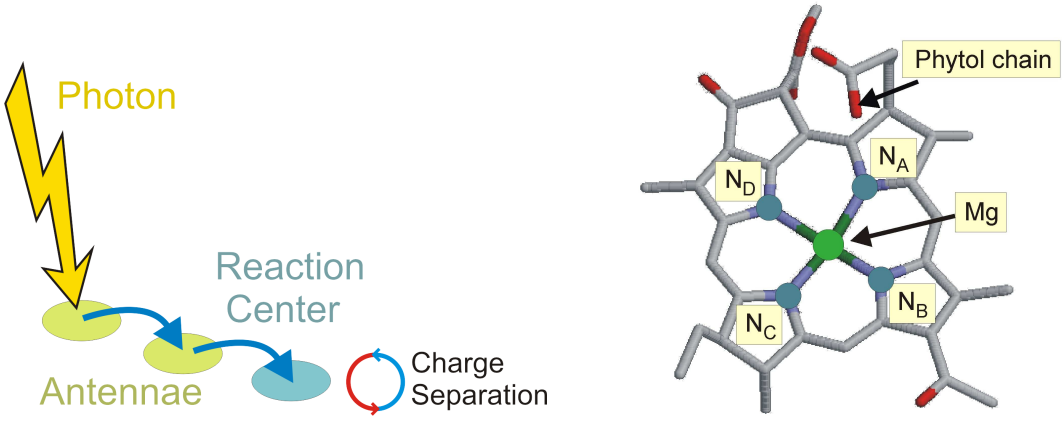

Figure 1.2: (*Left*) Cartoon of excitation energy transfer: Initially excitation event and the subsequent energy transfer to the reaction center, where the charge separation takes place. (*Right*) Sketch of a BChl*a* molecule (the phytyl chain is truncated at the marked position in the figure). Color code: Magnesium *green*, Oxygen *red*, Carbon *grey*, Nitrogen *blue*. The four Nitrogen atoms are labeled according to the standard nomenclature.

The underlying molecular mechanisms are far from being understood, even for small proteins. For the latter, there is a chance to obtain the relevant information about the local optical properties (site energies) of cofactors by a fit of optical spectra. These fits provide a critical test for any method that uses a direct calculation based on the structural data. An important system in this respect is the FMO protein [8, 9] which acts as a mediator of excitation energy between the outer antenna system, i. e., the chlorosomes [10], and the reaction center complex [11].

1.1 Pigments

The most important photosynthetic pigments are chlorophyll *a* (Chl*a*), occurring in green plants, oxygen producing algae and cyanobacteria, and bacteriochlorophyll *a* (BChl*a*), occurring in anaerobic bacteria. The name chlorophyll is derived from Greek: *chloros* = green and *phyllon* = leaf. Chl*a* absorbs most strongly in the blue and red, but poorly in the green part of the electromagnetic spectrum. This is the origin of the green color of chlorophyll containing tissues like plant leaves.

(Bacterio)chlorophyll is a chlorin pigment, which is structurally similar to other porphyrin pigments such as heme, appearing for instance in hemoglobin, the oxygen-transporting metallo-protein in red blood cells. In the case of Chl/BChl, at the center of the chlorin ring a magnesium ion is located (Fig 1.2, *right*), in contrast to an iron ion in the case of heme. The chlorin ring can have several different side chains, usually including a long phytyl[1] chain.

There are a few different forms that occur naturally: in all oxygen producing organisms Chl*a* is present, furthermore Chl*b* in higher plants and green algae, Chl*c* in various algae [12] and Chl*d* in *Acaryochloris marina* [13].

BChl*a* is present in most anoxygenic bacteria, BChl*b* in purple bacteria, BChl*c* and *d* in green bacteria, BChl*e* in brown bacteria and BChl*g* in heliobacteria [12]. These pigments absorb at different energies to increase the absorption cross section and to form an energy funnel for the transition energy from the antenna pigments towards the reaction center. Carotenoids contribute to the stability of pigment-protein complexes, are also able to act as photo protector via quenching of chlorophyll triplet states, i.e., they prevent formation of destructive singlet oxygen, and participate in light harvesting [14, 15]. Bacteriochlorophyll and chlorophyll pigments *in vivo* are protein bound. Depending on their function,

[1] Phytyl is a natural linear diterpene alcohol. It is an oily liquid that is nearly insoluble in water, but soluble in most organic solvents. Its chemical formula is $C_{20}H_{40}O$.

their optical spectra can differ substantially from those of the isolated molecules in solution.

The reaction center, where the charge separation takes place, is composed either of Chl*a* (higher plants, algae, cyanobacteria) or BChl*a* (anoxygenic bacteria). However, the major part of Chls/BChls (more than 99.5 %) acts as light absorbing antennas, funneling excitation energy to the reaction center. The antenna pigments serve to increase the absorption cross section of the RC.

1.1.1 Electronic Structure

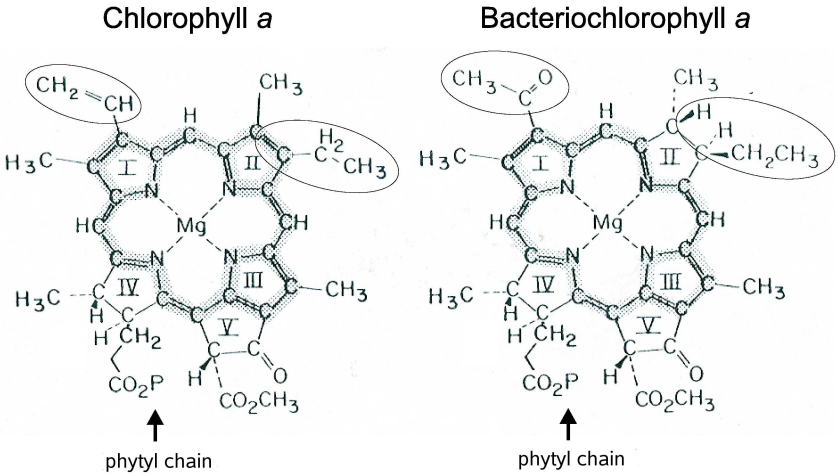

Figure 1.3: Chlorophyll *a* (*left*) and Bacteriochlorophyll *a* (*right*). The gray areas mark the cyclic π-electron system. The ellipses mark the positions where Chl*a* and BChl*a* differ. Figure (except ellipses) from Hanson [16].

The optical properties of pigments are determined by the extended conjugated π-electron systems of the tetrapyrrole[2] ring system. The strong optical transitions of Chl and BChl are due to $\pi \rightarrow \pi^*$ transitions.

According to the four-orbital model of Gouterman [17] the optical transitions of Chls/BChls arise from linear combinations of one electron promotions between the two highest occupied (HOMO-1 and HOMO) and the two lowest unoccupied (LUMO and LUMO+1) π-molecular orbitals. Gouterman explained the orthogonally polarized Q-bands Q_y (S_1) and Q_x (S_2) of the optical spectra as subtractive combination of the one electron promotion, while an additive combination defines the high energetic Soret band. The electronic π-system of Chls/BChls can be thought as a disturbed ideal tetrapyrrole π-system. The destabilization of the π-system arises from the saturation of pyrrol rings (ring IV for Chl, and rings II and IV in the case of BChls). By this saturation the initial degeneracy of the two one-electron promotions is destroyed, and a gain of oscillator strength of the subtractive combination at the expense of the additive is induced. Actually the observed Q_y-transition of BChl is stronger than that of Chl[3]. Furthermore, the four orbital model is also capable to explain the red shift of the Q_y-transition. With the help of quantum chemical calculations [16] it was possible to verify Gouterman's model, also for triplet states, which arise (according to Gouterman) from HOMO $\rightarrow$ LUMO transitions. For Chl*a*, the energy of the first triplet state T_1 is below the lowest excited singlet $Q_y(S_1)$ -state.

[2]Tetrapyrroles are compounds containing four pyrrole rings. Pyrrole is an aromatic organic compound, arranged in a pentagon with the chemical formula C_4H_5N.

[3]In Knox & Spring [18] the following vacuum dipole strengths of Q_y transitions in Chl/BChl were determined. BChl*a*: 37.1 D^2, Chl*a*: 21.0 D^2, Chl*b*: 14.7 D^2.

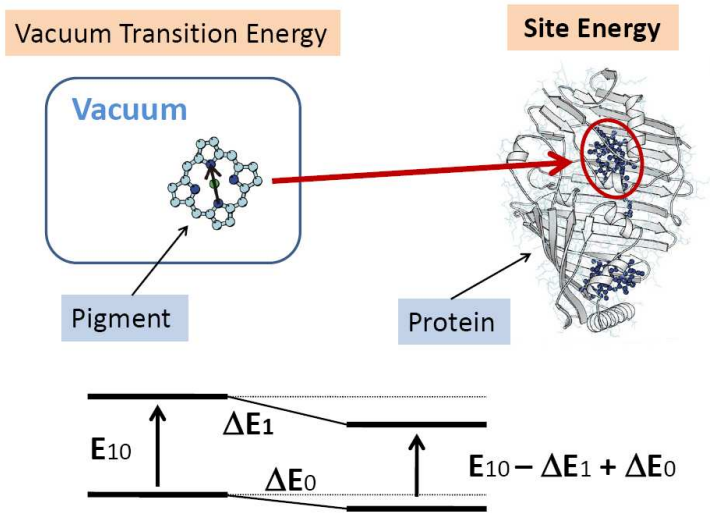

Figure 1.4: The vacuum transition energy of a pigment is changed by the local protein environment to its local transition energy (*site energy*).

1.1.2 Influence of the Environment

Pigments that are located in pigment protein complexes have shifted transition energies. These shifts have two origins: (i) the Coulomb interaction between pigments and (ii) the interaction with the protein surrounding. The change in transition energy caused by the Coulomb interactions between transition densities of the pigments is termed excitonic shift. To differentiate these excitonic shifts from shifts induced by the individual protein surrounding, the term *site energies* is introduced. The site energies are the transition energies of pigments in their local protein environment, assuming vanishing excitonic couplings. Site energies can not directly be measured, because the excitonic couplings cannot be turned off during the measurement. The site energies are sensitive to charged amino acid groups, hydrogen bonds, Mg-ligation and deformation of the pigment macrocycle.

1.2 Proteins

The word protein originates from the Greek $\pi\rho\bar{\omega}\tau o\varsigma$ (*protos*), which means *of primary importance*. These molecules were first described and entitled by the Swedish chemist Jöns Jakob Berzelius in 1838. However, the central role of proteins in organisms was not fully acknowledged until 1926, when James B. Sumner showed that the enzyme *urease* was a protein [19]. The first protein sequence was determined for *insulin*, by Frederick Sanger, who achieved the Chemistry Nobel Prize in 1958 for his work on the structure of proteins, especially that of insulin. The first protein structures were determined in 1958 for hemoglobin by Max Perutz [20] and myoglobin by Sir John Cowdery Kendrew [21], by X-ray diffraction analysis. To both scientists the 1962 Nobel Prize in Chemistry was awarded for these investigations.

Proteins are large organic compounds composed of amino acids. The amino acids form linear chains and are connected by peptide bonds between the carboxyl and amino groups of neighboring amino acid residues. The amino acid sequence of a protein is determined by a gene and encoded in the genetic code. Although the genetic code specifies only 20 natural amino acids, a large variety of proteins with many specific functions appear in nature. A still unsolved problem is the prediction of protein structures, based on the protein sequence. Reliable structure prediction would be extremely beneficial, because the determination of the sequence is relatively easy, while the crystallization, which is a precondition for the X-ray structure analysis, is a very difficult and time consuming process, as well as the X-ray analysis. For small proteins molecular dynamics is a suitable and successful structure prediction method, for large

proteins due to calculation effort, other methods like neural networks have to be enhanced.

In photosynthetic antennas, pigments are attached to the protein, which often has been called a scaffold which holds the pigments in a proper position. But the protein part of pigment protein complexes is much more than only a static scaffold, it also accepts the spare energy that is dispensed during excitation relaxation and its fast dynamics (in comparison to typical optical transition times) is important for the energy transfer through the antenna pigments towards the reaction center. The slow dynamics of the protein causes static disorder of the site energies: the site energies fluctuate slowly (compared to the optical transition times) around their mean value, hence the absorption lines are broadened. Such a thermal broadening can typically be described by a Gaussian distribution function and is termed inhomogeneous line width.

1.3 The FMO Complex of Green Sulfur Bacteria

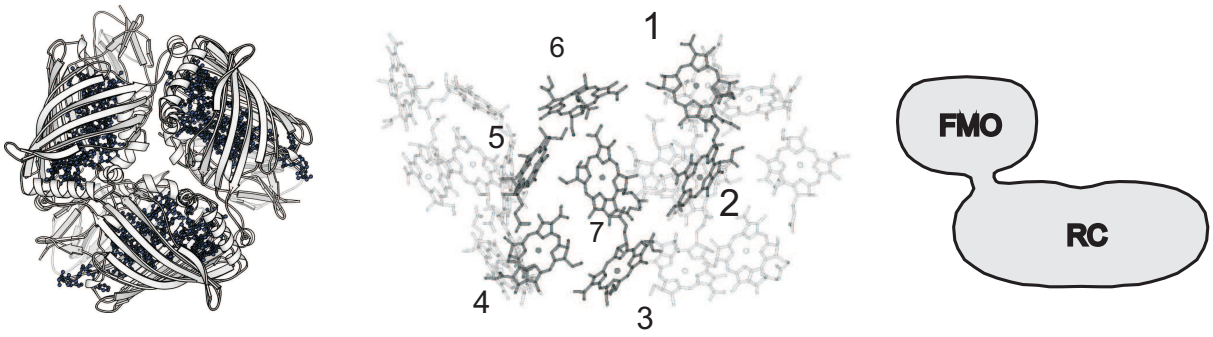

Figure 1.5: (*Left*) Sketch of the FMO trimer, the symmetry axis is perpendicular to the paper plane. (*Center*) FMO trimer with the symmetry axis in the paper plane. One monomer is highlighted and numbered according to Fenna & Matthews [2]. (*Right*) Sketch of the mutual arrangement of the FMO complex and the reaction center, as obtained from an electron-microscopic study [11, 22]. The orientation of the FMO complex is the same as in the *Center*.

The Fenna-Matthews-Olson (FMO) protein, is a water soluble complex and was the first pigment-protein complex that could be crystallized and analyzed by X-ray spectroscopy in 1975 by Fenna & Matthews [2]. Meanwhile the resolution of the electron density map has been refined to 1.9 Å by Tronrud *et al.* [23] for the FMO complex of *Prosthecochloris aestuarii* and to 2.2 Å for the structure of *Chlorobium tepidum* by Li *et al.* [24]. The structure of the FMO complex has a 3-fold rotational symmetry, i.e., it is a trimer (Fig 1.5, *left*). Each of the three monomers contains seven BChl*a* molecules, as shown in Fig 1.5 (*center*). The BChl*a* molecules are bound to the protein by ligation of their central magnesium atom to histidine, leucine or water bridged oxygen atoms. The original numbering (Fig 1.5, *center*) of the BChls, chosen by Fenna & Matthews, is used throughout this work. The FMO complex appears in green sulfur bacteria and mediates the transfers of excitation energy between the chlorosomes[4], which are the main light-harvesting antennae of green sulfur bacteria, and the membrane-embedded bacterial reaction center (Fig 1.5 (*right*) and Fig 1.6). This energy transfer from the antennas to the reaction center is controlled by the protein with systematic changes of the local optical transition energies (site energies) of the pigments. The determination of these site energies was a problem with partly contradictory solutions for about 30 years.

The FMO-complex of green sulfur bacteria represents an important model protein for the study of elementary pigment-protein couplings, because it is one of the simplest antenna protein complexes, ap-

[4]Large photosynthetic antenna complex found in green sulfur bacteria. They are ellipsoidal bodies, their length is around 100 to 200 nm, width of 50 to 100 nm and height of 15 to 30 nm. They are mostly composed of BChl (*c*, *d*, or *e*) with small amounts of carotenoids and quinones surrounded by a galactolipid monolayer.

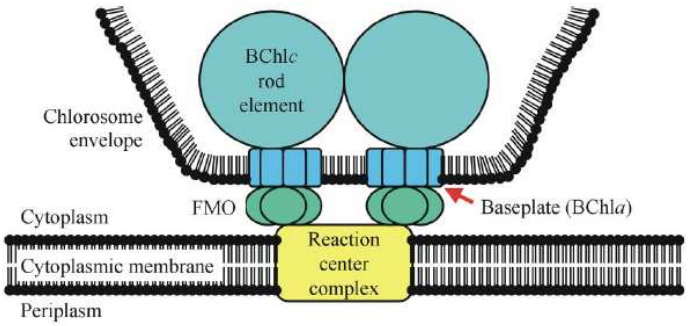

Figure 1.6: Schematic representation of the location of the FMO protein in the photosynthetic apparatus of green sulfur bacteria according to the most recent models [10, 25]. Figure created by Frank Müh [26].

pearing in nature. Furthermore the resolution of 1.9 Å [23] is the highest resolution achieved so far for a pigment-protein complex, and there are many spectroscopic data available from various experiments.

Methods developed on the relatively simple FMO protein will be applied to more complex systems, like photosystem I.

1.4 The Photosystem I of Green Plants

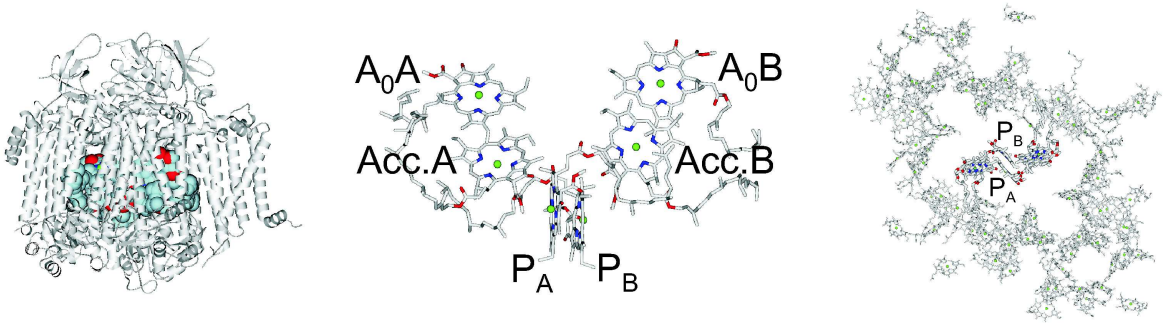

Figure 1.7: (*Left*) Sketch of the monomeric PSI complex of *S. elongatus*, sight nearly parallel to the thylakoid membrane, in grey the protein is shown while the six core complex pigments are colored. (*Center*) Details of the six core complex pigments. (*Right*) Spatial arrangement of all 96 pigments of one monomeric PSI unit.

The conversion from light energy to chemical energy in plants, green algae and cyanobacteria is driven by two cooperating large pigment protein complexes, namely photosystem I and II, which are both located in the thylakoid membrane, Fig 1.8.

The concept of the existence of two photosystems came up in the late 1950s to explain the so-called Emerson-Effect [27]: If single-cell algae or isolated chloroplasts are en-lighted by monochromatic light of either 680 or 700 nm, the sum of the two resulting photosynthetic rates (O_2 production) is significantly smaller than the resulting rate if both monochromatic lights are switched on at the same time. This result can be explained by assuming two photosystems with reaction centers absorbing at specific wavelengths. Only if both systems work to full capacity, the maximum photosynthetic rate can be reached. If the system is en-lighted solely at either 680 or 700 nm, holdup in the electron transport chain results and the photosystem cannot work optimal.

The reason for the name *photosystem I* (PSI) is due to the fact that PSI was discovered earlier than PSII, it does **not** reflect the order of the electron flux. The main steps of the chemical energy storage are carried out by four protein complexes: PSII, cytochrome b_6f, PSI and ATP synthase. These membrane

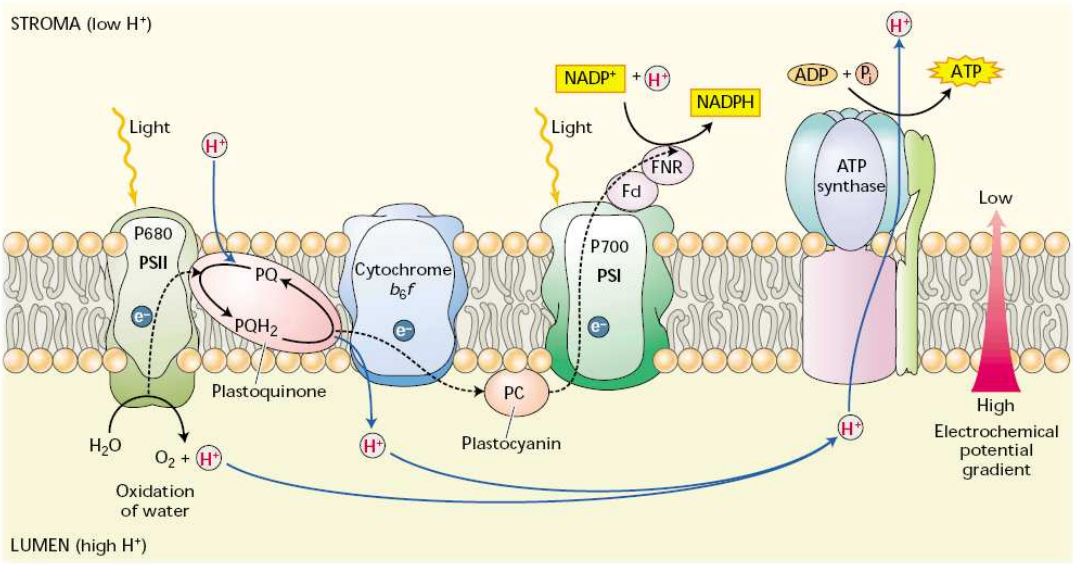

Figure 1.8: The electron and proton transfer in the thylakoid membrane is carried out vectorially by four protein complexes. Water is oxidized and protons are released in the lumen by PSII. PSI reduces $NADP^+$ to NADPH in the stroma, by the action of ferredoxin (Fd) and the flavoprotein ferredoxin-NADP reductase (FNR). Protons are also transported into the lumen by the action of the cytochrome b_6f complex and contribute to the electrochemical proton gradient. These protons diffuse to the ATP synthase enzyme, where their diffusion down the electrochemical potential gradient is used to synthesize ATP in the stroma. Reduced plastoquinone (PQH_2) and plastocyanin transfer electrons to cytochrome b_6f and to PSI, respectively. Dashed lines: electron transfer. Solid lines: proton movement. Figure from the book *Plant Physiology* [1].

complexes are oriented in the thylakoid membrane as shown in Fig 1.8 and function as described in the following (see also Fig 1.9):

- PSII oxidizes water to O_2 in the lumen and delivers protons into the lumen.
- Cytochrome b_6f grasps electrons from PSII and releases them to PSI. Additionally, it conveys protons from stroma into lumen.
- PSI reduces $NADP^+$ to NADPH in the stroma with the help of ferredoxin (Fd) and the flavoprotein ferredoxin-NADP reductase (FNR).
- ATP synthase generates ATP while protons diffuse back through it from the lumen into the stroma.

The PSI referred to throughout this work is the recently determined 2.5 Å structure of the thermophilic cyanobacterium *Synechococcus elongatus*, determined in 2001 by Jordan *et al.* [5] in cooperation of the *Freie Universität Berlin* and *Technische Universität Berlin*.

The PSI protein exists as a trimer and has a relative molecular mass of 3×356 kDa. For the 96 chlorophylls, position and orientation of the chlorophyll head groups were determined, leading to the mapping of the orientation of the Q_x and Q_y transition dipole moments.

1.5 Excitation Energy Transfer Mechanisms

In a simple excitation energy transfer reaction an electronic excitation is transfered between two pigments. In the initial state $|A\rangle = |A_{ex}\, B_{gr}\rangle$ pigment A is excited and pigment B is in its ground state. In the final state $|B\rangle = |A_{gr}\, B_{ex}\rangle$ the excitation was transferred from pigment A to pigment B. There are two possible mechanisms for this radiationless excitation transfer: Förster-transfer [28] (Fig 1.10,

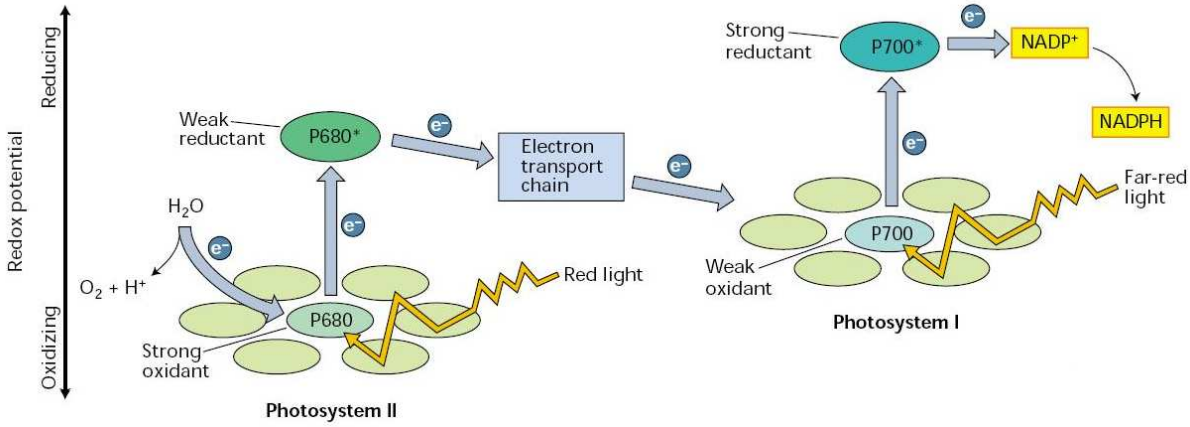

Figure 1.9: Simplified *Z-scheme* of photosynthesis. Red light absorption by photosystem II (PSII) produces a strong oxidant and a weak reductant. Far-red light absorption by PSI produces a weak oxidant and a strong reductant. The strong oxidant generated by PSII oxidizes water, the strong reductant produced by PSI reduces $NADP^+$. This scheme is basic to an understanding of photosynthetic electron transport. P680 and P700 refer to the (maximum) absorption wavelength (nm) of the reaction center chlorophylls in PSII and PSI, respectively. Figure from the book *Plant Physiology* [1].

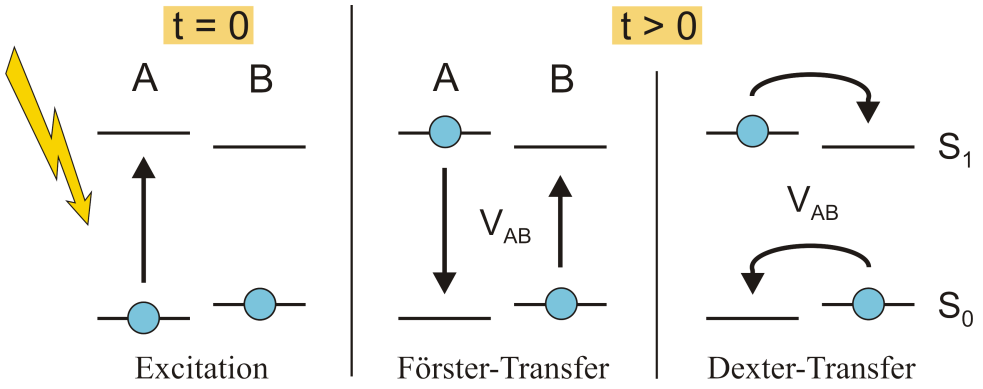

Figure 1.10: The two excitonic coupling mechanisms (Förster and Dexter) are illustrated. At time $t = 0$ (*left*) an excitation occurs, at time $t > 0$ either Förster transfer (*center*) or, Dexter transfer (*right*) takes place.

center) where the energy is transfered by Coulomb coupling between the transition densities of pigment A and pigment B and Dexter-transfer [29] (Fig 1.10, *right*), where two electrons are exchanged between A and B. If the distance between the pigments is much larger than their extensions, only Förster transfer takes place and contributions from Dexter transfer are negligible, since the latter relies on wavefunction overlap and therefore depends exponentially on distance. For pigments in close proximity, for example in the special pair, Dexter couplings need to be included to explain experimental results.

Chapter 2

Theory of Optical Spectra

Since atom coordinates of pigment-protein complexes are available from high-resolution X-ray spectroscopy (see chapter **Introduction**) it is possible to calculate structure based optical spectra, and to compare them with measured optical spectra. A realistic theory has to describe two quantities: The coupling between pigments (pigment-pigment coupling, Fig 2.1, *left*) and the coupling between each pigment and the protein (pigment-protein coupling, Fig 2.1, *right*). Unfortunately both coupling strengths are in the same range, which is a challenge for theory. In standard theories one uses perturbation theory for one of the two types of couplings, resulting in Förster theory of excitation energy transfer and Kubo/Lax theory of optical spectra in the case of weak inter-pigment couplings and Redfield theory for transfer and spectra for strong pigment-pigment coupling. The present theory of optical spectra (Renger & Marcus [30]) includes both, the pigment-pigment and the pigment-protein coupling beyond perturbation theory. Roughly speaking, the peak positions of optical lines are determined by the pigment-pigment coupling and the lineshape is determined by the pigment-protein coupling, including lifetime broadening and vibrational sidebands.

2.1 Hamiltonian of Pigment-Protein-Complexes

The theory is based on a standard Hamiltonian $H_{\rm ppc}$ for the pigment protein complex, that describes the pigments as coupled two-level systems interacting with vibrational degrees of freedom of the pigments and the protein,

$$H_{\rm ppc} = H_{\rm ex} + H_{\text{ex-vib}} + H_{\rm vib}\,. \tag{2.1}$$

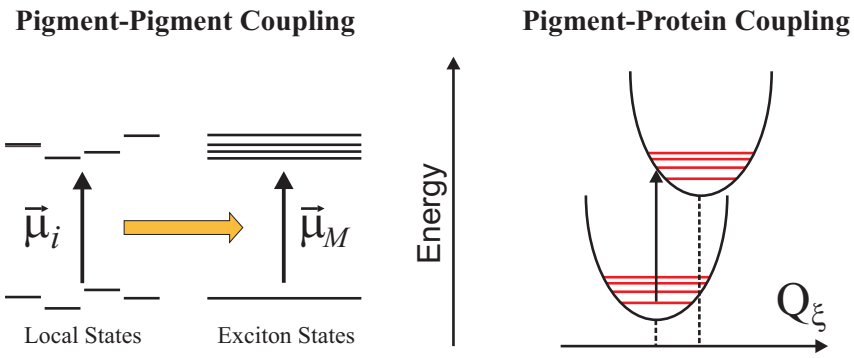

Figure 2.1: (*Left*) Pigment-pigment coupling leads to delocalized exciton states. (*Right*) Pigment-protein coupling leads to lifetime broadening and vibrational side bands in the optical spectra.

The exciton part

$$H_{\text{ex}} = \sum_m E_m |m\rangle\langle m| + \sum_{m \neq n} V_{mn} |m\rangle\langle n| \tag{2.2}$$

contains the site energies E_m of the pigments, defined as the optical transition energies at the equilibrium position of nuclei in the electronic ground state, and the excitation energy transfer couplings V_{mn} (see section 3.2).

The Hamiltonian $H_{\text{ex-vib}}$ describes the modulation of site energies by the vibrations. A linear dependence of the site energies on the (dimensionless) vibrational coordinate Q_ξ is assumed, which is defined in terms of creation and annihilation operators of vibrational quanta, $Q_\xi = C_\xi^\dagger + C_\xi$ [30, 31]

$$H_{\text{ex-vib}} = \sum_\xi \sum_m \hbar\omega_\xi g_\xi^{(m)} Q_\xi |m\rangle\langle m| \,. \tag{2.3}$$

The dimensionless coupling constants $g_\xi^{(m)} = g_\xi$ enter the spectral density $J(\omega)$ of the exciton vibrational coupling

$$J(\omega) = \sum_\xi g_\xi^2 \delta(\omega - \omega_\xi) \tag{2.4}$$

which is the key quantity in the expressions for optical spectra and the rate constants for exciton relaxation discussed below. $J(\omega)$ is assumed independent on the site index m, i.e., the same local modulation of site energies by the vibrational dynamics is assumed.

The vibrations are described by an Hamiltonian H_{vib} of harmonic oscillators

$$H_{\text{vib}} = \sum_\xi \frac{\hbar\omega_\xi}{4} Q_\xi^2 + T_{\text{nuc}} \,, \tag{2.5}$$

where T_{nuc} is the kinetic energy of nuclei.

The coupling between the pigment-protein complex and an external radiation field is described by the semiclassical Hamiltonian $H_{\text{ppc-rad}}$, which reads in rotating wave approximation

$$H_{\text{ppc-rad}} = -\sum_m \vec{\mu}_m \vec{e}\, E_\Omega(t) e^{-i\Omega t} |m\rangle\langle 0| + \text{h.c.} \,, \tag{2.6}$$

where $\vec{\mu}_m$ is the molecular transition dipole moment of the mth pigment, $\vec{e}$ the polarization of the field, and h.c. the hermitian conjugate. The field may be either stationary, i.e., $E_\Omega(t) = E_0$ or time-dependent. In the latter case a Gaussian shape for $E_\Omega(t)$ is assumed

$$E_\Omega(t) = \frac{E_0}{\sqrt{2\pi}\tau_p} e^{-t^2/(2\tau_p^2)} \,, \tag{2.7}$$

where the full width at half maximum (fwhm) of $E_\Omega(t)$ is $2\tau_p\sqrt{2\ln 2}$.

For the calculations of optical spectra and exciton relaxation, the above Hamiltonian $H_{\text{ppc}} + H_{\text{ppc-rad}}$ is expressed in terms of delocalized exciton states $|M\rangle$, which are given as linear combinations of localized excited states $|M\rangle = \sum_m c_m^{(M)} |m\rangle$, where $|c_m^{(M)}|^2$ describes the probability that the mth pigment is excited when the PPC is in the Mth exciton state. The exciton coefficients $c_m^{(M)}$ and excitation energies $\mathcal{E}_M$ are obtained from the solution of the eigenvalue problem $H_{\text{ex}}|M\rangle = \mathcal{E}_M|M\rangle$, with the H_{ex} of Eq 2.2. The Hamiltonian H_{ex} in Eq 2.2, simplifies in the basis of delocalized exciton states to:

$$H_{\text{ex}} = \sum_M \varepsilon_M |M\rangle\langle M|. \tag{2.8}$$

The Hamiltonian $H_{\text{ex-vib}}$ in Eq 2.3, in the basis of delocalized exciton states, using $|m\rangle = \sum_M c_m^{(M)}|M\rangle$ becomes

$$H_{\text{ex-vib}} = \sum_{M,N}\sum_{\xi} \hbar\omega_\xi g_\xi(M,N) Q_\xi |M\rangle\langle N| \tag{2.9}$$

with the exciton vibrational coupling constant

$$g_\xi(M,N) = \sum_m c_m^{(M)} c_m^{(N)} g_\xi^{(m)} \,, \tag{2.10}$$

that contains now diagonal ($M = N$) as well as off-diagonal ($M \neq N$) parts. The former give rise to vibrational sidebands of exciton transitions in optical spectra and the latter lead to relaxation between different exciton states. The coupling to the radiation field $H_{\text{ppc-rad}}$ in Eq 2.6 now reads

$$H_{\text{ppc-rad}} = -\sum_M \vec{\mu}_M \, \vec{e}\, E_\Omega(t)\, e^{-i\Omega t} |M\rangle\langle 0| + \text{h.c.}\,, \tag{2.11}$$

where the transition dipole moments $\vec{\mu}_M$ of the delocalized exciton states are obtained from the local transition dipole moments $\vec{\mu}_m$ and the exciton coefficients $c_m^{(M)}$ as

$$\vec{\mu}_M = \sum_m c_m^{(M)} \vec{\mu}_m \,. \tag{2.12}$$

The above Hamiltonians lead to the expressions for linear optical spectra, exciton state occupation probabilities, created by a short pulse, and rate constants of exciton relaxation, described in the following.

Delocalization of Excitons

The delocalization of excitons is investigated by the disorder averaged exciton states pigment distribution function $d_m(\omega)$ that describes the contribution of a given pigment m to the different exciton states [32]

$$d_m(\omega) = \left\langle \sum_M |c_m^{(M)}|^2 \delta(\omega - \omega_M) \right\rangle_{\text{dis}} \,. \tag{2.13}$$

The function $d_m(\omega)$ for the N pigments of a pigment protein complex can be compared with the density of exciton states

$$d_M(\omega) = \langle \delta(\omega - \omega_M) \rangle_{\text{dis}} \,. \tag{2.14}$$

$\langle \quad \rangle_{\text{dis}}$ denotes an average over static disorder in site energies. A Gaussian distribution function of width (fwhm) Δ_{dis} is assumed for these energies, and the disorder average is performed by a Monte Carlo method.

2.1.1 Linear Optical Spectra

The linear absorption $\alpha(\omega)$ is obtained from the Fourier-Laplace transform of the dipole-dipole correlation function $D(t)$ [33, 34], i. e.,

$$\alpha(\omega) \propto \Re \int_0^\infty dt\, e^{i\omega t}\, D(t) \,, \tag{2.15}$$

where $D(t) = \sum_M |\mu_M|^2 \rho_{M0}(t)$ and $\rho_{M0}(0) = 1$, with the density matrix ρ_{M0}, for detail see [30]. The linear absorption spectrum then is

$$\alpha(\omega) \propto \left\langle \sum_M |\vec{\mu}_M|^2 \, D_M(\omega) \right\rangle_{\text{dis}} \,, \tag{2.16}$$

where $D_M(\omega)$ is the lineshape function. In the calculation of circular dichroism, the dipole strength $|\vec{\mu}_M|^2$ in Eq 2.16 is replaced by the rotational strength $r_M = \sum_{m>n} c_m^{(M)} c_n^{(M)} \vec{R}_{mn} \cdot (\vec{\mu}_m \times \vec{\mu}_n)$, where $\times$ denotes a cross product and $\vec{R}_{mn}$ is the center to center distance of pigments m and n. In the case of linear dichroism $|\vec{\mu}_M|^2$ in Eq 2.16 is replaced by $|\vec{\mu}_M|^2(1 - 3\cos^2\theta_M)$, where θ_M is the angle between the symmetry axis of the trimer and the excitonic transition dipole moment $\vec{\mu}_M$.

Singlet Minus Triplet Spectra

The singlet spectrum is the usual linear absorption spectrum of N pigments described above (Eq 2.16), while the triplet spectrum is the linear absorption spectrum with a triplet state on one of the N pigments. The effect is that the pigment with the triplet state does not absorb in the Q_y region any more, i.e., does not effect the absorption spectrum. Hence the triplet spectrum is the linear absorption spectrum of the remaining $N-1$ pigments. The T−S spectrum is the difference of both spectra. That has the advantage that in good approximation, only the pigments coupled strongly to the pigment which carries the triplet state, affect the difference spectrum (see chapter 5).

Cation Minus Neutral Spectra

The $P^+ - P$ spectra are similar to the T−S spectra. In this case the P spectrum is the linear absorption spectrum of N pigments and the P^+ spectrum is the spectrum with a cation on one of the N pigments. This pigment does analog to the pigment with the triplet state not absorb in the Q_y region, hence a linear absorption spectrum of $N-1$ pigments results. In contrast to the T−S spectra, additionally the electrochromic shift of the site energies of the remaining $N-1$ pigments caused by the charge, must be considered. This is done by distributing the positive elementary charge over all heavy atoms of the pigment and calculating the electrochromic effect of that charge distribution on the transition density of the other pigments, following Eq 3.36 (here the charge distribution of the pigment with the cation is the background charge distribution, bg).

2.1.2 Lineshape function

The lineshape function $D_M(\omega)$ was obtained using a non-Markovian partial ordering prescription (POP) theory. It is given as [30]

$$D_M(\omega) = \Re \int_0^\infty dt\, e^{i(\omega-\tilde{\omega}_M)t}\, e^{G_M(t)-G_M(0)}\, e^{-t/\tau_M}\ , \tag{2.17}$$

where $\Re$ denotes the real part of the integral. $D_M(\omega)$ contains both vibrational sidebands and life-time broadening due to exciton relaxation. The vibrational sidebands are described by $G_M(t)$ and the life-time broadening is described by the dephasing time τ_M (discussed in detail below). Both quantities are related to the spectral density $J(\omega)$ in Eq 2.4. The time-dependent function $G_M(t)$ in Eq 2.17, is given as

$$G_M(t) = \gamma_{MM}\, G(t) \tag{2.18}$$

with

$$G(t) = \int_0^\infty d\omega \left[(1 + n(\omega))\, J(\omega)\, e^{-i\omega t} + n(\omega)\, J(\omega)\, e^{i\omega t} \right] \tag{2.19}$$

and γ_{MM} being the diagonal part of

$$\gamma_{MN} = \sum_{m,n} e^{-R_{mn}/R_c}\, c_m^{(M)} c_m^{(N)} c_n^{(M)} c_n^{(N)}\ . \tag{2.20}$$

It contains the exciton coefficients $c_m^{(M)}$, a correlation radius R_c of protein vibrations[1] and the center to center distance R_{mn} between pigments m and n.

The function $n(\omega)$ in Eq 2.19 is the mean number of vibrational quanta with energy $\hbar\omega$ that are excited at a given temperature T (Bose-Einstein distribution function)

$$n(\omega) = \frac{1}{e^{\hbar\omega/kT} - 1}\,, \tag{2.21}$$

where k is Boltzmann's constant. The dephasing time τ_M in Eq 2.17 is determined by the rate constants $k_{M\to N}$ of exciton relaxation, obtained using a Markov approximation for the off-diagonal parts of the exciton vibrational coupling,

$$\tau_M^{-1} = \frac{1}{2}\sum_{N\neq M} k_{M\to N} \tag{2.22}$$

where the rate constant reads

$$k_{M\to N} = 2\ \gamma_{MN}\,\tilde{C}^{(\mathrm{Re})}(\omega_{MN})\,. \tag{2.23}$$

It resembles the standard Redfield rate constant (e.g. Ref. [35]). The $\tilde{C}^{(\mathrm{Re})}(\omega_{MN})$ is the real part of the Fourier-Laplace transform of the pigment's optical energy gap correlation function [30]:

$$\tilde{C}^{(\mathrm{Re})}(\omega_{MN}) = \pi\,\omega_{MN}^2\Big[\big(1+n(\omega_{MN})\big)J(\omega_{MN}) + n(\omega_{NM})J(\omega_{NM})\Big]\,, \tag{2.24}$$

where $J(\omega) = 0$ for $\omega < 0$, and $\omega_{MN} = \omega_M - \omega_N$ is the transition frequency between the Mth and the Nth exciton state. The $\tilde{\omega}_M$ in Eq 2.17 is shifted from the purely excitonic transition frequency ω_M due to the exciton-vibrational coupling

$$\begin{aligned}\tilde{\omega}_M &= \omega_M + \sum_N \gamma_{MN}\tilde{C}^{(\mathrm{Im})}(\omega_{MN}) \\ &= \omega_M - \gamma_{MM}\frac{E_\lambda}{\hbar} + \sum_{N\neq M}\gamma_{MN}\tilde{C}^{(\mathrm{Im})}(\omega_{MN})\,,\end{aligned} \tag{2.25}$$

where γ_{MN} is given in Eq 2.20 and E_λ is the local reorganization energy

$$E_\lambda = \hbar\int_0^\infty d\omega\ \omega\, J(\omega)\,. \tag{2.26}$$

The $\tilde{C}^{(\mathrm{Im})}(\omega_{MN})$ in Eq 2.25 is related to the real part $\tilde{C}^{(\mathrm{Re})}(\omega)$ in Eq 2.24 by a Kramers-Kronig relation [30, 36]

$$\tilde{C}^{(\mathrm{Im})}(\omega_{MN}) = \frac{1}{\pi}\,\wp\int_{-\infty}^{+\infty} d\omega\frac{\tilde{C}^{(\mathrm{Re})}(\omega)}{\omega_{MN}-\omega}\,, \tag{2.27}$$

where $\wp$ denotes the principal part of the integral (details are given in section 2.1.5).

2.1.3 Vibrational Sidebands

The lineshape function $D_M(\omega)$ of Eq 2.17 is rewritten as

$$\begin{aligned}D_M(\omega) &= e^{-G_M(0)}\left\{\ \Re\int_0^\infty dt\, e^{i(\omega-\tilde{\omega}_M)t}e^{-t/\tau_M} + \Re\int_0^\infty dt\, e^{i(\omega-\tilde{\omega}_M)t}\ \Big(e^{G_M(t)}-1\Big)\ e^{-t/\tau_M}\right\} \\ &= ZL(\omega) + SB(\omega)\end{aligned} \tag{2.28}$$

[1] A value of $R_c = 5$ Å is used, that was determined from transient spectra of photosystem II reaction centers in [30]. The stationary spectra calculated here do not depend critically on this value.

where the zero vibrational quanta ($0 \rightarrow 0$) lineshape is

$$ZL(\omega) = e^{-G_M(0)} D_M^{(\mathrm{Mk})}(\omega) \tag{2.29}$$

with the Lorentzian shaped lineshape function $D_M^{(\mathrm{Mk})}(\omega)$ obtained from Markov approximation [30][2]

$$D_M^{(\mathrm{Mk})}(\omega) = \frac{\tau_M^{-1}}{(\omega - \tilde{\omega}_M)^2 + \tau_M^{-2}} \,. \tag{2.32}$$

The vibrational sideband reads

$$SB(\omega) = e^{-G_M(0)} \, \Re \int_0^\infty dt \, e^{i(\omega - \tilde{\omega}_M)t} \, \left(e^{G_M(t)} - 1 \right) \, e^{-t/\tau_M} \,. \tag{2.33}$$

We note that the area of the two contributions in the spectra, i.e. their integrals are

$$\int_{-\infty}^{\infty} d\omega \, ZL(\omega) = e^{-G_M(0)} \quad \text{and} \quad \int_{-\infty}^{\infty} d\omega \, SB(\omega) = 1 - e^{-G_M(0)} \,. \tag{2.34}$$

Hence the importance of non-Markovian effects, i.e. the integral weight of vibrational sidebands

$$\frac{\int d\omega \, SB(\omega)}{\int d\omega \, ZL(\omega)} = e^{G_M(0)} - 1 \tag{2.35}$$

depends on the function (using Eq 2.18 and Eq 2.19, with $t = 0$)

$$G_M(0) = \gamma_{MM} \int_0^\infty d\omega J(\omega)(1 + 2\, n(\omega)) \,. \tag{2.36}$$

We note that the quantity $\int d\omega \, J(\omega)$ in Eq 2.36 is known as the Huang-Rhys factor (see Eq 3.1) that is a measure of the local exciton-vibrational coupling and hence it seems to be useful to introduce a Huang-Rhys factor of exciton transition S_M as [30]:

$$S_M = \gamma_{MM} S \,, \quad \text{with} \quad 1 \geq \gamma_{MM} \geq \frac{1}{N}. \tag{2.37}$$

The factor γ_{MM} varies between unity for delocalized vibrations ($R_c \rightarrow \infty$) and $\frac{1}{N}$, where N is the number of pigments for localized vibrations and delocalized electronic states. In general, the S factors that are reported in the literature for multi-pigment protein complexes must be interpreted as S_M factors. For most antenna systems $S_M \leq 1$ holds. A notable exception being the red antenna states of PSI and the exciton states formed by the special pair pigments in the reaction centers. We see from Eqs 2.35 and 2.36 that the Markov approximation is valid for low temperatures, where $n(\omega) \approx 0$ in combination with $S_M \ll 1$ [3].

2.1.4 Franck-Condon Principle

The composition of the lineshape function $D_M(\omega)$ of the zero vibrational quanta line $ZL(\omega)$ and vibrational sideband $SB(\omega)$ is due to the well known Franck-Condon principle (FCP), ***IUPAC definition*** [37]:

---

[2] That is because the Fourier-transformation of $f(t) = \begin{cases} e^{-t/\tau_M} & t \geq 0 \\ 0 & t < 0 \end{cases}$ reads

$$F(\omega) = \frac{1}{\sqrt{2\pi}} \int_{-\infty}^{+\infty} dt \, f(t) \, e^{-i\omega t} = \frac{1}{\sqrt{2\pi}} \cdot \frac{1}{\tau_M^{-1} + i\omega} = \frac{1}{\sqrt{2\pi}} \cdot \frac{\tau^{-1} - i\omega}{\tau_M^{-2} + \omega^2} \tag{2.30}$$

and for the zero line $ZL(\omega)$ follows from

$$\Re \int_0^\infty dt \, e^{i(\omega - \tilde{\omega}_M)t} e^{-t/\tau_M} = \frac{\tau_M^{-1}}{(\omega - \tilde{\omega}_M)^2 + \tau_M^{-2}} \,. \tag{2.31}$$

[3] $n(\omega) \approx 0 \quad \Rightarrow \quad G_M(0) = \gamma_{MM} \int d\omega J(\omega) = \gamma_{MM} S \quad \Rightarrow \quad \frac{\int d\omega SB}{\int d\omega ZL} = e^{\gamma_{MM} S} - 1 = 0 \quad \text{if} \quad S \approx 0.$

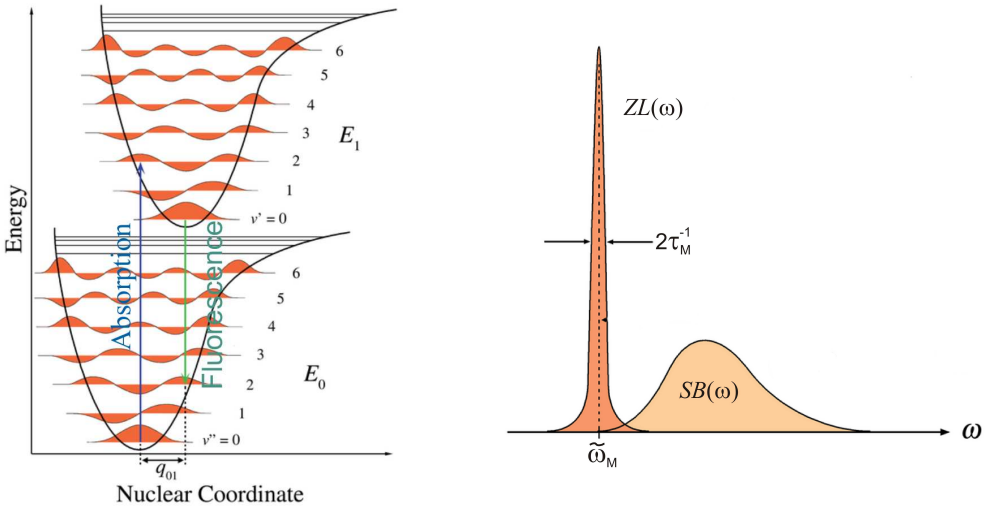

Figure 2.2: (*Left*) Franck-Condon principle energy diagram. Due to the FCP vertical transitions occur, favoring vibrational levels. In the situation shown here, transitions between $\nu'' = 0$ and $\nu' = 2$ (and vice versa) are favored. (*Right*) Schematic representation of the line shape of an electronic excitation. The narrow component at the frequency $\tilde{\omega}_M$ is the zero-phonon line $ZL(\omega)$ and the broader feature at higher frequency is the phonon sideband $SB(\omega)$. In emission the relative positions of the two components are reversed. Images by Mark M. Somoza.

Classically, the Franck Condon principle is the approximation that an electronic transition is most likely to occur without changes in the positions of the nuclei in the molecular entity and its environment. The resulting state is called a Franck Condon state, and the transition involved, a vertical transition. The quantum mechanical formulation of this principle is that the intensity of a vibronic transition is proportional to the square of the overlap integral between the vibrational wavefunctions of the two states that are involved in the transition.

Usually electronic transitions of molecules are simultaneous changes in electronic and vibrational energy levels due to absorption or emission of a photon of the corresponding energy. The FCP declares that during an electronic transition, a change from one vibrational energy level to another will be more likely to occur if the two vibrational wave functions overlap more significantly.

The vibrational levels and wavefunctions can be described by quantum harmonic oscillators, or by more complex approximations to the potential energy of molecules, e.g. Morse potential. In Fig 2.2 (*left*) the FCP for vibronic transitions in a molecule with a potential energy functions of Morse type (for ground and excited electronic states) is depicted. In the low temperature approximation, the molecule is originally in the $\nu = 0$ vibrational level of the electronic ground state. The absorption of a photon of the appropriate energy induces a transition to the excited electronic state. The new electron configuration may result in a change of the equilibrium positions of the molecules nuclei. In Fig 2.2 (*left*) this change in nuclear coordinates between ground and excited state is labeled as q_{01}. In the case of a diatomic molecule the nuclear coordinates axis refers to the separation between both nuclei. The vibronic transition is indicated by a vertical arrow due to the assumption of frozen nuclear coordinates during the transition. The probability for the molecule to end up in a particular vibrational level is proportional to the square of the overlap of the vibrational wavefunctions of the original and final state (Franck-Condon factors, compare section 3.2.5). In the electronic excited state molecules relax to the lowest vibrational level, quickly. From there the decay to the lowest electronic state occurs via photon emission.

The FCP is valid for absorption and fluorescence. The vibrational structure is most clearly visible if inhomogeneous broadening is absent, as it is the case for molecules of a cold diluted gas. In this case vibronic transitions are narrow, equally spaced Lorentzian curves. Equally spaced vibrational levels only

appear for the parabolic potential of harmonic oscillators. For more realistic potentials, such as the Morse potential, energy spacing decreases with increasing vibrational energy. Electronic transitions from the lowest vibrational states of the electronic ground state to the lowest vibrational states of the first excited state are called $0-0$ transitions, and have the same energy in absorption and fluorescence. Transitions from the lowest vibrational states of the electronic ground state to the first vibrational states of the first excited state are called $0-1$ transition and so on.

2.1.5 Frequency Shift

The non-diagonal parts of the frequency shift in Eq 2.25 are in general small compared to the diagonal part $\gamma_{MM}E_\lambda/\hbar$. These non-diagonal parts are obtained with the help of the Kramers-Kronig relation (Eq 2.27) using Eq 2.24:

$$\tilde{C}^{(\mathrm{Im})}(\omega_{MK}) = S_0 \; \wp \int_0^\infty d\omega \frac{\omega^2}{\omega_{MK}-\omega} J_0(\omega) + S_0 \; \wp \int_0^\infty d\omega \frac{2\,\omega^2\omega_{MK}}{\omega_{MK}^2-\omega^2} n(\omega) J_0(\omega)\,. \tag{2.38}$$

To solve the principal part integrals in the above equation we apply an approximation of Jang, Cao and Silbey [38] for the function $n(\omega)$ of Eq 2.21

$$n(\omega) \approx e^{-\frac{\hbar\omega}{kT}} + e^{-2\frac{\hbar\omega}{kT}} + \frac{kT}{\hbar\omega} e^{-\frac{5}{2}\frac{\hbar\omega}{kT}} \tag{2.39}$$

and approximate the spectral density $J(\omega)$ (Eq 3.2) by a more simple functional form [38]

$$S_0 J_0(\omega) \approx \omega \cdot \sum_{i=1}^{3} \frac{s_i}{\omega_i^2}\, e^{-\frac{\omega}{\omega_i}} \tag{2.40}$$

where $s_1 = 0.9,\ s_2 = 0.25,\ s_3 = 0.15$, and $\hbar\omega_1 = 2.5$ meV, $\hbar\omega_2 = 8.7$ meV, $\hbar\omega_3 = 12.4$ meV [39].

The above principal part integrals are then solved for the approximations introduced above for $J_0(\omega)$ and $n(\omega)$. At low temperatures ($T < 10$ K), considered here, the $\tilde{C}^{(\mathrm{Im})}(\omega_{MK})$ in Eq 2.38 can be approximated by the first integral in Eq 2.38, leading to

$$\tilde{C}^{(\mathrm{Im})}(\omega_{MK}) \approx S_0 \sum_{i=1}^{3} \frac{s_i}{\omega_i^2} \left[\omega_{MK}^3 \,\mathrm{Ei}\left(\frac{\omega_{MK}}{\omega_i}\right) e^{-\frac{\omega_{MK}}{\omega_i}} - 2\omega_i^3 - \omega_i^2\omega_{MK} - \omega_i\omega_{MK}^2 \right], \tag{2.41}$$

where $\mathrm{Ei}(x)$ is the Exponential integral, which is defined for $|x| < \infty,\ x \neq 0$ ($\wp$ denotes Cauchy's principal value) as:

$$\mathrm{Ei}(x) = \wp \int_{-\infty}^{x} dt\, \frac{e^t}{t} = C + \ln|x| + \sum_{n=1}^{\infty} \frac{x^n}{n \cdot n!}\,, \tag{2.42}$$

with the Euler-constant $C = 0.577215665$. It was calculated numerically [40].

The second integral in Eq 2.38, which contributes at higher temperatures, yields

$$\begin{aligned} \int_0^\infty d\omega \frac{2\omega^2\omega_{MK}}{\omega_{MK}^2-\omega^2} n(\omega)J(\omega) = S_0 \sum_{i=1}^{3} \frac{2s_i}{\omega_i^2} \Bigg\{ & \int_0^\infty d\omega \frac{\omega^3\omega_{MK}}{\omega_{MK}^2-\omega^2} e^{-a_i\omega} + \\ & + \int_0^\infty d\omega \frac{\omega^3\omega_{MK}}{\omega_{MK}^2-\omega^2} e^{-b_i\omega} + \frac{kT}{\hbar} \int_0^\infty d\omega \frac{\omega^2\omega_{MK}}{\omega_{MK}^2-\omega^2} e^{-c_i\omega} \Bigg\}, \end{aligned} \tag{2.43}$$

where

$$a_i = \frac{\hbar}{kT} + \frac{1}{\omega_i}\,, \qquad b_i = \frac{2\hbar}{kT} + \frac{1}{\omega_i}\,, \qquad c_i = \frac{5\hbar}{2kT} + \frac{1}{\omega_i}\,. \tag{2.44}$$

The first integral of Eq 2.43 is given as:

$$\int_0^\infty d\omega \frac{\omega^3 \omega_{MK}}{\omega_{MK}^2 - \omega^2} e^{-a_i \omega} = \frac{\omega_{MK}^3}{2} \left[e^{-a_i \omega_{MK}} \mathrm{Ei}(a_i \omega_{MK}) + e^{a_i \omega_{MK}} \mathrm{Ei}(-a_i \omega_{MK}) \right] - \frac{\omega_{MK}}{a_i^2} \quad (2.45)$$

the second integral is obtained by replacing a_i by b_i in Eq 2.45, and the third integral reads:

$$\int_0^\infty d\omega \frac{\omega^2 \omega_{MK}}{\omega_{MK}^2 - \omega^2} e^{-c_i \omega} = \frac{\omega_{MK}^2}{2} \left[e^{-c_i \omega_{MK}} \mathrm{Ei}(c_i \omega_{MK}) - e^{c_i \omega_{MK}} \mathrm{Ei}(-c_i \omega_{MK}) \right] - \frac{\omega_{MK}}{c_i} . \quad (2.46)$$

Combining the above three expressions that solve Eq 2.43 with Eq 2.41 the overall solution for $\tilde{C}^{(\mathrm{Im})}(\omega_{MK})$ is obtained as

$$\begin{aligned} \tilde{C}^{\mathrm{Im}}(\omega_{MK}) = S_0 \sum_{i=1}^{3} \frac{s_i}{\omega_i^2} \Bigg\{ & \omega_{MK}^3 e^{-\frac{\omega_{MK}}{\omega_i}} \mathrm{Ei}\Big(\frac{\omega_{MK}}{\omega_i}\Big) \\ & + \omega_{MK}^3 \Big[e^{-a_i \omega_{MK}} \mathrm{Ei}\left(a_i \omega_{MK}\right) + e^{a_i \omega_{MK}} \mathrm{Ei}\left(-a_i \omega_{MK}\right) \Big] \\ & + \omega_{MK}^3 \Big[e^{-b_i \omega_{MK}} \mathrm{Ei}\left(b_i \omega_{MK}\right) + e^{b_i\, \omega_{MK}} \mathrm{Ei}\left(-b_i\, \omega_{MK}\right) \Big] \\ & + \frac{kT}{\hbar} \omega_{MK}^2 \Big[e^{-c_i \omega_{MK}} \mathrm{Ei}\left(c_i \omega_{MK}\right) - e^{c_i\, \omega_{MK}} \mathrm{Ei}\left(-c_i\, \omega_{MK}\right) \Big] \\ & - \omega_i \Big(2\omega_i^2 + \omega_i \omega_{MK} + \omega_{MK}^2 \Big) - 2\omega_{MK} \Big(\frac{1}{a_i^2} + \frac{1}{b_i^2} + \frac{kT}{\hbar c_i} \Big) \Bigg\} . \end{aligned} \quad (2.47)$$

2.1.6 Different Levels of Theory

Simulated spectra using different levels of theory described in the following, are shown in Fig 2.3.

1. Stick-spectra (Fig 2.3, *left*, red): obtained from Eq 2.16 by neglecting any homogeneous broadening, i.e., life-time broadening and vibrational sidebands, by setting $G_M(t) = 0$ and $\tau_M^{-1} = 0$ in Eq 2.17. In this case the line shape function $D_M(\omega)$ becomes just a delta-function that peaks at the exciton transition frequency ω_M, $D_M(\omega) = \delta(\omega - \omega_M)$.

2. Gauss-dressed stick-spectra (*left*, green): to perform the average over disorder analytically, any resonance energy transfer narrowing [41], i.e. a decrease of the width of the distribution of exciton energies with respect to that of the distribution of local transition energies is neglected as well. Assuming a Gaussian distribution function

$$P(\omega_M - \bar{\omega}_M) = \frac{1}{\sqrt{2\pi\sigma^2}} \exp\left[\frac{-(\omega_M - \bar{\omega}_M)^2}{(2\sigma^2)} \right] \quad (2.48)$$

   of the same width (fwhm $= 2\sqrt{2 \ln 2}\ \sigma$) for all exciton energies $\hbar\omega_M$ (a so-called *Gauss-dressed stick-spectrum*), results in

$$\alpha(\omega) \propto \frac{1}{\sqrt{2\pi\sigma^2}} \sum_M |\vec{\mu}_M|^2 e^{-(\omega - \bar{\omega}_M)^2/(2\sigma^2)} , \quad (2.49)$$

   where the mean exciton energies $\bar{\omega}_M$ are those obtained for the mean site energies.

3. Dynamic theory, Markov approximation (*right*, red): Additionally to the solution of the exciton eigenvalue problem it includes a shift of the peak positions (Eq 2.25) and lifetime broadening due to pigment-protein coupling, resulting in Lorentzian shaped lineshapes (Eq 2.32). The peak shift of Eq 2.25 can even be simplified to the diagonal part only, i.e.,

$$\tilde{\omega}_M = \omega_M - \gamma_{MM} \frac{E_\lambda}{\hbar}, \quad (2.50)$$

   because the overall spectrum is more affected by the simplification of the lineshape.

4. Dynamic theory, non-Markovian (*right*, green): Beyond the Markov approximation it includes also vibrational sidebands, i.e. $D_M(\omega) = ZL(\omega) + SB(\omega)$, given in Eqs 2.29, 2.32, 2.33, and the complete peak shift of Eq 2.25.

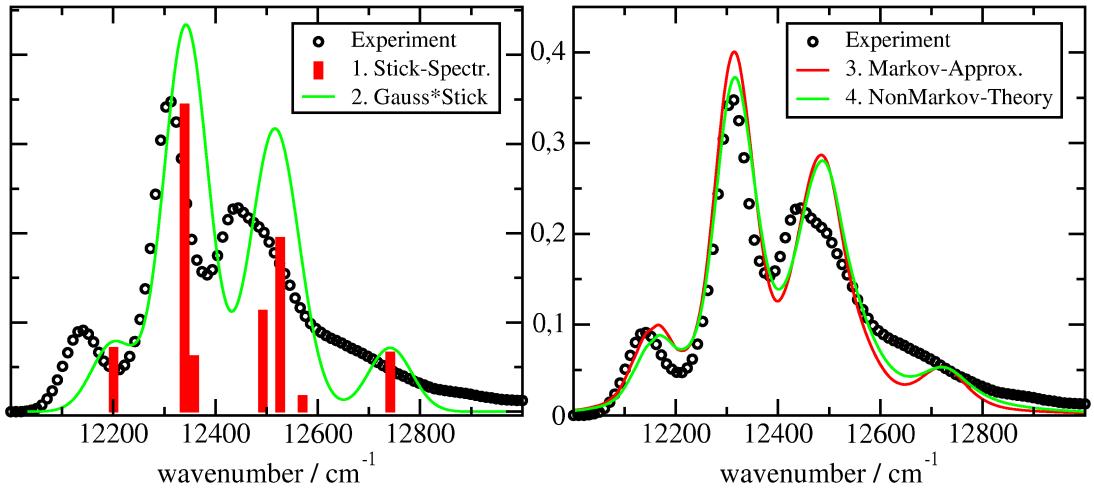

Figure 2.3: Simulated spectra for different levels of theory are shown: (*left*) 1. stick-spectra (red), 2. Gauss-dressed stick-spectra (green), (*right*) 3. Markov approximation (red), 4. non-Markov theory (green). The experimental spectrum of the FMO complex from *P. aestuarii* is measured by Wendling *et al.* [42].

2.1.7 Relation of the Present to Earlier Theories

The theory used by Vulto *et al.* [43] was the method of Gauss-dressed stick-spectra, described above. In the theory of Wendling *et al.* [42, 44], resonance energy transfer narrowing, life-time broadening and vibrational sidebands were taken into account using the following approximations for the function $D_M(\omega)$ in Eq 2.17: (i) a shift of the transition frequency ω_M by the exciton vibrational coupling was neglected, i.e. $\tilde{\omega}_M = \omega_M$ in Eq 2.25, (ii) any dependence of the vibrational sidebands of the exciton transitions on the delocalization of exciton states was neglected by replacing the function $G_M(t) = \gamma_{MM} G(t)$ in Eq 2.17 by the function $G(t)$, that describes the vibrational sidebands of a monomeric BChl*a* in a protein environment, (iii) the factor $\pi\omega_{MN}^2$ appearing in Eqs 2.22 and 2.24 for the rate constant of exciton relaxation between the Mth and the Nth state was approximated by a constant γ_0 that is assumed the same for all transitions $M \to N$, i.e., instead of the $\tilde{C}^{\mathrm{Re}}(\omega)$ in the lower part of Fig 3.3 a scaled $J(\omega)$ in the upper part of this figure is used.

The main differences between the non-Markovian theory (used throughout this work) and the two earlier theories are illustrated in Fig 2.4. Due to the neglect of vibrational sidebands in the theory of Vulto *et al.* [43] (green line), there is less intensity in the blue part of the spectrum. The missing life time broadening seems to be compensated in part by the neglect of resonance energy transfer narrowing as seen by the width of the two main peaks. In the theory of Wendling *et al.* [42, 44] (red line) the neglect of the dependence of the vibrational sideband on the exciton states delocalization leads to a stronger vibrational sideband as seen in the blue part of the spectrum and to a change of the relative height of the two main peaks. We note that the differences between the three theories are partly compensated in the fit of optical spectra by different site energies. However, as will be seen below the overall ranking of optimal site energies is similar in all three approaches.

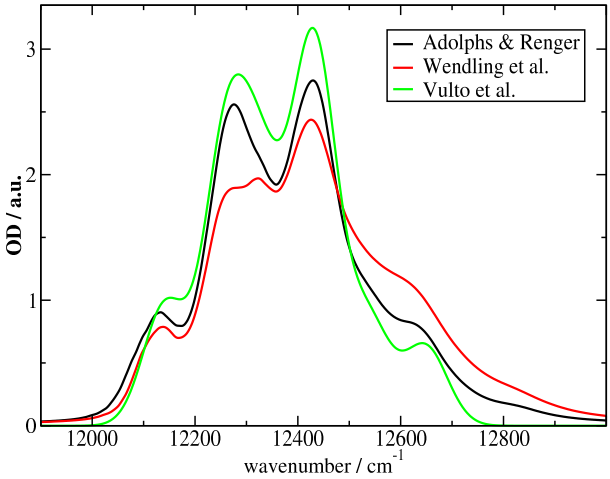

Figure 2.4: Calculation of absorption spectra of FMO-trimer of *C. tepidum* using site energy values from Table 4.3 using three different theories of optical spectra as explained in the text. The black line shows the non-Markovian theory, the green line Gauss-dressed stick-spectra as in Ref. [43] and the red line a theory in which the vibrational sidebands of exciton transitions were approximated by a vibrational sideband of monomeric BChl as in Ref. [42]. For better comparison the red line was red-shifted by 50 cm^{-1} and the green line by 35 cm^{-1}.

2.1.8 Excitation by a Short Laser Pulse

In chapter 4 we want to describe exciton relaxation after excitation by a short laser puls. For this purpose we first introduce the potential energy surface (PES) of exciton states by rewriting the Hamiltonian $H_{\rm ppc}$ of Eq 2.1 in terms of exciton states $|M\rangle$ (using Eqs 2.5, 2.8 and 2.9) and the completeness relation $|0\rangle\langle 0| + \sum_M |M\rangle\langle M| = 1$, as

$$H_{\rm ppc} = U_0(Q)|0\rangle\langle 0| + \sum_M U_M(Q)|M\rangle\langle M| + \sum_{M\neq N}\sum_\xi \hbar\omega_\xi g_\xi(M,N) Q_\xi |M\rangle\langle N| + T_{\rm nuc} \qquad (2.51)$$

where the diagonal part of the exciton-vibrational coupling was used to construct potential energy surfaces (PES) of exciton states

$$U_M(Q) = \varepsilon_M^{(0)} + \sum_\xi \frac{\hbar\omega_\xi}{4}\left(Q_\xi + 2\,g_\xi(M,M)\right)^2 \qquad (2.52)$$

that are shifted along the coordinate axis by $-2\,g_\xi(M,M)$ with respect to the PES $U_0(Q)$ of the ground state

$$U_0(Q) = \sum_\xi \frac{\hbar\omega_\xi}{4} Q_\xi^2\,. \qquad (2.53)$$

The energy $\varepsilon_M^{(0)} = \hbar\omega'_M$ is the transition energy between the minima of the excited state and the ground state PES (see Fig 2.5),

$$\varepsilon_M^{(0)} = \varepsilon_M - \gamma_{MM} E_\lambda \qquad (2.54)$$

where $\varepsilon_M = \hbar\omega_M$ is the vertical transition energy (site energy) and E_λ the local reorganization energy in Eq 2.26, see Fig 2.5. It is assumed that the off-diagonal parts of the exciton vibrational coupling[4] $g_\xi(M,N)$, Eq 2.10, are weak enough so that exciton relaxation during the short excitation pulse can be

[4]The diagonal part $g_\xi(M,M)$ of the exciton vibrational coupling determines the shift of the PES of exciton state $|M\rangle$ relative to the ground state $|0\rangle$, while the non-diagonal part $g_\xi(M,N)$ couples the exciton states $|M\rangle$ and $|N\rangle$, i.e., leads to exciton relaxation.

neglected. In this case, a non-perturbative inclusion of the diagonal part of the exciton vibrational coupling and a second order perturbation theory with respect to $H_{\text{ppc-rad}}$ in Eq 2.11 yields for the population $P_M(t)$ of the Mth exciton state

$$P_M(t) = \frac{|\vec{\mu}_M|^2}{3\hbar^2} \int_{t_0}^{t} d\tau \int_{t_0}^{\tau} d\tau_1 \, e^{-i(\Omega-\omega'_M)(\tau-\tau_1)} E_\Omega(\tau) E_\Omega(\tau_1) \cdot \\ \cdot \, \mathrm{Tr}_{\text{vib}} \left\{ e^{\frac{i}{\hbar}U_M(\tau-\tau_1)} \, e^{-\frac{i}{\hbar}U_0(\tau-\tau_1)} \, W_0^{(\text{eq})} \right\} \tag{2.55}$$

where Tr_{vib} denotes a trace with respect to the vibrational degrees of freedom, and the vibrationally relaxed initial electronic ground state, is described by the equilibrium statistical operator $W_0^{(\text{eq})}$

$$W_0^{(\text{eq})} = \frac{e^{-(U_0+T_{\text{nuc}})/kT}}{\mathrm{Tr}_{\text{vib}}\{e^{-(U_0+T_{\text{nuc}})/kT}\}} \tag{2.56}$$

and an average over a random orientation of complexes with respect to the polarization of the external field was performed. By changing the integration variable $\tau - \tau_1 \rightarrow \tau_1$, and setting $t_0 \rightarrow -\infty$ the occupation probability is obtained as

$$P_M(t) = 2\frac{|\vec{\mu}_M|^2}{3\hbar^2} \Re \int_0^\infty d\tau_1 e^{-i(\Omega-\omega'_M)\tau_1} f(t,\tau_1) g(\tau_1) \tag{2.57}$$

where $\Re$ denotes the real part and $f(t,\tau_1)$ is given as

$$f(t,\tau_1) = \int_{-\infty}^{t} d\tau E_\Omega(\tau) E_\Omega(\tau-\tau_1) \,, \tag{2.58}$$

which for $t \rightarrow \infty$ becomes the autocorrelation function of the pulse. The function $g(\tau_1)$ contains the average over the vibrational degrees of freedom that is performed using a second order cumulant expansion, which is exact for harmonic oscillators [31]

$$g(\tau_1) = \mathrm{Tr}_{\text{vib}} \left\{ e^{-\frac{i}{\hbar}U_M(\tau_1)} e^{-\frac{i}{\hbar}U_0(\tau_1)} W_0^{(\text{eq})} \right\} = e^{G_M(\tau_1)-G_M(0)} \,. \tag{2.59}$$

The population of exciton states after the action of the short pulse $P_M^{(p)}$ is obtained by formally setting $t \rightarrow \infty$. With the $E_\Omega(t)$ in Eq 2.7, the population $P_M^{(p)}$ reads

$$P_M^{(p)} = \frac{2|\vec{\mu}_M|^2}{3\hbar^2} \Re \int_0^\infty d\tau e^{-i(\Omega-\omega'_M)\tau} e^{G_M(\tau)-G_M(0)} e^{-\tau^2/(4\tau_p^2)} \,. \tag{2.60}$$

This result will be used as an initial condition in the calculation of exciton relaxation, discussed in the following.

2.1.9 Exciton Relaxation Dynamics

In Redfield theory a Markovian treatment of the diagonal part of the exciton vibrational coupling is performed, neglecting the mutual shift of the excitonic PES. Modified Redfield theory [32, 45–47] allows to treat this shift. By that, the reorganization of nuclei occurring upon exciton relaxation between different excitonic PES (Fig 2.5) is included. Assuming that the system is relaxed in the PES of exciton state $|M\rangle$, initially, a rate constant $k_{M\rightarrow N}$ for exciton relaxation between the two excitonic PES is obtained from second order perturbation theory in the couplings between the PES of state $|M\rangle$ and $|N\rangle$. Using a harmonic oscillator description for the vibrations, the following rate constant is obtained [32, 47]:

$$k_{M\rightarrow N} = \int_{-\infty}^{\infty} d\tau \; e^{i\omega'_{MN}\tau} e^{\phi_{MN}(\tau)-\phi_{MN}(0)} [(\frac{\lambda_{MN}}{\hbar} + G_{MN}(\tau))^2 + F_{MN}(\tau)] \,, \tag{2.61}$$

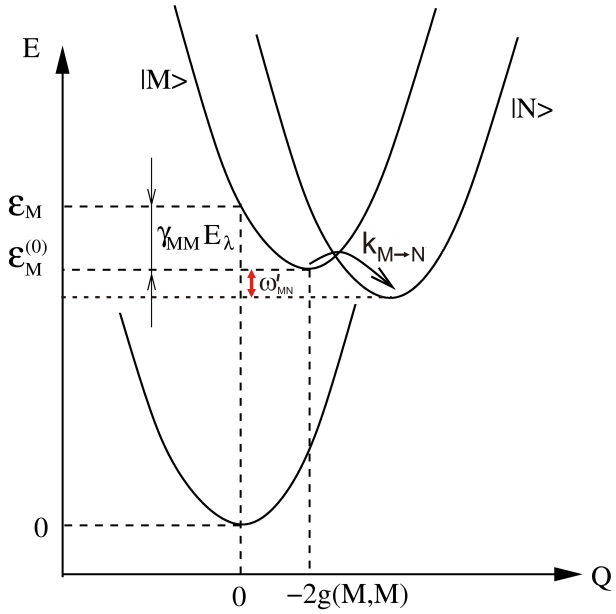

Figure 2.5: Potential energy surfaces of the ground state and two exciton states $|M\rangle$ and $|N\rangle$. The displacements of the different PES along the vibrational coordinate Q gives rise to vibrational side bands of exciton transitions in optical spectra and reorganization effects of nuclei in exciton relaxation.

with ω'_{MN} following from Eq 2.54:

$$\omega'_{MN} = \omega'_M - \omega'_N = \omega_{MN} - (\gamma_{MM} - \gamma_{NN}) \cdot E_\lambda \tag{2.62}$$

and where the time-dependent functions

$$\phi_{MN}(t) = a_{MN}\ \phi_0(t)\,, \qquad G_{MN}(t) = b_{MN}\ \phi_1(t)\,, \qquad F_{MN}(t) = c_{MN}\ \phi_2(t) \tag{2.63}$$

are related to the spectral density $S_0 J_0(\omega)$ via the function $\phi_k(t)$, with $k = 0, 1, 2$,

$$\phi_k(t) = S_0 \int_{-\infty}^{\infty} d\omega\, e^{-i\omega t}(1 + n(\omega))\, \omega^k (J_0(\omega) - J_0(-\omega))\,. \tag{2.64}$$

The time-independent part in the integrand in Eq 2.61, λ_{MN}, is

$$\lambda_{MN} = d_{MN} E_\lambda\,, \tag{2.65}$$

using the local reorganization energy E_λ in Eq 2.26 with $J(\omega) = S_0 J_0(\omega)$. The coefficients a_{MN}, b_{MN}, c_{MN}, and d_{MN} in the above equations are given by the exciton coefficients and the correlation radius of protein vibrations as [32]

$$a_{MN} = \sum_{mn} \left((c_m^{(M)})^2 (c_n^{(M)})^2 + (c_m^{(N)})^2 (c_n^{(N)})^2 - 2(c_m^{(M)})^2 (c_n^{(N)})^2 \right) e^{-R_{mn}/R_c} \tag{2.66}$$

$$b_{MN} = \sum_{mn} \left((c_m^{(M)})^2 - (c_m^{(N)})^2 \right) c_n^{(M)} c_n^{(N)} e^{-R_{mn}/R_c} \tag{2.67}$$

$$c_{MN} = \sum_{mn} c_m^{(M)} c_m^{(N)} c_n^{(M)} c_n^{(N)} e^{-R_{mn}/R_c} \tag{2.68}$$

$$d_{MN} = \sum_{mn} \left((c_m^{(M)})^2 + (c_m^{(N)})^2 \right) c_n^{(M)} c_n^{(N)} e^{-R_{mn}/R_c}\,. \tag{2.69}$$

If the diagonal part of the exciton vibrational coupling, i.e., the mutual shift of excitonic PES surfaces, is neglected, Eq 2.61 reduces to the Redfield result in Eq 2.23: The only function in Eq 2.61 that does not contain a diagonal part of the coupling is the $F_{MN}(t)$ in Eq 2.63 [47]. After setting the remaining functions zero, Eq 2.61 becomes $k_{M\to N} = \int_{-\infty}^{\infty} d\tau\ e^{i\omega_{MN}\tau} F_{MN}(\tau)$. If the $F_{MN}(t)$ in Eq 2.63 is introduced and the integration over τ is carried out, the rate constant becomes $k_{M\to N} = 2\pi\gamma_{MN}\omega_{MN}^2(1+n(\omega_{MN}))(J(\omega_{MN}) - J(\omega_{NM}))$. By noting that $-(1+n(\omega_{MK})) = n(\omega_{KM})$, the equality of the above rate constant with the Redfield result in Eq 2.23 is seen.

Exciton relaxation dynamics is described by the rate equations for the populations $P_M(t)$ of exciton states

$$\frac{d}{dt}P_M(t) = -\sum_{N\neq M}\left(k_{M\to N}P_M(t) + k_{N\to M}P_N(t)\right) \tag{2.70}$$

with the initial populations $P_M(0) = P_M^{(p)}$ created by the short pulse (Eq 2.60). Alternatively, exciton states which are formed by the pigments at the top of the trimer in Fig 4.10 will be populated at time zero to mimic excitation energy transfer as it occurs in *vivo* between the chlorosomes and the RC. For the rate constants $k_{M\to N}$ the modified Redfield result in Eq 2.61 or the Redfield expression in Eq 2.23 is used. In matrix form Eq 2.70 reads $\frac{d}{dt}\vec{P}(t) = -A\vec{P}(t)$, where the Mth element of $\vec{P}(t)$ is $P_M(t)$ and the kinetic matrix A contains in the diagonal the elements $A_{MM} = \sum_{N\neq M} k_{M\to N}$ and in the off-diagonal $A_{MN} = -k_{N\to M}$. The standard solution for $\vec{P}(t)$ is given as $\vec{P}(t) = \sum_i d_i\vec{c}_i e^{-\lambda_i t}$, where the λ_i and $\vec{c}_i$ are the eigenvalues and (right) eigenvectors of the kinetic matrix A and the constants d_i are obtained from the initial condition $\vec{P}(0) = \sum_i d_i\vec{c}_i$.

2.2 Theory of Excitonic Couplings in Dielectric Media

The following perturbative treatment of solute-solvent interaction is a part of [48]. We consider a pair of excitonically coupled solute (pigment) molecules, denoted by A and B, that is surrounded by N solvent (amino acid residue) molecules C_ξ, where $\xi = 1,\ldots,N$. The localized excited states of the system are denoted as $|A^{(0)}\rangle$, $|B^{(0)}\rangle$, and $|C_{m_\xi}^{(\xi)}\rangle$, denoting the states of the system where A is in its first excited state, B is in its first excited state, and solvent molecule ξ is in excited state m_ξ, respectively, while all other molecules are in their ground state. The respective energies are E_A, E_B and E_{m_ξ}. The energy E_0 of the ground state of the complex $|0\rangle$ is set to zero. The intermolecular Coulomb-coupling Hamiltonian $\hat{V}$ contains three parts

$$\hat{V} = \hat{V}_{AB} + \sum_\xi\left(\hat{V}_{AC_\xi} + \hat{V}_{BC_\xi}\right), \tag{2.71}$$

the coupling between A and B, A and C_ξ, and B and C_ξ, respectively. In the following, a perturbation theory in the solute-solvent coupling is used[5] to derive an expression for the matrix element for excitation energy transfer between A and B. For molecules A and B which are not excitonically coupled to each other but to the solvent molecules, we can express the corresponding states as $|A\rangle = |A^{(0)}\rangle + |\delta A^{(0)}\rangle$ ($|B\rangle$ analog), used in Eq 2.72:

$$\begin{aligned} V_{AB}^{(\mathrm{ex})} &= \langle A|\hat{V}|B\rangle \\ &\approx \langle A^{(0)}|\hat{V}|B^{(0)}\rangle + \langle\delta A|\hat{V}|B^{(0)}\rangle + \langle A^{(0)}|\hat{V}|\delta B\rangle \end{aligned} \tag{2.72}$$

where first order perturbation theory in the solute-solvent coupling gives for the wavefunctions $|\delta A\rangle$:

$$|\delta A\rangle = \sum_{\xi,m_\xi}\frac{V_{AC_{m_\xi}}^{(\xi)}}{E_A - E_{m_\xi}}|C_{m_\xi}\rangle, \tag{2.73}$$

[5]The term $\hat{V}_{AB}$ is the main part of the Hamiltonian, while the term $\sum_\xi\left(\hat{V}_{AC_\xi} + \hat{V}_{BC_\xi}\right)$ is considered as the small perturbation.

analog for $|\delta B\rangle$. After inserting Eq 2.73 into Eq 2.72 we obtain

$$V_{AB}^{(\mathrm{ex})} = V_{AB}^{(0)} + \delta V_{AB}^{(\mathrm{ex})} \tag{2.74}$$

where $V_{AB}^{(0)} = \langle A^{(0)}|\hat{V}_{AB}|B^{(0)}\rangle$ describes the excitonic coupling in vacuum and $\delta V_{AB}^{(\mathrm{ex})}$ contains the effect of the dielectric medium, with

$$\begin{aligned}\delta V_{AB}^{(\mathrm{ex})} &= \sum_{\xi,m_\xi} V_{AC_{m_\xi}^{(\xi)}} V_{C_{m_\xi}^{(\xi)}B}\left(\frac{1}{E_A - E_{m_\xi}} + \frac{1}{E_B - E_{m_\xi}}\right) \\ &\approx -2\sum_{\xi,m_\xi} \frac{V_{AC_{m_\xi}^{(\xi)}} V_{C_{m_\xi}^{(\xi)}B}}{E_{m_\xi}}\,. \end{aligned} \tag{2.75}$$

In the second line of Eq 2.75 we have used the fact that the excitation energies of the solvent molecules are much larger than that of the first excited state of the solutes, i.e., it holds $E_{A/B} \ll E_{m_\xi}$.

Starting from a many electron wavefunction for the solute and the solvent molecule, the above matrix elements are described by the Coulomb coupling between atomic partial charges [49]

$$\langle A|\hat{V}_{AC_\xi}^{(\xi)}|C_{m_\xi}\rangle = \sum_{I,J} \frac{q_I^{(A)}(0,1) q_J^{(C_\xi)}(0,m_\xi)}{|\mathbf{R}_I^{(A)} - \mathbf{R}_J^{(C_\xi)}|}\,, \tag{2.76}$$

where $\mathbf{R}_I^{(A)}$ and $\mathbf{R}_J^{(C_\xi)}$ are the position vectors of the Ith atom of molecule A and the Jth atom of molecule C_ξ, analog for molecule B. The atomic partial charges $q_I^{(A/B)}(0,1)$ and $q_J^{(C_\xi)}(0,m_\xi)$ are determined from a fit of the *ab initio* electrostatic potentials of the transition densities of the solute and solvent molecules, respectively. If a dipole approximation for solvent molecule C_ξ is used, Eq 2.76 becomes, using $\sum_J q_J^{(C_\xi)}(0,m_\xi) = 0$:

$$\langle A|\hat{V}_{AC_\xi}^{(\xi)}|C_{m_\xi}\rangle = \sum_{I} \frac{q_I^{(A)}(0,1)\mathbf{d}_{0m_\xi}^{(\xi)}(\mathbf{R}_I^{(A)} - \mathbf{R}_\xi)}{|\mathbf{R}_I^{(A)} - \mathbf{R}_\xi|^3}\,, \tag{2.77}$$

analog for B. The $\mathbf{R}_\xi$ points to the center of the ξth solvent molecule with transition dipole moment $\mathbf{d}_{0m_\xi}^{(\xi)} = \sum_J q_J^{(C_\xi)}(0,m_\xi)\mathbf{R}_J^{(C_\xi)}$. After inserting Eq 2.77 into Eq 2.75, we obtain

$$\delta V_{AB}^{(\mathrm{ex})} = \sum_\xi \sum_{I,J} q_J^{(B)}(0,1) q_I^{(A)}(0,1) \frac{(\mathbf{R}_J^{(B)} - \mathbf{R}_\xi)\hat{\alpha}_\xi(\mathbf{R}_\xi - \mathbf{R}_I^{(A)})}{|\mathbf{R}_J^{(B)} - \mathbf{R}_\xi|^3 |\mathbf{R}_I^{(A)} - \mathbf{R}_\xi|^3}\,, \tag{2.78}$$

where the polarizability tensor $\hat{\alpha}_\xi$ of the ξth solvent molecule was introduced. The tensor elements $(\alpha_\xi)_{ij}$ with $i,j = \{x,y,z\}$, are given as [50]:

$$(\alpha_\xi)_{ij} = 2\sum_{m_\xi} \frac{(d_{0m_\xi}^{(\xi)})_i (d_{0m_\xi}^{(\xi)})_j}{E_{m_\xi}}\,. \tag{2.79}$$

The interpretation of Eq 2.78 is as follows: The transition charges $q_I^{(A)}(0,1)$ of solute A produces an electric field $\mathbf{E}_I^{(A)}(\mathbf{R}_\xi) = q_I^{(A)}(0,1)(\mathbf{R}_\xi - \mathbf{R}_I^{(A)})/|\mathbf{R}_I^{(A)} - \mathbf{R}_\xi|^3$ at the location of the solvent molecule ξ. This field induces a dipole moment $\mathbf{p}_{I,A}^{(\xi)} = \hat{\alpha}_\xi \mathbf{E}_I^{(A)}$ in the solvent molecule. The latter interacts with the charge $q_J^{(B)}(0,1)$ of solute B to yield $\delta V_{AB}^{(\mathrm{ex})} = \sum_\xi \sum_J q_J^{(B)}(0,1)\phi_{I,A}^{(\xi)}(\mathbf{R}_J^{(B)})$ where $\phi_{I,A}^{(\xi)}(\mathbf{R}_J^{(B)}) =$

$\mathbf{p}_{I,A}^{(\xi)}(\mathbf{R}_J^{(B)} - \mathbf{R}_\xi)/|\mathbf{R}_J^{(B)} - \mathbf{R}_\xi|^3$ is the electrostatic potential of $\mathbf{p}_{I,A}^{(\xi)}$ at the Jth partial charge of solute B. The overall excitonic coupling thus may be written as

$$V_{AB}^{(\mathrm{ex})} = \sum_J q_J^{(B)}(0,1)\phi_I^{(A)}(\mathbf{R}_J^{(B)}) \tag{2.80}$$

where the electrostatic potential $\phi_I^{(A)}(\mathbf{R}_J^{(B)})$ reads

$$\phi_I^{(A)}(\mathbf{R}_J^{(B)}) = q_I^{(A)}(0,1)\left\{\frac{1}{|\mathbf{R}_I^{(A)} - \mathbf{R}_J^{(B)}|} + \sum_\xi \frac{(\mathbf{R}_J^{(B)} - \mathbf{R}_\xi)\hat{\alpha}_\xi(\mathbf{R}_\xi - \mathbf{R}_I^{(A)})}{|\mathbf{R}_I^{(B)} - \mathbf{R}_\xi|^3|\mathbf{R}_I^{(A)} - \mathbf{R}_\xi|^3}\right\}. \tag{2.81}$$

The first contribution on the right hand side reflects the direct coupling between solutes A and B and the second contribution contains the effect of the dielectric medium discussed above.

Eq 2.81 suggests the following calculation by using a continuum approximation for the solvent molecules. The potential $\phi_I^{(A)}$ is obtained from the solution of a Poisson equation

$$\nabla\left(\epsilon(\mathbf{r})\nabla\phi_I^{(A)}(\mathbf{r})\right) = -4\pi\sum_I q_I^{(A)}(0,1)\delta(\mathbf{r} - \mathbf{R}_I)\,, \tag{2.82}$$

where the atomic partial charges $q_I^{(A)}(0,1)$ are determined from the fit of the *ab initio* electrostatic potential of the transition density of solute A in vacuum. The $\epsilon(\mathbf{r})$ equals n^2, if $\mathbf{r}$ points to the solvent region, and one inside the molecule-shaped cavity. We note that only the electronic polarizability of the solvent (protein) needs to be taken into account, since the nuclei are frozen on the time-scale of an electronic transition (Franck-Condon principle).

Chapter 3

Calculation of Parameters

3.1 Spectral Density

The spectral density of exciton vibrational coupling $J(\omega) = \sum_\xi g_\xi^2 \delta(\omega - \omega_\xi)$ (Eq 2.4) describes how the configuration of nuclei of the protein changes upon electronic excitation of the pigment. The spectral density is related to the Huang-Rhys factor by

$$S = \int_0^\infty d\omega \, J(\omega) = \sum_\xi g_\xi^2. \tag{3.1}$$

Since the displacement of the minima of the potential energy surfaces of the two electronic states with respect to each other equals $-2g_\xi$ (Fig 3.1, *left*), the more this displacement, the larger S. The exciton-vibrational coupling is weak when $S \ll 1$, and strong when $S \gg 1$. The typical coupling in photosynthetic antenna complexes lies in an intermediate range, $S \approx 1$. If the potential energy surfaces are unshifted relatively to each other, the spectral density vanishes and the spectra do not contain vibrational sidebands.

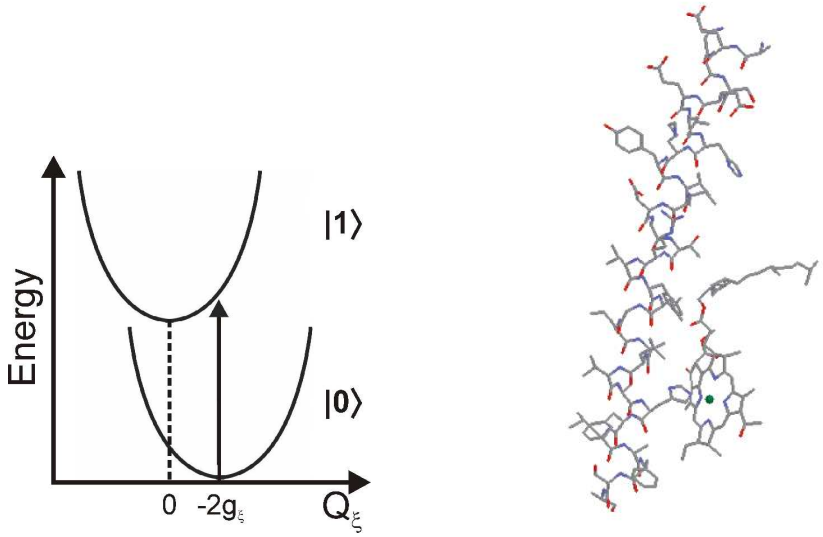

Figure 3.1: (*left*) Franck Condon transition with non-vanishing spectral density with negative g_ξ. (*right*) Model for the B777-complex. The model has been adapted from the atomic structure of the LH2 complex [51] (Brookhaven Protein Data file 1kzu.pdb), figure adopted from [30].

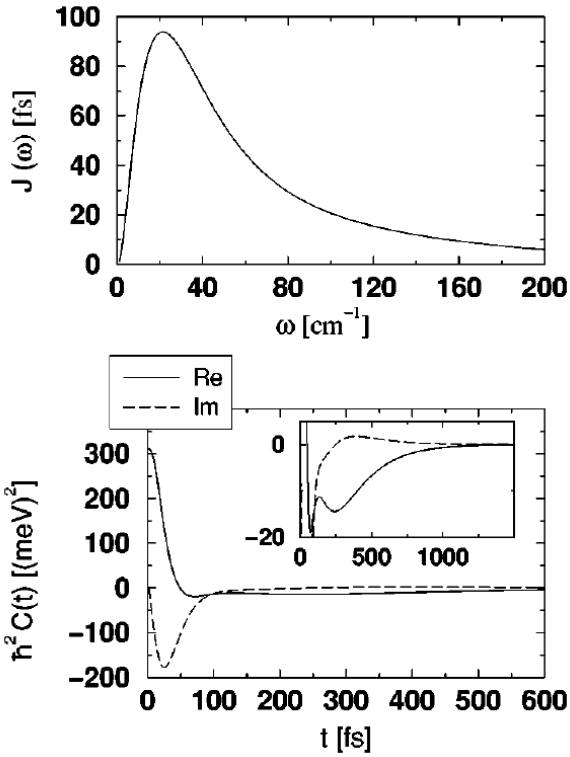

Figure 3.2: (*top*) Spectral density $J(\omega)$, extracted from the fit of fluorescence line narrowing spectra of the B777-complex. (*bottom*) Correlation function of the pigment transition energy of B777-complexes at $T = 1.6$ K. Solid and dashed lines show the real and imaginary parts, respectively. The inset in the lower half is a zoom into the small amplitude long time components of the correlation function. Figure adopted from [30].

3.1.1 Spectral Density Extracted from Fluorescence Line Narrowing Spectra

Renger and Marcus [30] used the B777-complex (Fig 3.1, *right*) as a model system to investigate the local interaction between a pigment and the protein in photosynthetic antennas. They extracted the spectral density of the pigment-protein interaction from 1.6 K fluorescence line narrowing spectra of B777-complexes, measured [52] at different excitation wavelength. They used an empirical functional form for $J(\omega)$ (see [30]) and determined it finally to

$$J(\omega) = \frac{1}{s_1 + s_2} \sum_{i=1,2} \frac{s_i}{7!\, 2\omega_i^4}\, \omega^3\, e^{-(\omega/\omega_i)^{1/2}} \tag{3.2}$$

with the extracted parameters $s_1 = 0.8$, $s_2 = 0.5$, $\hbar\omega_1 = 0.069$ meV and $\hbar\omega_2 = 0.24$ meV. The spectral density $J(\omega)$ from Eq 3.2 and the resulting correlation function $C(t)$, calculated from Eq 3.3 [30]

$$C(t) = \int_0^\infty d\omega\, \omega^2 \{(1 + n(\omega))J(\omega)e^{-i\omega t} + n(\omega)J(\omega)e^{i\omega t}\}, \tag{3.3}$$

is depicted in Fig 3.2 (adopted from [30]).

3.1.2 High Energy Mode

In the model we used in Adolphs and Renger [53], the spectral density $J(\omega)$ contains both a broad low frequency contribution $S_0 J_0(\omega)$ by the protein vibrations with Huang-Rhys factor S_0 and a single effective high-energy vibrational mode of the pigments with Huang-Rhys factor S_{H}

$$J(\omega) = S_0 J_0(\omega) + S_{\mathrm{H}}\, \delta(\omega - \omega_{\mathrm{H}})\,. \tag{3.4}$$

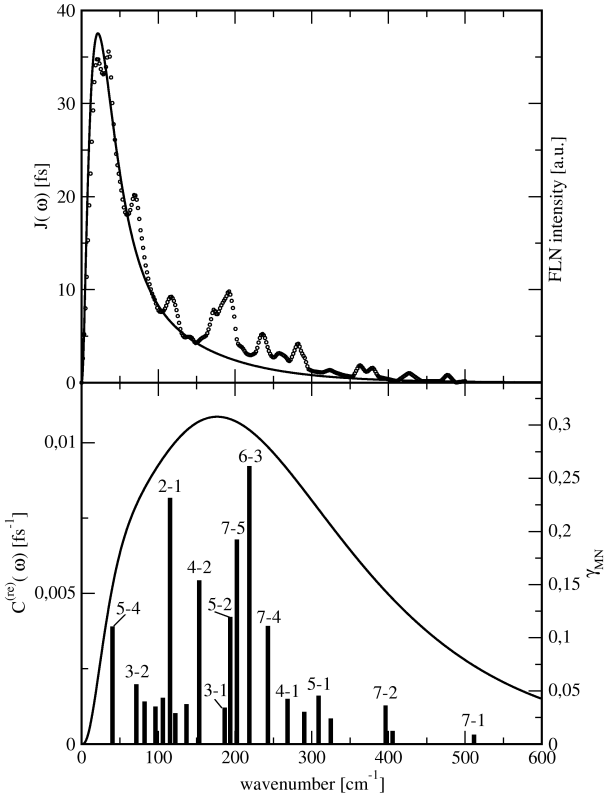

Figure 3.3: Upper part: Comparison of the low-frequency part $S_0 J_0(\omega)$ of the spectral density and the fluorescence line narrowing spectrum of *C. tepidum* [44]. Lower part: The function $\tilde{C}^{(\mathrm{Re})}(\omega)$ is shown that results from the $S_0 J_0(\omega)$ in the upper part (Eq 2.24). The factors γ_{MN} are shown as bars centered at the mean transition energy $\hbar\omega_{MN}$ between the exciton states. The numbers at the top of the bars show between which excitons M and N the transition takes place (in the FMO monomer).

For the normalized low-frequency function $J_0(\omega)$, i.e., $\int_0^\infty J_0(\omega)\, d\omega = 1$, we assume that it has the same form as $J(\omega)$ in Eq 3.2.

The Huang-Rhys factor S_0 of the pigment-protein coupling in Eq 3.4 was estimated from the temperature dependence of the absorption spectra [44, 54] of the FMO complexes of *P. aestuarii* and *C. tepidum* to be approximately 0.4. A comparison of the function $J_0(\omega)$ with the fluorescence line narrowing spectrum of *C. tepidum* [44] is shown in the upper part of Fig 3.3. The experimental spectrum (for the present weak exciton-vibrational coupling) should be similar [30] to the $J(\omega)$ in Eq 3.4. On the basis of this comparison, the Huang-Rhys factor and the energy of the high-frequency mode were estimated as $S_{\mathrm{H}} = 0.22$ and $\omega_{\mathrm{H}} = 180$ cm^{-1}. By taking into account that the energy of the high-frequency mode is large compared to the thermal energy (at $T = 5$ K), i.e., $\hbar\omega_{\mathrm{H}} \gg kT$, the function $G_M(t)$ in Eq 2.18 becomes, using Eqs. 2.19 and 3.4

$$\begin{aligned} G_M(t) &= \gamma_{MM}\ S_0 \int_0^\infty d\omega \left[(1+n(\omega))\, J_0(\omega)\, e^{-i\omega t} + n(\omega)\, J_0(\omega)\, e^{i\omega t} \right] + \gamma_{MM}\ S_{\mathrm{H}} e^{-i\omega_{\mathrm{H}} t} \\ &= G_M^{(0)}(t)\ +\ \gamma_{MM}\ S_{\mathrm{H}} e^{-i\omega_{\mathrm{H}} t} \end{aligned} \tag{3.5}$$

By introducing this $G_M(t)$ into Eq 2.17, using a series expansion for $\exp(\gamma_{MM} S_{\mathrm{H}} e^{-i\omega_{\mathrm{H}} t})$, the following lineshape function $D_M(\omega)$ is obtained

$$D_M(\omega) = e^{-S_{\mathrm{H}}\gamma_{MM}}\ \Re \int_0^\infty dt \sum_{k=0}^{\infty} \frac{(\gamma_{MM} S_{\mathrm{H}})^k}{k!} \cdot e^{i(\omega-(\tilde{\omega}_M + k\omega_{\mathrm{H}}))t}\, e^{G_M^{(0)}(t) - G_M^{(0)}(0)}\, e^{-t/\tau_M}\ . \tag{3.6}$$

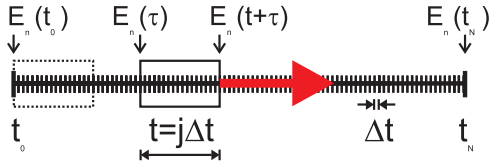

Figure 3.4: Calculation of the correlation function. The run with a fixed window size gives one point of the correlation function. To obtain the whole function the window size has to be varied from 0 to t_{max}.

The above $D_M(\omega)$ differs from the one obtained previously (Eq 2.17) in that it includes now also vibrational satellites of a high-frequency vibrational mode. The dephasing time τ_M of the Mth exciton transition and the off-diagonal part of the shift in transition energy $\sum_{N\neq M}\gamma_{MN}\tilde{C}^{(\mathrm{Im})}(\omega_{MN})$ in Eq 2.25 are determined by the low frequency contribution $S_0J_0(\omega)$ of the spectral density.

3.1.3 Spectral Density from Molecular Dynamics Simulation

The correlation function $C_{mn}(t)$ of the time-dependent site energies $E_m(t)$ and $E_n(t)$ reads [30]

$$C_{mn}(t) = \frac{1}{\hbar^2}\langle\, \delta E_m(t)\, \delta E_n(0)\,\rangle, \tag{3.7}$$

where $\langle \dots \rangle$ denotes an average over all trajectories. Both cases $m \neq n$ and $m = n$ (auto-correlation) are possible. The $\delta E_m(t)$ is the deviation of $E_m(t)$ from the mean value $\langle E_m\rangle$,

$$\delta E_m(t) = E_m(t) - \langle E_m\rangle, \tag{3.8}$$

and can be calculated (in discrete form) according to

$$\langle E_m\rangle = \frac{1}{N_T}\sum_{i=1}^{N_T} E_m(t_i) \tag{3.9}$$

where N_T is the number of time steps Δt and $t_i = i\cdot\Delta t$. Application of the *ergodic theorem*[1] on Eq 3.7 leads to

$$C_{mn}(t) = \frac{1}{\hbar^2}\lim_{T\to\infty}\frac{1}{T}\int_0^T d\tau\ \delta E_m(t+\tau)\ \delta E_n(\tau), \tag{3.10}$$

where T is the length of the time-trace and t is the variable time window. In discrete form it reads:

$$C_{mn}(t_j) = \frac{1}{\hbar^2 N_T}\sum_{i=1}^{N_T-j}\delta E_m(t_j+t_i)\ \delta E_n(t_i). \tag{3.11}$$

The argument of the correlation function, i.e., t (or $t_j = \Delta t\cdot j$ in discrete form) must be considered as time-window, which is shifted over the hole trajectory to calculate the (auto-) correlation between the site energy at all times τ and all times $\tau + t$ by integrating over τ, see Fig 3.4. For one window size t this gives only one point of the (auto-) correlation function $C(t)$. To get the hole function for an interval $[t, t_{max}]$, one has to calculate the (auto-) correlation function for all possible window sizes. The time-dependent site energies $E_m(t)$ can be calculated for each time step of a molecular dynamics simulation very efficiently and sufficiently with the **Charge Density Coupling Method**, that will be introduced in section 3.3.2. The site energies $E_m(t)$ are obtained from Eq 3.36, where the time-dependent atom positions $r_I^{(m)} = r_I^{(m)}(t)$ and $r_J^{(\mathrm{bg})} = r_J^{(\mathrm{bg})}(t)$ are obtained from molecular dynamics simulations.

[1] **Ergodic theorem:** In the case of ergodicity (trajectory comes arbitrary close to every phase-space point), the phase-space mean is equal to the time mean.

Extraction of the Spectral Density

From a semi-classical harmonic oscillator approach, a classical correlation function can be obtained [55, 56] as:

$$C_{\mathrm{cl}}(t) \approx \frac{2kT}{\hbar} \int_0^\infty d\omega \, J(\omega) \, \omega \, \cos(\omega t), \tag{3.12}$$

which is also known as Wiener-Khintchin theorem. It is valid only for high temperatures, which is the case in usual MD-simulations. The above relation (Eq 3.12) between $C_{\mathrm{cl}}(t)$ and $J(\omega)$ will be used to extract $J(\omega)$ from classical molecular dynamics simulations of the FMO complex, and has been used before by Warshel & Hwang [55] to extract a spectral density of electron transfer. A Fourier transformation $\tilde{C}_{\mathrm{cl}}(\bar{\omega}) = \mathrm{FT}\{C_{\mathrm{cl}}(t)\}$ of Eq (3.12) together with Euler's formula leads to:

$$\tilde{C}_{\mathrm{cl}}(\bar{\omega}) = \int_{-\infty}^{+\infty} dt \, e^{-i\bar{\omega}t} \, C_{\mathrm{cl}}(t) = \frac{kT}{\hbar} \int_0^\infty d\omega \, J(\omega) \, \omega \int_{-\infty}^{+\infty} dt \, (e^{i\omega t} + e^{-i\omega t}) \, e^{-i\bar{\omega}t}. \tag{3.13}$$

The second integral of the right hand side can be written as[2]:

$$\int_{-\infty}^{+\infty} dt \, e^{-i(\bar{\omega}-\omega)t} + \int_{-\infty}^{+\infty} dt \, e^{-i(\bar{\omega}+\omega)t} = 2\pi \, [\, \delta(\bar{\omega}-\omega) + \delta(\bar{\omega}+\omega) \,]. \tag{3.14}$$

For the Fourier transformed correlation function follows:

$$\begin{aligned} \tilde{C}_{\mathrm{cl}}(\bar{\omega}) &= \frac{2\pi kT}{\hbar} \int_0^\infty d\omega \, J(\omega) \, \omega \, [\, \delta(\bar{\omega}-\omega) + \delta(\bar{\omega}+\omega) \,] \\ &= \frac{2\pi kT}{\hbar} \, [\, J(\bar{\omega}) \, \bar{\omega} - J(-\bar{\omega}) \, \bar{\omega} \,]. \end{aligned} \tag{3.15}$$

Having in mind that $J(-\omega) = 0$ and replacing $\bar{\omega}$ by ω and $\tilde{C}$ by C, we get an equation for the computation of the spectral density via the classical correlation function of site energies calculated by MD simulations:

$$J(\omega) = \frac{\hbar}{2\pi kT} \frac{C(\omega)}{\omega}, \tag{3.16}$$

where $C(\omega) = C_{\mathrm{cl}}(\omega)$.

Correlation Radius

The correlation radius R_c of protein vibrations has been introduced in Eq 2.20. Up to now R_c was assumed to be around 5 Å [30]. For the relation between $C_{mn}(t)$ and $C_{mm}(t)$ we assume $C_{mn}(t) = \exp(-\frac{R_{mn}}{R_c}) \cdot C_{mm}(t)$ for $m \neq n$, where R_{mn} is the center to center distance between pigments m and n. With the correlation functions $C_{mn}(t)$ for $m \neq n$ and $m = n$ from MD we will be able to prove or disprove the upper relation, and if it fits it will yield the correlation radius R_c.

Summary

From the autocorrelation function $C(t) = C_{mm}(t)$ the spectral density $J(\omega)$ can be extracted. Assuming $C_{mn}(t) = \exp(-\frac{R_{mn}}{R_c}) \cdot C_{mm}(t)$ for $m \neq n$ will yield the correlation radius R_c. In general the correlation function has the property $C_{mn}(t) \neq C_{nm}(t)$.

[2] For the Dirac delta function one possible representation is: $\int_{-\infty}^{+\infty} e^{-i\omega t} \, dt = 2\pi \, \delta(\omega)$

3.2 Excitonic Couplings

In 1948 Förster suggested a mechanism that is able to transfer excitation between molecules [28]. He related the rate constant of this transfer mechanism to the overlap of the fluorescence spectrum of the donor and the absorption spectrum of the acceptor. The Coulomb coupling of the electrons of the excited molecule with those of the molecule in the ground state induce the excitation energy transfer, due to Förster. The respective coupling matrix element is given by the coupling between the transition dipole moments of the molecules. Since structural information of corresponding complexes is available, excitation energy transfer in photosynthesis can be understood in molecular detail. If the intermolecular distances between photosynthetic pigments are in the range or even smaller than the pigments extension, additional short-range contributions to the matrix element can be expected, which have two reasons: electron exchange between the molecules, first mentioned by Dexter [29], and the point dipole approximation fails for the Förster coupling matrix element.

By means of the innovative work of Weiss [57] and Chang [58] quantitative corrections for the convenient point dipole approximation for the Förster coupling matrix element became available. The point dipole approximation is achieved from a multipole expansion of the transition densities of the interacting molecules. It is only valid if the extension of the molecular wave function is small compared to the distance between the molecule centers.

While for the point dipole approximation only information about geometry and strength of the molecular transition dipole elements and the intermolecular distances is needed, for the more exact method of Weiss and Chang, so-called transition monopole charges are introduced. Those are obtained from semi-empirical quantum chemical calculations, using a self consistent field method. These transition monopoles reflect the transition density of a molecule, which has no classical analogue. It contains a product of ground and excited-state wave functions, instead of an absolute square of a wave function, as an ordinary charge density. The excitation energy transfer coupling can simply be calculated as the Coulomb coupling between the transition charges of one molecule with those of the other, i.e., it can easily be applied if the transition charges are known.

3.2.1 Excitonic Coupling in Vacuum

The excitonic coupling V_{mn} between a pigment in an excited electronic state and a pigment in the ground-state, introduced in Eq 2.2, is conveyed by Coulomb coupling. The respective matrix elements of excitation energy transfer reads:

$$V_{mn} = \langle\, \psi_{m'}\, \psi_n \,|\, V_{\text{Coulomb}} \,|\, \psi_m\, \psi_{n'} \,\rangle \tag{3.17}$$

where $\psi_{m/n}$ denote the ground and $\psi_{m'/n'}$ the excited state wavefunctions of pigment m/n. V_{Coulomb} is the Coulomb coupling between both, electrons and nuclei of the two pigments.

Point Dipole Approximation

If the extension of the electronic wavefunction of pigments is small compared to their center to center distance, V_{Coulomb} can be Taylor expanded, and the first non-zero term of this Taylor series is the point dipole approximation, where the excitonic coupling is given as

$$V_{mn} = \frac{\mu^2_{\text{eff}}}{R^3_{mn}} \left[\vec{e}_m \cdot \vec{e}_n - 3\,(\vec{e}_m \cdot \vec{e}_{mn})(\vec{e}_n \cdot \vec{e}_{mn})\right] \tag{3.18}$$

where $\vec{e}_m$ is a unit vector along the transition dipole moment of the mth pigment, the unit vector $\vec{e}_{mn}$ is oriented along the line connecting the centers of pigments m and n, and $\mu^2_{\text{eff}} = f \cdot \mu^2_{vac}$ is the effective dipole strength of the Q_y transition of BChl*a* (see section 3.2.2).

In Eq 3.18 the excitonic coupling is expressed as dipole-dipole coupling between optical transition dipoles. These transition dipoles are an approximation for the quantum mechanical transition density,

which has no classical analoge (see below). The orientation and position of pigments transition dipoles can be obtained from structural data. The orientation of the Q_y transition dipole moment of (bacterio)chlorophylls is approximately along the N_B-N_D axis (Fig 1.2) of the molecules [49]. The dipole strength are estimated from optical spectra measured for (bacterio)chlorophylls in different solvents [18].

Extended Dipole Approximation

A first improvement of the point dipole approximation, is the extended dipole approximation. This approximation considers a certain extend of the pigments electronic wavefunctions, by placing two partial charges of opposite sign $\pm\delta q_m$ in a certain distance l on the transition dipole direction (N_B-N_D axis). The charges $\pm\delta q_m$ have to be chosen as to achieve $|\mu_m| = l\,|\delta q_m|$ with $|\mu_m|$ of the optical transition. The excitonic coupling is given by the Coulomb interaction between the point charges of pigment m and n:

$$V_{mn} = \sum_{i,j=\pm} ij\,\frac{\delta q_m\,\delta q_n}{|r_m^i - r_n^j|} \tag{3.19}$$

where $ij = \begin{cases} +1 & i = j \\ -1 & i \neq j \end{cases}$ and $|r_m^i - r_n^j|$ is the distance between the partial charges $\pm\delta q_m$ and $\pm\delta q_n$.

Transition Density

A general expression for the excitonic coupling can be calculated by a quantum chemical method. The coupling V_{mn} is written as a Coulomb coupling between transition densities:

$$V_{mn} = \int d\vec{r}_1\,d\vec{r}_2\,\frac{\rho_m(\vec{r}_1)\,\rho_n(\vec{r}_2)}{|\vec{r}_1 - \vec{r}_2|} \tag{3.20}$$

where the transition density of pigment m is defined as integral over the product of ground and excited state wavefunctions ψ_m and $\psi_{m'}$ [49, 59, 60]:

$$\begin{aligned} \rho_m(\vec{r}_1) &= \int_s ds \int d\vec{r}_2 \cdots d\vec{r}_N\ \psi_m(\vec{r}_1, \vec{r}_2, \ldots \vec{r}_N) \cdot \psi^*_{m'}(\vec{r}_1, \vec{r}_2, \ldots \vec{r}_N) \\ &= \quad N \int d\vec{r}_2 \cdots d\vec{r}_N\ \psi_m(\vec{r}_1, \vec{r}_2, \ldots \vec{r}_N) \cdot \psi^*_{m'}(\vec{r}_1, \vec{r}_2, \ldots \vec{r}_N)\,, \end{aligned} \tag{3.21}$$

where the integration is performed over the N spin coordinates and the $N-1$ spatial coordinates.

After calculation of the transition densities by a quantum chemical method, there are several opportunities to determine the excitonic couplings. One possibility is to approximate the coupling of Eq 3.20 by discrete transition charges of the two pigments. These charges can be obtained from the transition densities by integration over particular volume elements. The oldest approach is the so-called transition monopole method of Weiss [57] and Chang [58]. They calculated transition charges for each atom of a pigment, using a semi-empirical Pariser-Parr-Pople method.

The transition density cube method of Krueger *et al.* [61] fractionizes the space around the pigment into cubes and solves the integral of Eq 3.20 numerically on that three dimensional grid. Roughly half a million cubes are required for one (bacterio)chlorophyll pigment to reach convergence of the integral. The latest method of Madjet *et al.* [49], the so-called TrEsp-method, determines atomic transition charges by fitting the electrostatic potential of point charges to the electrostatic potential of the quantum chemical transition density. Because the couplings from the transition density cube method converge for small cubes against the TrEsp couplings [49], this method contains the full information of the ab initio transition density. Therefore it is more accurate than the transition monopole method, even though the coupling calculations finally need the same relatively small effort, compared with the high numerical effort of the transition density cube method.

3.2.2 Dielectric Environment

Although the excitonic couplings, in contrast to the site energies, can be calculated straightforwardly from the structural data, there is an unknown scaling factor that contains the uncertainty about the effect of the dielectric environment on the Coulomb (excitonic) interaction:

$$V_{mn} = f \cdot V_{mn}^{(\text{vacuum})}. \tag{3.22}$$

The factor f describes the enhancement of the dipole strength[3] and the screening of the Coulomb coupling by the dielectric environment with optical dielectric constant ε, where μ_{vac}^2 is the dipole strength of the Q_y transition of BChl*a* (Chl*a*) in vacuum and $(\mu(\varepsilon))^2$ in the dielectric,

$$f = g \cdot \left(\frac{\mu(\varepsilon)}{\mu_{\text{vac}}} \right)^2 . \tag{3.23}$$

If the distance between the pigments is large compared to the extension of their ground and excited state wavefunctions, the screening factor g equals $1/\varepsilon$, which is the case for the empty cavity situation. The dipole strength of a point dipole μ in a spherical cavity in a dielectric medium is enhanced to [62]: $\mu = \frac{3\varepsilon}{2\varepsilon+1} \cdot \mu_{\text{vac}}$ (empty cavity model). In the simplest approximation the factor f for two interacting point dipoles in spherical cavities, both dipoles are enhanced by the empty cavity factor, the interaction is screened by $1/\varepsilon$ and the therefore the effective (shielding included) empty cavity factor is then just the product of all factors: $f = \frac{9\varepsilon}{(2\varepsilon+1)^2}$. If two pigments are very close, it can be expected that the factor f becomes distance dependent, because the two pigments do not form separate cavities with dielectric medium in between but are rather situated in the same cavity. As pointed out by Knox and van Amerongen [63] the enhancement of the dipole strength, i.e. the change in quantum mechanical transition probability by the dielectric can be classically understood by the change of local electric field interacting with the vacuum transition dipole. Recently, Knox and Spring [18] analyzed the dipole strength of BChl*a* in 15 different solvents and found the empirical relation $(\mu(\varepsilon))^2 = (43.3 + 24.2(\sqrt{\varepsilon} - 1))\ \text{D}^2$ between the dipole strength $(\mu(\varepsilon))^2$ in the solvent with dielectric constant ε and the vacuum value $(\mu(1))^2$. If this empirical formula is compared with the predictions of two cavity models, the empty cavity model was found to provide the best explanation [18]. Within the latter, the dipole strength of BChl*a* in the solvent is obtained as $(\mu(\varepsilon))^2 = 37.1 \cdot (3\varepsilon/(2\varepsilon + 1))^2\ \text{D}^2$, that contains the vacuum dipole strength $\mu_{\text{vac}}^2 = (\mu(1))^2 = 37.1\ \text{D}^2$. For the dipole strength of Chl*a*, they [18] analyzed the dipole strength in 43 different solvents and fount the relation $(\mu(\varepsilon))^2 = (20.2 + 23.5(\sqrt{\varepsilon} - 1))\ \text{D}^2$. The extracted vacuum dipole strength for Chl*a* is $\mu_{\text{vac}}^2 = 21.0\ \text{D}^2$.

3.2.3 Test Case – Comparison with Results from Literature

In a recent study Hsu *et al.* [64] demonstrated that the excitonic coupling between two molecules in a dielectric environment that results from a quantum mechanical treatment using time dependent density functional theory, can be obtained also classically. The classical calculation just involves the electrostatic coupling between the transition densities of the two molecules taking into account the fast (optical) part of the dielectric response of the medium. Hsu *et al.* [64] showed, using a multipole expansion, that the interaction between two transition dipoles in a spherical cavity can be either increased or decreased by the dielectric response of the environment, depending on the geometry of the transition dipoles. As described in detail below the present method is based on a numerical solution of the Poisson equation and allows thereby to treat also non-spherical cavities, as those of the BChls in the FMO-protein. We have tested our numerical procedure by reproducing the spherical cavity results of Hsu *et al.*, as shown in Fig 3.5. In this calculation, the transition dipoles are represented by two transition charges of opposite sign

[3] Here we use the usual but non-SI unit D (Debye), respectively D^2 for the (electric) dipole strength. The conversion to SI units follows 1 D$= 3.33564 \cdot 10^{-30}$ Cm. Primary definition: a positive and a negative elementary charge, separated by 1 Å, have a dipole moment of 4.8 D.

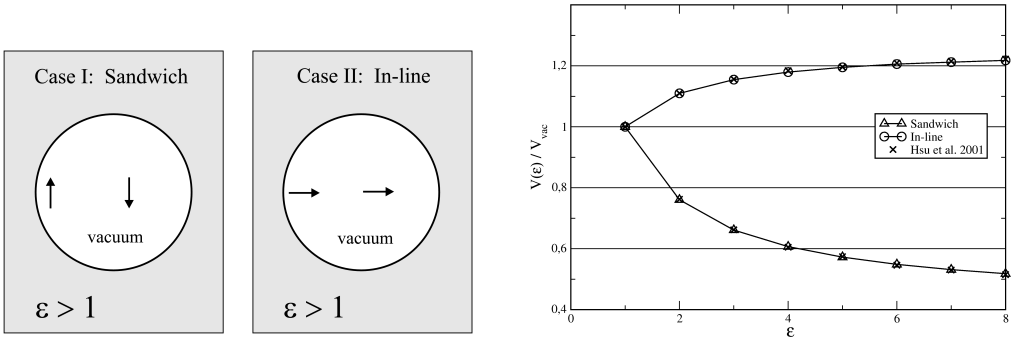

Figure 3.5: Left part: Sketch of the spherical cavity containing two transition dipoles with different geometries: The dipoles are located at (-0.8,0,0) and (0.1,0,0), the cavity radius equals 1. Right part: Ratio of the Coulomb coupling obtained for different dielectric constants ($\varepsilon > 1$) and the Coulomb coupling in vacuum ($\varepsilon = 1$) for the two geometries in the left part. The values obtained earlier by Hsu *et al.* [64] using a multipole expansion are shown also.

at close distance. The two geometries are depicted in the left part of Fig 3.5 and the resulting couplings are shown in the right part in dependence on the dielectric constant.

3.2.4 Calculation of the Couplings

The excitonic couplings are obtained from the Coulomb couplings between the transition densities of the BChls. To take into account the influence of the dielectric we introduced the following method [53], based on the theoretical considerations of section 2.2. A dielectric volume of the protein is created from overlapping spheres of its atoms with atomic radii taken from the CHARMM22 force field [65]. The transition density of BChl m, is described by atomic transition charges $q_I^{(m)}(1,0)$ that are located in the respective cavities in the FMO protein, $\rho_m(\vec{r}) = \sum_I q_I^{(m)}(1,0)\,\delta(\vec{r} - \vec{R}_I^{(m)})$. An optical dielectric constant of $\varepsilon = 2$ is assumed for the protein and $\varepsilon = 1$ (i.e. vacuum) for the BChl cavities. The transition charges are rescaled such as to result in the correct magnitude of the vacuum transition dipole moment magnitude of 6.1 D as determined in an empty cavity analysis by Knox & Spring [18] from absorption data of BChl*a* in different solvents. The Poisson equation

$$\nabla \cdot [\varepsilon(\vec{r})\,\nabla\phi_m(\vec{r})] = -4\pi \sum_I q_I^{(m)}\,\delta(\vec{r} - \vec{R}_I^{(m)}) \tag{3.24}$$

is solved for each BChl numerically by a finite difference method using the program MEAD [66]. The value of $\varepsilon(\vec{r})$ equals 2 if $\vec{r}$ points to a position in the protein and 1 in the case of BChl. From the resulting electrostatic potential $\phi_m(\vec{r})$ of the transition density of BChl m, the excitonic coupling with BChl n is given as [53]

$$V_{mn} = \int d\vec{r}\,\phi_m(\vec{r})\,\rho_n(\vec{r}) = \sum_I \phi_m(\vec{R}_I^{(n)})\,q_I^{(n)}(1,0) \tag{3.25}$$

In a first approach [53] the atomic transition monopole (TM) charges q_I of Chang [58] were used for the transition charges $q_I^{(m)}$(1,0). In a second approach [67] the transition charges $q_I^{(m)}$(1,0) are obtained from a fit of the electrostatic potential of the transition density (TrEsp, [49]), obtained with time dependent density functional theory using a 6-31G* basis set and a B3LYP exchange correlation (XC) functional. A geometry optimization is performed, constraining the torsional angle of the 3-acetyl group to its value in the crystal structure [23] to study the influence of the acetyl group orientation of the BChls on the excitonic coupling. Alternatively, the coupling is calculated with transition charges obtained for fully geometry optimized BChl*a* [49]. In this case, all BChls carry the same set of charges $\{q_I\}$. The

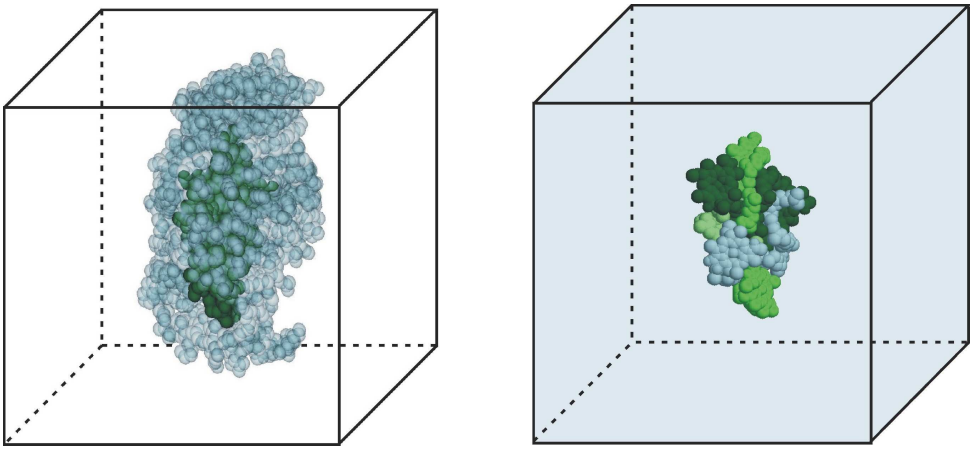

Figure 3.6: Dielectric volume considered in the calculations of excitonic couplings. *(Left)* The pigments are surrounded by protein with $\varepsilon = 2$, outside of the protein ε equals 1. *(Right)* The BChls are surrounded by protein and solvent, both described by $\varepsilon = 2$. In both cases the BChl shaped cavities have $\varepsilon = 1$ inside.

quantum chemical calculations were performed with the programs [68] and QChem [69] and the fit of the electrostatic potential with the CHELP-BOW program [70].

In a simplified version of the method, the polarizability of the solvent is taken into account, using the same optical dielectric constant $\varepsilon = 2$ as for the protein. In this case, there is no need to create a dielectric volume of the protein, and the BChls are modeled as vacuum cavities containing the TrEsp charges in the homogeneous dielectric. The simplified model together with the TrEsp charges for Chl*a* is also applied on the central part of photosystem I. The two different types of dielectrics are illustrated in Fig 3.6.

The results obtained by the above methods are compared with the simple point dipole approximation of Eq 3.18. It will be investigated, which value of f gives the closest agreement with the values obtained from the electrostatic calculations above. We note that in general f is distance and orientation dependent [71].

Finally, we note that the Knox/Spring analysis of the dipole strengths was limited to the $0-0$ transition of the BChl*a* Q_y transition, i.e., it does not include excitations of intramolecular vibrations (see also section 3.2.5). To take into account excitonic couplings that involve intramolecular vibrational transitions would require to include those vibrational modes via the respective Franck-Condon factors explicitly in the theory (see e.g. [72, 73]), which is beyond the scope of this study.

3.2.5 Dipole Strength

The vacuum dipole strength $\mu^2_{(0-0)} = 37.1\,\mathrm{D}^2$ from Knox & Spring [18] is limited to the 0–0 transition, i.e., the excitation of intramolecular vibration is not included. Therefore a legitimate question is, whether we have to use this vacuum dipole strength of $37.1\,\mathrm{D}^2$, if we take into account only the 0–0 transition in the simulation of spectra, or if we have to use the accumulated dipole strength of the 0–0 and 0–1 transition united on the 0–0 transition, i.e. $\mu^2 = \mu^2_{(0-0)} + \mu^2_{(0-1)}$.

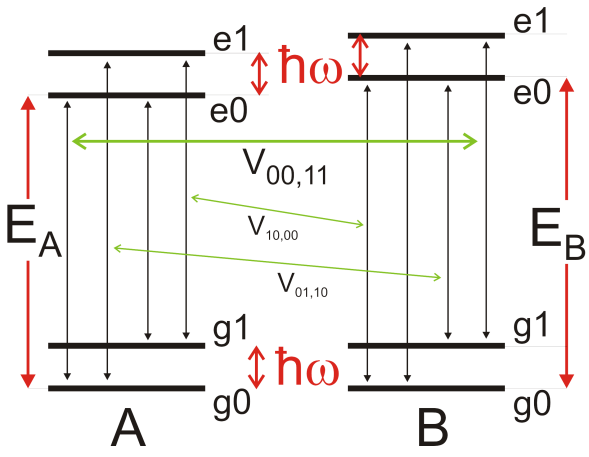

Figure 3.7: Two pigments A and B, each having a vibrational level in the ground and excited electronic state. Black arrows: possible transitions. Green arrows: selected excitonic couplings between transitions.

Two excitonically coupled pigments with each having a vibrational ground and excited level in the electronic ground and excited state (Fig 3.7) will have dimer eigenstates that reflect the excitonic couplings between the different transitions. Since the 0–0 transitions couple strongest they will show the largest splitting and the transitions involving vibrational levels will not be splitted that much (by coupling with a transition of the other molecule) because of their low dipole strength. So, increasing the dipole strength of the 0–0 transition would put the oscillator strength in a different place of the spectrum than by explicitly including the vibrational transitions in the diagonalization procedure.

In the following dimer calculations are performed to investigate this point in detail. For this purpose we study a dimer where one vibrational level for the ground and excited state is taken into account. The vibrational frequency is set to 180 cm^{-1}, taken from [44], see Fig 3.3. The matrix of excitonic couplings between all possible transitions and the energies of respective states is presented in Table 3.1. Notation: $|\mathrm{A\,g0}\rangle$ stands for molecule A in electronic and vibrational ground state, $|\mathrm{A\,g1}\rangle$ means molecule A is in electronic ground and vibrational excited state, $|\mathrm{A\,g0}\rangle$ means molecule A is in electronic excited and vibrational ground state and $|\mathrm{A\,g1}\rangle$ means molecule A is in electronic and vibrational excited state, analog for molecule B.

The diagonal elements of the left upper and right lower rectangle of the matrix in Table 3.1 do not belong to transitions but are the energy of the actual state. For instance the (4,4)-entry ($E_\mathrm{B} + 2\hbar\omega$) is the energy of molecule A in electronic ground state and vibrational excited state $|\mathrm{A\,g1}\rangle$, which amounts to $\hbar\omega$ and the energy of molecule B in electronic and vibrational excited state $|\mathrm{B\,e1}\rangle$, which amounts to $E_\mathrm{B} + \hbar\omega$, see Fig 3.7.

In the right upper and left lower rectangle the respective excitonic couplings are listed. For example the excitonic coupling $V_{00,11}$ is the excitonic coupling of the transition of pigment A between $|g0\rangle$ and $|e0\rangle$ and pigment B between $|g1\rangle$ and $|e1\rangle$ (Fig 3.7). The matrix elements $V_{ij,mn}$ with $i,j,m,n = \{0,1\}$ of Table 3.1 can be calculated with the Franck-Condon factors of Eq 3.27 as shown exemplary in Eq 3.26

$$V_{00,11} = \langle \mathrm{Ag0\ Be1}|V|\mathrm{Ae0\ Bg1}\rangle = \langle\chi_{\mathrm{g0}}|\chi_{\mathrm{e0}}\rangle_\mathrm{A}\langle\chi_{\mathrm{e1}}|\chi_{\mathrm{g1}}\rangle_\mathrm{B}\langle \mathrm{Ag\ Be}|V|\mathrm{Ae\ Bg}\rangle, \tag{3.26}$$

where $\langle \mathrm{Ag\ Be}|V|\mathrm{Ae\ Bg}\rangle$ is calculated as explained in section 3.2 and the Franck-Condon factors are obtained as (see e.g. [31]):

$$\langle\chi_{\mathrm{g}M}|\chi_{\mathrm{e}N}\rangle = e^{-S/2}\sum_{m=0}^{M}\sum_{n=0}^{N}\frac{(-1)^n\sqrt{S^n}\sqrt{S^m}}{m!\,n!}\sqrt{\frac{M!\,N!}{(M-m)!\,(N-n)!}}\delta_{M-m,N-n}, \tag{3.27}$$

where e, g is the electronic index (here ground and excited state), N, M is the number on vibrational quanta, in our case $N, M = \{0,1\}$ and S is the Huang-Rhys factor of the vibrational level. For $M = N$

Table 3.1: Matrix of excitonic couplings. $\omega = 180$ cm^{-1} is the vibration frequency of the vibrational mode.

	A g0 B e0	A g0 B e1	A g1 B e0	A g1 B e1	A e0 B g0	A e0 B g1	A e1 B g0	A e1 B g1
A g0 B e0	E_{B}	0	0	0	$V_{00,00}$	$V_{00,01}$	$V_{01,00}$	$V_{01,01}$
A g0 B e1	0	$E_{\mathrm{B}} + \hbar\omega$	0	0	$V_{00,10}$	$V_{00,11}$	$V_{01,10}$	$V_{01,11}$
A g1 B e0	0	0	$E_{\mathrm{B}} + \hbar\omega$	0	$V_{10,00}$	$V_{10,01}$	$V_{11,00}$	$V_{11,01}$
A g1 B e1	0	0	0	$E_{\mathrm{B}} + 2\hbar\omega$	$V_{10,10}$	$V_{10,11}$	$V_{11,10}$	$V_{11,11}$
A e0 B g0	$V_{00,00}$	$V_{00,01}$	$V_{01,00}$	$V_{01,01}$	E_{A}	0	0	0
A e0 B g1	$V_{00,10}$	$V_{00,11}$	$V_{01,10}$	$V_{01,11}$	0	$E_{\mathrm{A}} + \hbar\omega$	0	0
A e1 B g0	$V_{10,00}$	$V_{10,01}$	$V_{11,00}$	$V_{11,01}$	0	0	$E_{\mathrm{A}} + \hbar\omega$	0
A e1 B g1	$V_{10,10}$	$V_{10,11}$	$V_{11,10}$	$V_{11,11}$	0	0	0	$E_{\mathrm{A}} + 2\hbar\omega$

the Franck-Condon factors simplify to

$$\langle \chi_{\mathrm{g}M} | \chi_{\mathrm{e}M} \rangle = e^{-S/2} \sum_{m=0}^{M} \frac{(-S)^m}{(m!)^2} \frac{M!}{(M-m)!} \tag{3.28}$$

With Eq 3.27 and 3.28 we determine the required Franck-Condon factors to:
$\langle \chi_{\mathrm{g0}} | \chi_{\mathrm{e0}} \rangle = e^{-S/2}$, $\langle \chi_{\mathrm{g1}} | \chi_{\mathrm{e1}} \rangle = e^{-S/2}(1-S)$, $\langle \chi_{\mathrm{g0}} | \chi_{\mathrm{e1}} \rangle = -e^{-S/2}\sqrt{S}$, $\langle \chi_{\mathrm{g1}} | \chi_{\mathrm{e0}} \rangle = e^{-S/2}\sqrt{S}$.

Without vibrational levels the 8×8-matrix in Table 3.1 reduces to the 2×2 exciton matrix for two pigments described in Eq 2.2. Then the diagonal elements are the site energies and the non-diagonal elements are the usual excitonic couplings explained earlier in this chapter.

With the matrix in Table 3.1, Eq 3.26 and Eq 3.27 we performed calculation of dimer spectra (Gauss-dressed stick-spectra) with and without excitonic coupling for the case with vibrational level in ground and excited state (Fig 3.8, black lines). To elucidate whether it is better to use the 0 – 0 dipole strength in the calculation or the accumulated dipole strength of the 0 – 0 and 0 – 1 transition, calculation without vibrational level with the 0 – 0 dipole strength (37.1 D^2) (Fig 3.8, green lines) and the accumulated 0 – 0 and 0 – 1 dipole strength (1.25·37.1 D^2)[4] have been performed (Fig 3.8, green lines). The calculations were done for the BChl 1 – BChl 2 dimer of the FMO complex from *C. tepidum* with strong coupling, taking into account the site energies (12410 and 12530 cm^{-1}) from the genetic fit (Table 4.3, Trimer).

Both calculations deviate from the result with vibrational levels. However, it seems that just taking into account the dipole strength of the 0 – 0 transition provides a better description of the spectral position of the two main bands.

Increasing the effective dipole strength would also add to the life time broadening of the 0 – 0 transition in an artificial way.

[4] Knox & Spring [18] alert that the dipole strengths they reported are the 0 – 0 strengths and that the remainder of the Q_y band strength is around 20 %. We interpret that they mean a relation of 80 % dipole strength belong to the 0 – 0 transition and 20 % to 0 – 1 and (higher) transitions. Hence we chose the Huang-Rhys factor to S=0.25.

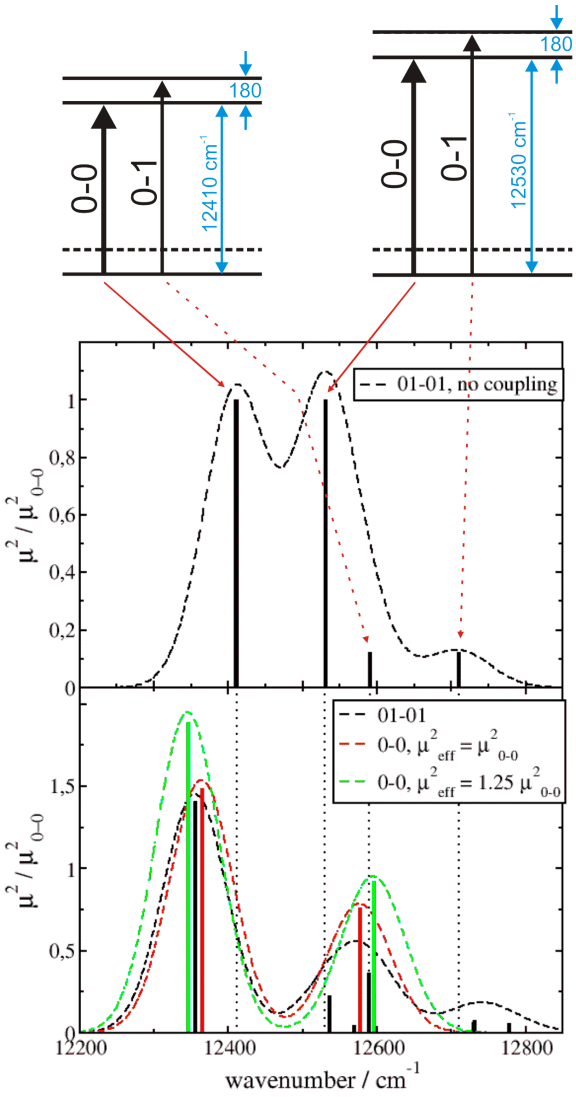

Figure 3.8: (*Top*) Energy scheme for two pigments with vibrational level in the electronic ground and excited level. (*Center*) Solution with vibrational levels for couplings *switched off*, site energies 12410 and 12530 cm^{-1}, vibrational levels +180 cm^{-1}. (*Bottom*) Three possible results for couplings *switched on* and same site energies as in *center*.

3.2.6 Systematic Study of Couplings in Dielectric

Here the idea is to investigate the influence of the dielectric medium on the pigment-pigment-coupling in a systematic way to eventually find a rule how the influence of the dielectric can be effectively included in the calculation of pigment couplings in vacuum. The factor of 0.8, estimated before for FMO is in principle only valid for strongly coupled pigments (which are dominating the spectra of FMO), and a more general factor would be very useful. Scholes *et al.* [71] recently published a distance dependent factor $s(r)$ (Eq 3.29), based on an exponential function, resulting from elaborate quantum chemical calculations for 100 pairs of molecules in four different photosynthetic proteins.

$$s(r) = \frac{V_{\text{med}}}{V_{\text{vac}}} = A\, e^{-\beta r} + s_0, \qquad \text{with} \quad A = 2.68,\ \beta = 0.27,\ s_0 = 0.54. \tag{3.29}$$

As our calculations will show, beside the distance also the mutual orientation is important. The calculations here have been done with the program Mead [75] for BChl*a* with the TrEsp charges from Madjet *et al.* [49], rescaled to the dipole moment 37.1 D^2 of Knox & Spring [18]. All calculations are done in

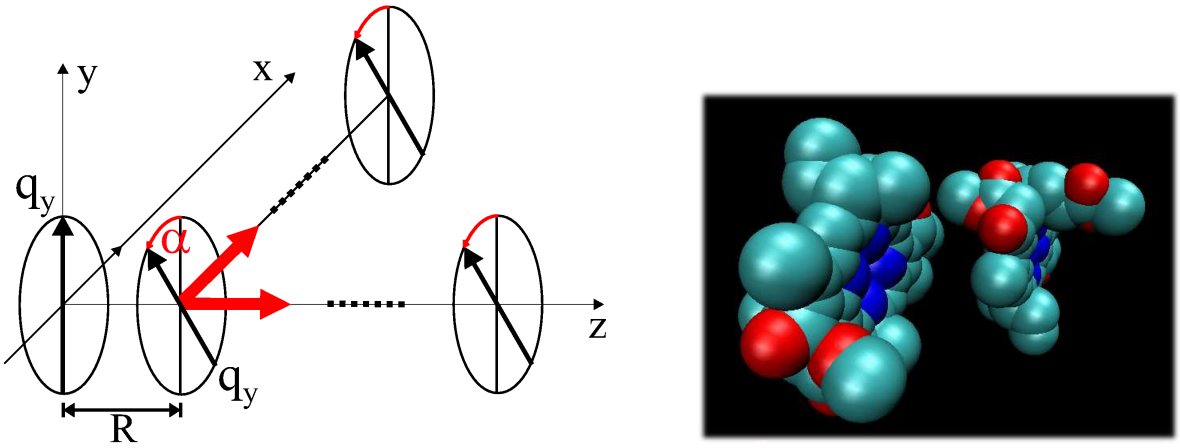

Figure 3.9: *(Left)* Calculations are either done for fixed distance in z-direction (R), different angles α and different distances in x-direction or different angles α and different distances in z-direction. *(Right)* VMD [74] picture (perspective) of two pigments with $z = 6$ Å, $x = 14$ Å and $\alpha = 0°$. The colored areas have $\varepsilon = 1$ and the black area $\varepsilon = 2$ for medium calculations.

vacuum ($\varepsilon = 1$) and dielectric medium with $\varepsilon = 2$, to extract the influence of the medium by comparison. The vacuum couplings from Mead were reproduced with a simple Fortran program, that calculates the vacuum couplings in point dipole approximation (Eq 3.18) and in extended dipole approximation (Eq 3.19), using the dipole extend of $d_0 = 8.8$ Å from Madjet *et al.* [49]. From Fig 3.10 it is evident that the vacuum couplings are reproduced in good approximation by the extended dipole couplings, while the point dipole approximation is not sufficient.

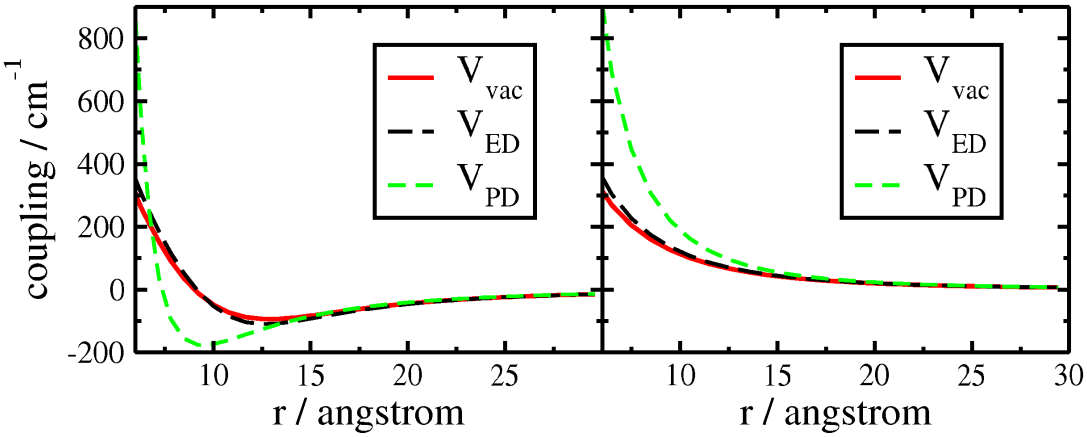

Figure 3.10: Excitonic couplings in vacuum (red), extended dipole approximation (black) with extension $d_0 = 8.8$ Å and point dipole approximation (green), plotted versus the center-to-center distance r. *(Left)* Move in x-direction and $z = 3$ Å , $\alpha = 0°$. *(Right)* Move in z-direction and $x = 0$ Å , $\alpha = 0°$.

Interestingly, it is possible to reproduce the difference between the vacuum couplings and the couplings in the dielectric (Fig 3.11, *left*) by the couplings of an extended dipole of an enlarged length $d_1 = 10$ Å, multiplied by a factor (Fig 3.11, *right*) $\Delta V \approx f \cdot V_{\text{vac}}^{(\text{ED})}(d_1 = 10 \text{ Å})$. As one can see in Fig 3.11, the minimum position of ΔV is a critical measure of the extend of the dipole to be used. The $\Delta V_{\text{vac}}^{(\text{ED})}$ for 10 and 11 Å describe the function ΔV with nearly the same quality, but the 10 Å curve describes the couplings for small distances a little bit better.

To investigate the angle dependence of ΔV, the couplings have been calculated for fixed z-distance ($R = 3$ Å) at several different angles ($\alpha = 0°$, $10°$, $20°$, $30°$, $45°$, $60°$, $75°$, $135°$) for distances varied in x-direction as shown in Fig 3.9 (*left*). The resulting couplings are presented in Fig 3.17. The angle

90° is skipped, because the coupling nearly vanishes at this angle (Eq 3.18, 3.19) and therefore numeric artefacts would be enhanced. To identify the angle dependence of the factor f that yields

$$\Delta V = V_{\text{vac}} - V_{\text{med}} \approx f(\alpha) \cdot V_{\text{vac}}^{\text{ED}}(d_1)\,, \tag{3.30}$$

the difference of the couplings in Fig 3.17 are calculated and the extended dipole couplings for $d_1 = 10$ Å are fitted to them (Fig 3.12), yielding different factors $f(\alpha)$ for the respective angles α.

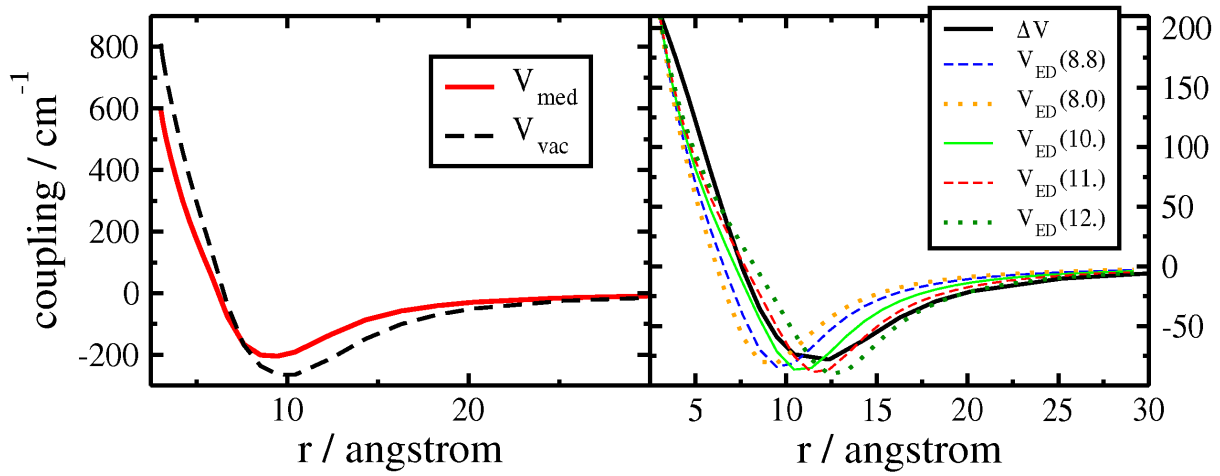

Figure 3.11: *(Left)* Excitonic couplings in medium (red) and vacuum (black), calculated with *Mead*. *(Right)* Difference of vacuum and medium couplings $\Delta V = V_{\text{vac}} - V_{\text{med}}$, in comparison with extended dipole couplings with different dipole extensions. For better comparison, the ED couplings are scaled with individual factors.

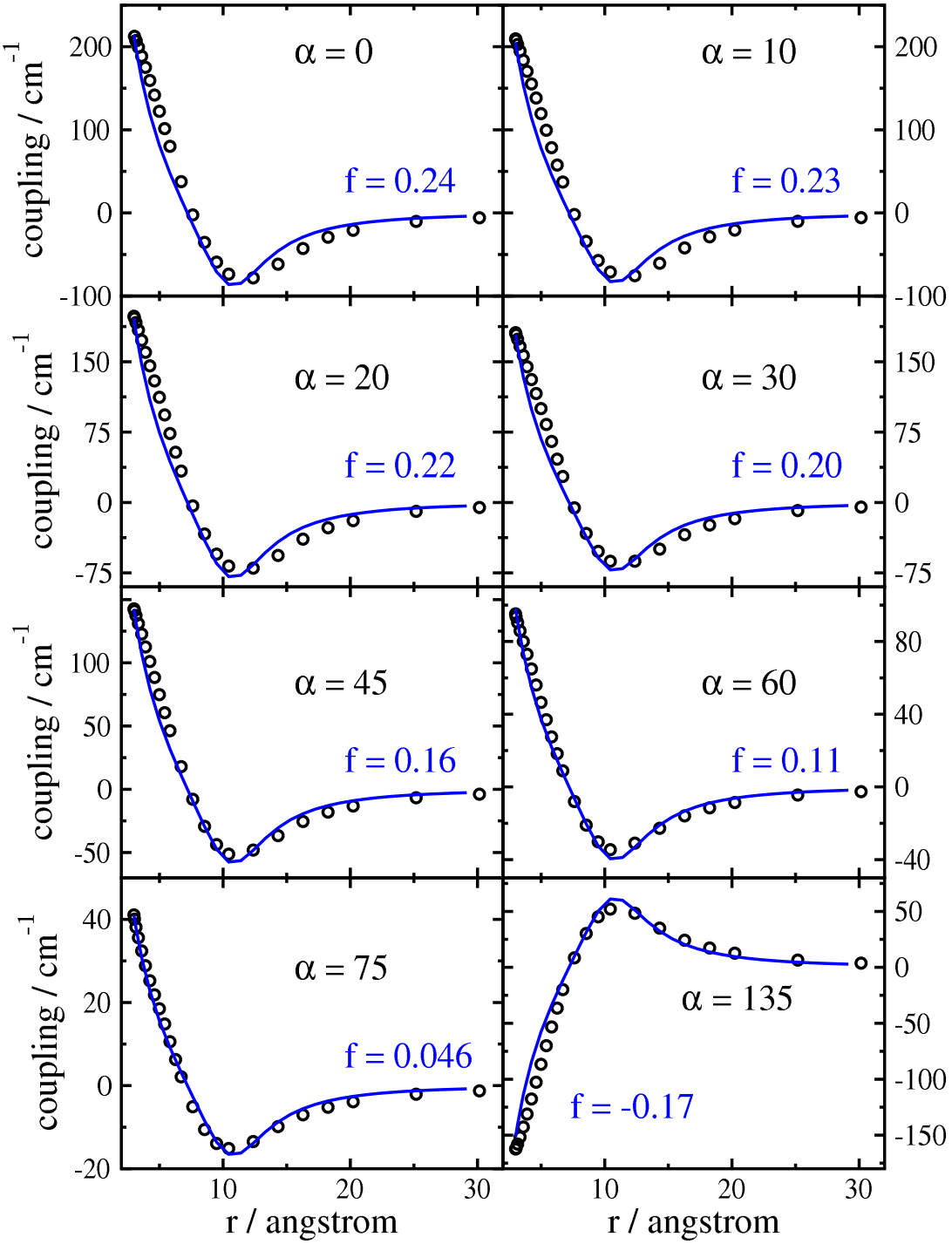

Figure 3.12: Black circles: difference between vacuum couplings and couplings in dielectric with $\varepsilon = 2$ (from Fig 3.17), i.e., $\Delta V = V_{\text{vac}} - V_{\text{med}}$, calculated for plan parallel bacteriochlorophylls with start distance $R = 3$ Å at certain angles α between both Q_y transition dipole moments, plotted versus center-to-center distance r (see Fig 3.9). Blue line: scaled coupling (scaling factor f given in the figure) of two extended dipoles $V_{\text{vac}}^{\text{ED}}(d_1)$, following Eq 3.19, with extensions 10 Å and dipole strengths 37.1 D^2.

In Fig 3.13 the fit factors of Fig 3.12 are shown for angles between $0°$ and $135°$ ($R = 3$ Å). Obviously these factors are well fitted by a scaled cosine function.

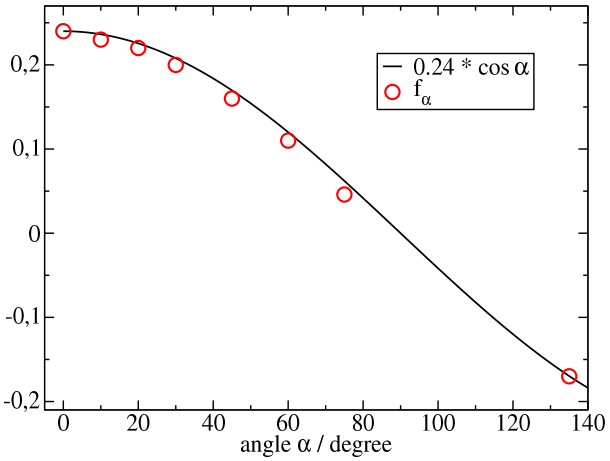

Figure 3.13: Scaling factors $f(\alpha)$ (Eq 3.30) obtained from Fig 3.12, in dependence of the angle α for fixed z-distance $R = 3$ Å (red circles), in comparison with a scaled cosine (black line).

To investigate the distance dependence, the couplings have been calculated for three different angles ($\alpha = 0°, 20°, 45°$) and distances between 0 and 30 Å in z-direction. The results are shown in Fig 3.16. It is evident that f is also distance dependent, i.e., in the simplest case it should hold $f = f_{R,r}(R,r) \cdot f_\alpha(\alpha)$. The function which is suitable to describe the data points is of the type $f(R,r) \propto 1 - e^{-a_1 \cdot R - a_2 \cdot r}$, where R is the distance between the planes, described by the Nitrogen atoms $N_A - N_D$ in the BChls and r is the center-to-center distance.

The coefficients have been determined by a manual fit using the program *gnuplot* [76].

Now it is possible to present a formula for the coordinate based calculation of the couplings in media without an explicit numerical solution of the Poisson-Boltzmann Equation:

$$V_{\text{med}}^{(\text{appr})} = V_{\text{vac}} - f \cdot V_{\text{vac}}^{\text{ED}}(d_1)\,, \tag{3.31}$$

where f is angle and distance dependent:

$$f = f(\alpha, R, r) = a_0 \cdot \cos\alpha \cdot (1 - e^{-a_1 \cdot R} \cdot e^{-a_2 \cdot r}) \tag{3.32}$$

with $a_0 = 0.42$, $a_1 = 0.28$, $a_2 = 0.04$ for BChl*a*. For other types of pigments (e.g. BChl*b* or Chl*a*) it is necessary to do the calculation again and extract specific coefficients a_0, a_1, a_2, because they might depend on the pigment type.

As a test of the empirical derived formulas Eq 3.31 and Eq 3.32, a calculation with a different fixed z-distance $R = 6$ Å and angle $\alpha = 0$ is done for center-to-center distances r between 6 and 25 Å. The result is shown in Fig 3.14.

In Fig 3.15 the ratio of V_{med} and V_{vac} for the Mead values is compared to the Scholes function (Eq 3.29) $s(r)$ and the ratio of our approximation (Eq 3.31, 3.32) to the vacuum couplings $V_{\text{med}}^{(\text{appr})}/V_{\text{vac}}$. The zero crossing of the ratio of calculated couplings (Fig 3.15, *left*) is well described by our approximation, as well as the limit for large distances fits very well with our approximation. The Scholes function $s(r)$ fits only better for a move in x-direction in the range of 8 to 13 Å, while it fails in the description of the overall behavior and gives wrong limits.

In Fig 3.16 *(left)* the approximated medium couplings using our approximation (red) and the Scholes approximation (orange) is compared to the exact medium couplings obtained by solving the Poisson equation numerically. Our approximation fits very well to the exact values, while the Scholes values fit well for distances larger than 10 Å. In Fig 3.17 also our approximation (red) fits very well to the medium

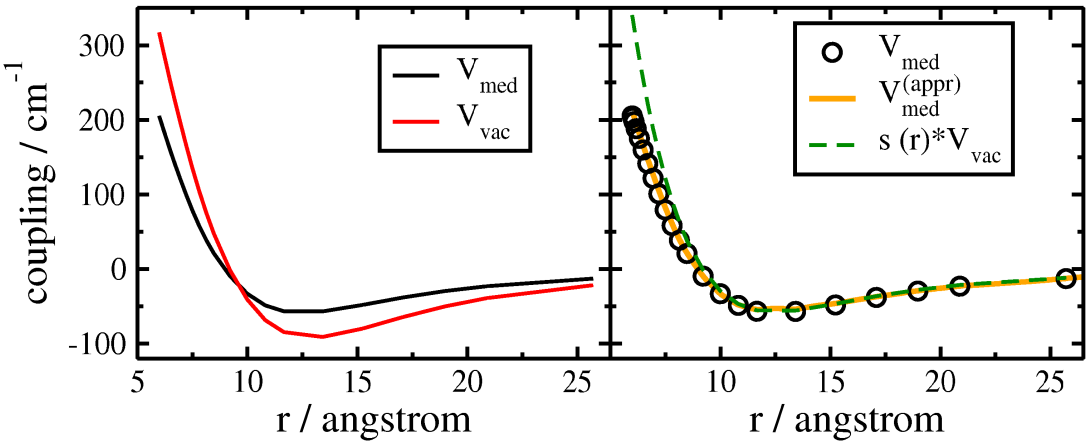

Figure 3.14: *(Left)* Vacuum couplings V_{vac} (red) and couplings in dielectric medium with $\varepsilon = 2$, V_{med} (black). *(Right)* Couplings in medium (black circles), $V_{\text{med}}^{(\text{appr})}$ following Eq 3.31, 3.32 for an angle $\alpha = 0°$ and plane distance $R = 6$ Å (orange) in comparison with the Scholes-approximation (Eq 3.29) $s(r) \cdot V_{\text{vac}}$ (green).

values, while the Scholes values (orange) fit very well for distances larger than 7 Å. In the range of 10 to 13 Å the Scholes values even fit slightly better.

As a result of the good agreement between the extended dipole approximation with the exact vacuum couplings (Fig 3.10) we can give an even simpler expression for Eq 3.31. Here only the coordinates of the Nitrogen atoms are needed.

$$V_{\text{med}}^{(\text{appr})} = V_{\text{vac}}^{\text{ED}}(d_0) - f \cdot V_{\text{vac}}^{\text{ED}}(d_1)\,, \tag{3.33}$$

with $d_0 = 8.8$ Å, $d_0 = 10$ Å and f specified in Eq 3.32.

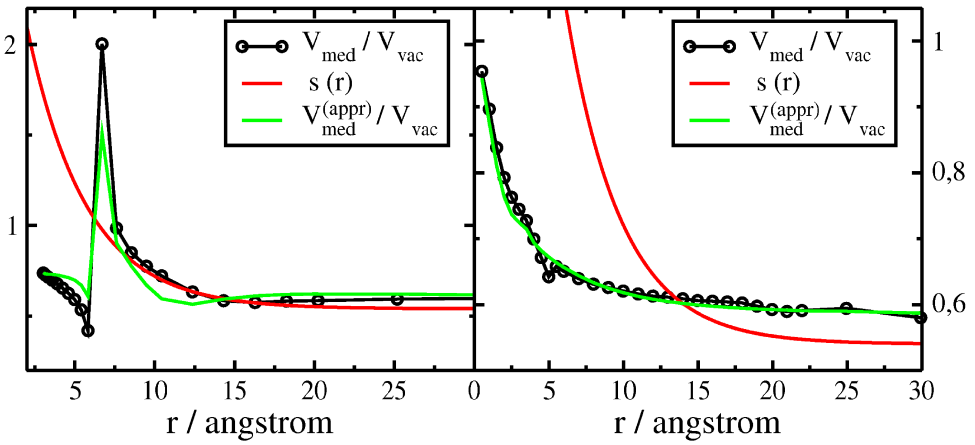

Figure 3.15: *(Left)* Move in x-direction with $R = 3$ Å and $\alpha = 0$. *(Right)* move in z-direction, $\alpha = 0$. $s(r)$ from Eq 3.29, in comparison with $V_{\text{med}}/V_{\text{vac}}$ from the mead calculations (Figs 3.17 and 3.16).

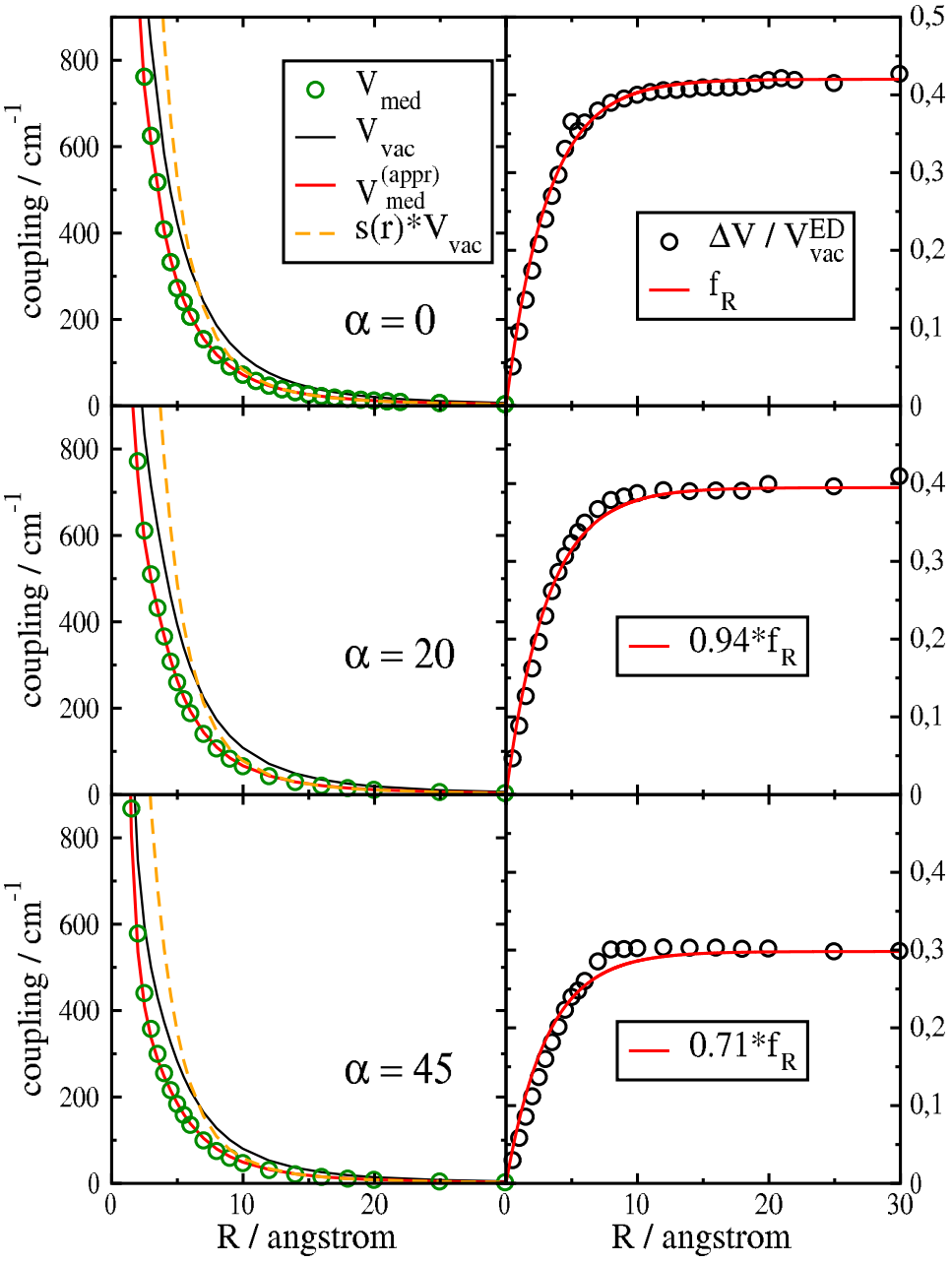

Figure 3.16: *(Left)* Couplings in dielectric with $\varepsilon = 2$, (V_{med}, green circles) and vacuum couplings (V_{vac}, black line) calculated with Mead in comparison with the approximation $V_{\text{med}}^{(\text{appr})}$ following Eq 3.31 and 3.32 (red) and the Scholes values (Eq 3.29) $s(r) \cdot V_{\text{vac}}$ (orange) for a move in z-direction and different angles α between the transition dipoles Q_y. *(Right)* Ratio of coupling difference $\Delta V = V_{\text{vac}} - V_{\text{med}}$ and $V_{\text{vac}}^{\text{ED}}(d_1)$ (black circles) and $f_R\,(R) \cdot \cos(\alpha)$ (red line).

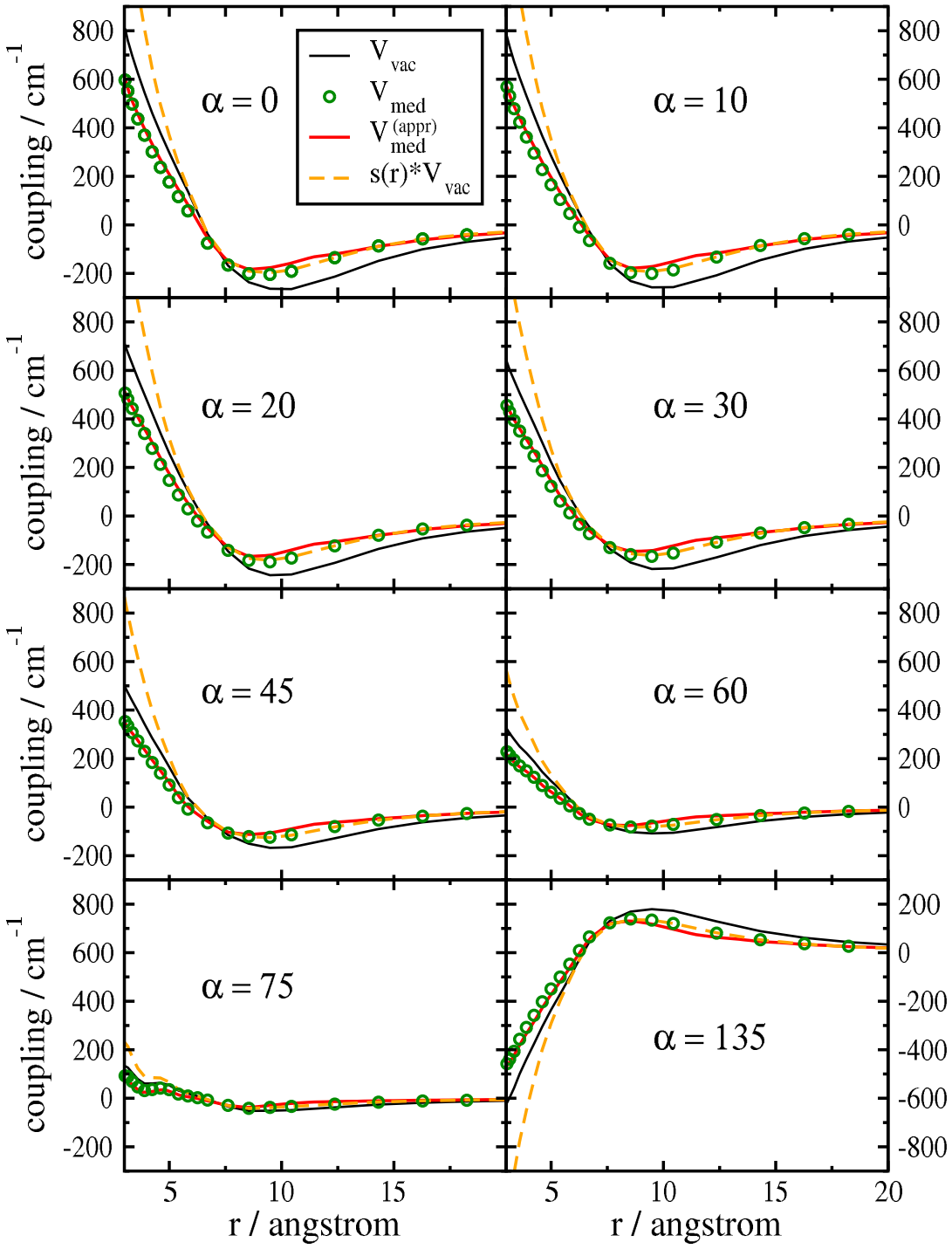

Figure 3.17: Move in x-direction. Vacuum couplings (black) and couplings in dielectric with $\varepsilon = 2$ (green circles), calculated for plan parallel BChls with distance $R = 3$ Å at certain angles between the transition dipole moments Q_y (see Fig 3.9). Calculations are done with the program Mead [75]. $V_{\text{med}}^{\text{appr}}$ calculated following Eqs 3.31 and 3.32, $s(r) \cdot V_{\text{vac}}$ calculated following Eq 3.29.

3.3 Calculation of Site Energies

In the following, four independent methods to obtain the local transition energies (site energies) of the seven BChl*a* molecules of the monomeric subunits of the FMO protein of *P. aestuarii* and *C. tepidum* are described. First the site energies are used as parameters that are optimized by a genetic algorithm in the fit of optical spectra. Afterwards, three methods which calculate the site energies directly at different levels of approximation, are presented.

3.3.1 Site Energies from Fit of Optical Spectra

Evolutionary Algorithm

An evolutionary algorithm is an optimization method, which takes the biological evolution as a paradigm. The evolution has the ability to adapt complex life-forms and organisms to their environmental and life conditions by manipulating their genetic constitution. Thereby a very difficult optimization problem is solved. The most amazing property of evolution is the relatively simple procedure and the cooperation of different control mechanisms. In a simple model the search procedure can be reduced to three simple principles: Mutation, selection and recombination.

Description of the Algorithm

An often successful way to treat nonlinear multidimensional optimization problems is to use an evolutionary algorithm as a fit routine [77–79]. An overview of the optimization process is given in Fig 3.18. In the initial step N sets of site energies are generated (a so-called *population* of N *chromosomes*), one

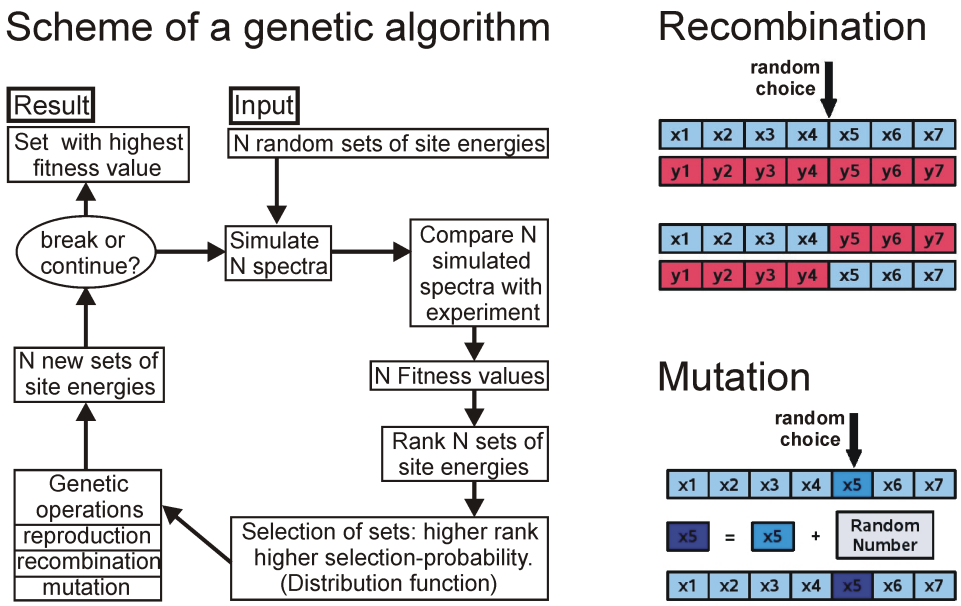

Figure 3.18: *Left* Working scheme of the genetic algorithm used in the fit of optical spectra to obtain the site energies. *Right* Genetic operations, recombination (*top*) and mutation (*bottom*).

set is provided (start set) and $N-1$ are randomly created. The corresponding spectra are calculated, and the different sets are ranked according to their *fitness value*, which is obtained from the reciprocal of the mean square deviation between the calculated and experimental spectrum. To get better individuals from generation to generation it is necessary to use a suitable distribution function which takes into account the ranking of chromosomes by choosing higher ranked chromosomes with higher probability than those with lower rank: the so–called *selection* of chromosomes. With these selected chromosomes genetic

Table 3.2: Test of the genetic algorithm, using the FMO coordinates. All site energies are expressed in units of cm^{-1}. The *True* values are site energies that were used to calculate a spectrum that is used instead of the experimental spectrum in the fit. The *Initial* values are different sets of initial site energies used in the fit, as explained in the text, and the *Fit-Result* values are the respective optimal site energies obtained from the genetic algorithm.

	Initial		Fit-Result		
BChl	Center	Swap	Center	Swap	True
1	12460	12450	12451	12442	12450
2	12460	12470	12521	12514	12520
3	12460	12550	12210	12207	12210
4	12460	12540	12320	12317	12320
5	12460	12210	12548	12558	12550
6	12460	12320	12542	12538	12540
7	12460	12520	12471	12469	12470

operations [77–79] (*reproduction, recombination* and *mutation*) are performed.
Reproduction: To avoid the loss of important information, in each step the chromosome with the highest rank is copied to the next cycle.
Recombination: Two sets of parameters are selected and it is decided by a random number after which position a *cross-over* (see figure 3.18) is done to produce a new parameter set.
Mutation: One or two elements of a chromosome are selected by random and their values are changed by adding a random number (reasonable boundaries!). Mutation can be done after selection of one set of parameters or additional after recombination. The fit is iteratively completed. In this work 100 to 200 fit cycles were computed, with a population of 100 chromosomes.

Test of the Algorithm for FMO

The algorithm was tested (using the FMO coordinates) first by replacing the experimental spectrum by a calculated spectrum, shown as circles in Fig 3.19, that was obtained for the site energies given in the last column (*True*) of Table 3.2. A simultaneous fit of the absorption (OD), linear dichroism (LD), circular dichroism (CD) and the derivative of the absorption (OD′) spectrum was performed. A typical population of 100 chromosomes was used. After 200 iteration steps, the values for the site energies found by the algorithm were within ± 2 cm^{-1} of the true values for convenient initial values and within ± 9 cm^{-1} for inconvenient initial values. The algorithm converges fast, if all initial values for the site energies are chosen equal at an energy of 12460 cm^{-1} in the center of the target spectrum. The spectrum resulting for those initial site energies is shown as dotted line in Fig 3.19. The most difficult situation occurred with an inverted order of the initial values with respect to the optimal values, the respective initial spectrum is shown as a dashed line in Fig 3.19. If only the OD spectrum alone was fitted, the optimal site energies obtained were wrong, even if a population of 500 chromosomes was used.

Test of the Algorithm for PS1

Again the experimental spectra are replaced by simulated spectra, here triplet minus singlet (T – S) and cation minus neutral ($P^+ - P$) spectra and the derivatives of both. For the algorithm test the triplet state is placed on P_A and the charge on P_B . For each inhomogeneous spectrum N = 2000 homogenous spectra are averaged. The special pair coupling is set to 180 cm^{-1}, what is relatively close to the expected special pair coupling. In contrast to the FMO fit, also the inhomogeneous line-widths (fwhm) are treated as fit parameters. A simultaneous fit of the T – S and $P^+ - P$ spectra and their derivatives was performed. A typical population of 200 chromosomes was used. After 200 iteration steps, the values for the site energies found by the algorithm were within ± 10 cm^{-1} of the true values and the values for the inho-

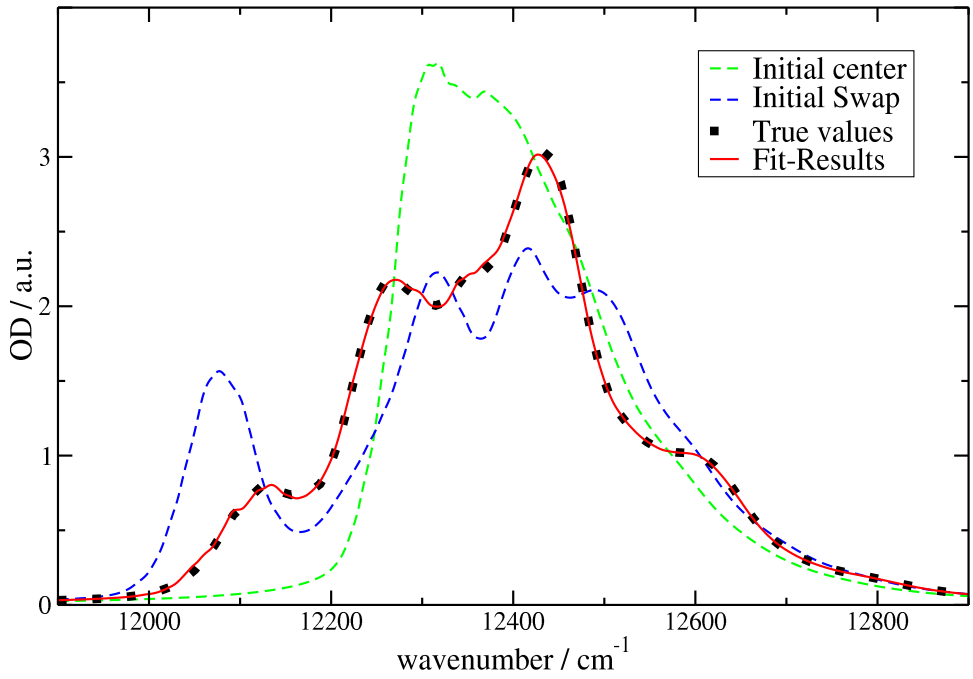

Figure 3.19: Test of the genetic algorithm, using the FMO coordinates. The two *Initial* spectra are obtained for different initial sets of site energies used in the genetic algorithm as explained in the text. The *True* spectrum is used in place of the experimental spectrum, it is obtained for a set of known test values of site energies. The *Fit-Results* (solid line) shows the spectra obtained for the two sets of optimal site energies given in Table 3.2.

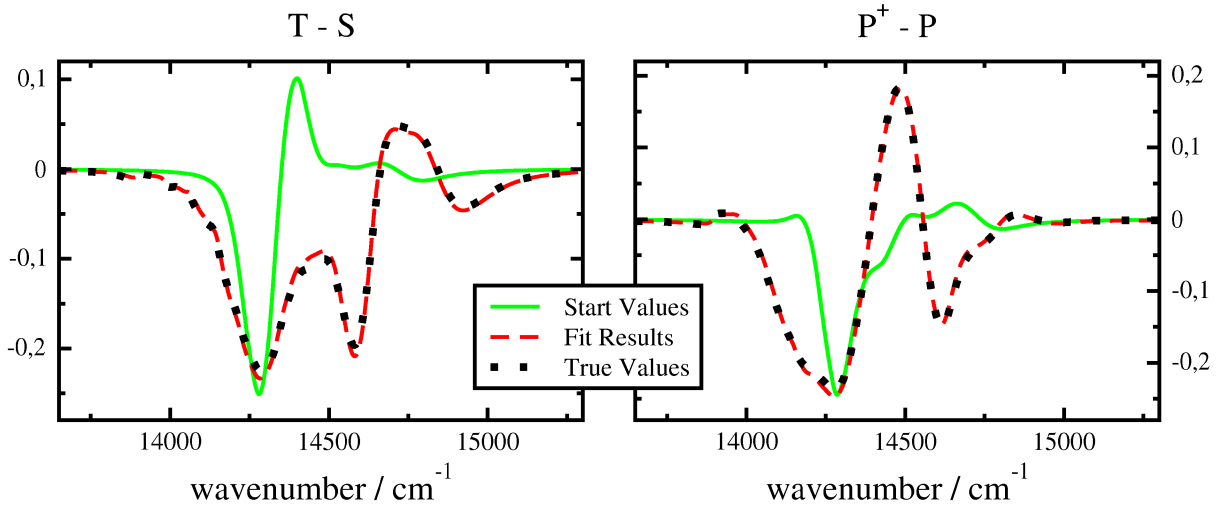

Figure 3.20: Test of the genetic algorithm, using the PSI coordinates. The initial spectrum for T – S is scaled by factor 0.4, because of better visualization. The *Initial* (green line) spectra are obtained for the initial set of site energies used in the genetic algorithm as explained in the text. The *True Value* spectrum (black dots) is used in place of the experimental spectrum, it is obtained for a set of known test values of site energies. The *Fit-Results* (red dashed line) shows the spectra obtained for the two sets of optimal site energies given in Table.

Table 3.3: Test of the genetic algorithm, using the PSI coordinates. Site energies (E_m) and inhomogeneous line-widths (fwhm) are expressed in units of cm^{-1}. The *True* values are site energies that were used to calculate a spectrum that is used instead of the experimental spectrum in the fit. The *Initial* values is the set of initial site energies used in the fit, as explained in the text, and the *Fit-Result* values are the respective optimal site energies obtained from the genetic algorithm.

	Initial		Fit		True	
Chl	E_m	fwhm	E_m	fwhm	E_m	fwhm
1011 (P_A)	14550	150	14689	258	14680	250
1021 (P_B)	14550	150	14496	257	14500	290
1012	14550	150	14764	157	14770	160
1022	14550	150	14438	197	14440	190
1013	14550	150	14732	119	14730	140
1023	14550	150	14180	175	14170	180

mogeneous line-widths are within ± 20 cm^{-1}, except for P_B, where the deviation is around 30 cm^{-1} for the given initial values. The algorithm converges fast, if all initial values for the site energies are chosen equal at an energy of 14550 cm^{-1} in the center of the target spectrum. The spectrum resulting for the initial site energies is shown as thin green line, the Test spectrum for the True Values is the black dotted line and the spectrum resulting for the fitted values is the red dashed curve in Fig 3.20.

3.3.2 Site Energies from Structural Data

In the following, three methods are described that aim at a direct calculation of site energies from the structural data. In these approaches no absolute site energies but relative site energy shifts are calculated. The site energy E_m for pigment m is given by:

$$E_m = E_0 + \Delta E_m \,, \tag{3.34}$$

where the site energy shift ΔE_m is obtained by the methods described below, and the constant E_0 is assumed to be equal for all pigments and will be determined from the overall spectral position in comparison with experiment.

Point Charge – Dipole Method

From classical theory the interaction between a dipole $\vec{\mu}$ and an electric field $\vec{E}$ (in vacuum) is given as $W = -\vec{\mu} \cdot \vec{E}$. The ground and excited states of the pigments are described by their dipole moments $\vec{\mu}_{\rm gr}$ and $\vec{\mu}_{\rm ex}$, respectively, and the electrochromic shift of the transition energy is obtained as the difference in interaction energies of the excited and the ground state $\Delta E = W_{\rm ex} - W_{\rm gr}$. We note that an additional shift $-1/2\,\Delta\alpha\,E^2$ occurs because of the difference in polarizability $\Delta\alpha$ of the two electronic states [80, 81]. Including the $\Delta\alpha$ reported for BChl*a* from Stark experiments [82], spectral band shift measurements in solution [83] and quantum chemical calculations [80] has a small effect on the calculated electrochromic shifts. The site energies obtained, including the $\Delta\alpha$-term are within 10% of those obtained by neglecting this term. The large variance in the reported $\Delta\alpha$ values ranging from -4.3 Å^3 [80] to 16 Å^3 [83] makes it difficult to obtain a reliable estimate of the small correction term for the site energies. Therefore this second order correction is neglected in this study and only the first order term described above is taken into account.

The shift ΔE_m of the transition energy of the mth pigment in a field of N point charges q_k in a dielectric medium then follows as:

$$\Delta E_m = \frac{1}{\varepsilon_{\rm eff}} \sum_{k=1}^{N} q_k \cdot \frac{\Delta\vec{\mu}_m \cdot \vec{r}_{mk}}{r_{mk}^3} \tag{3.35}$$

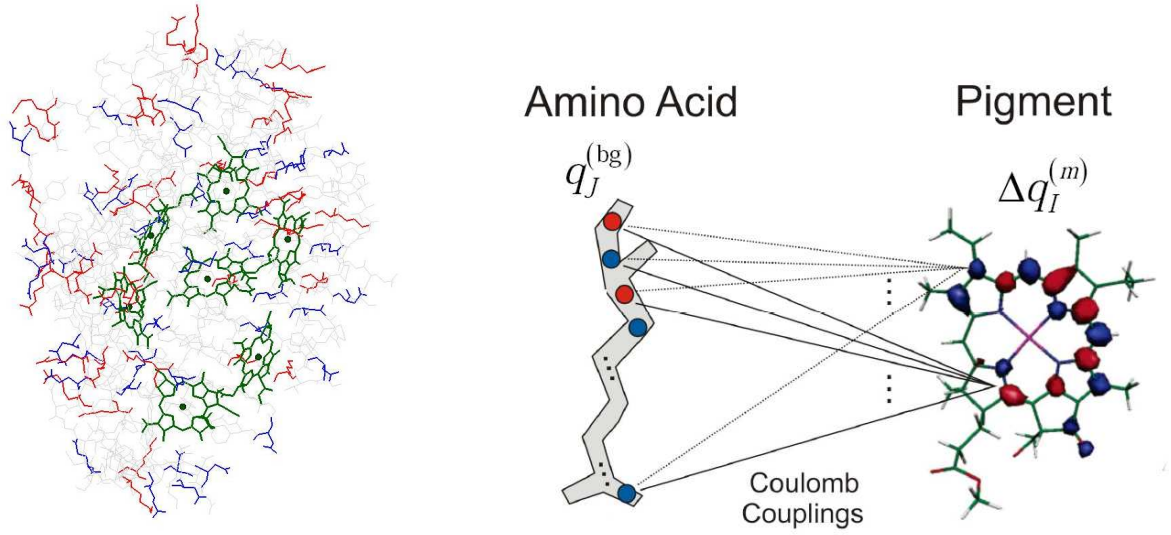

Figure 3.21: *Left:* Structure of monomeric subunit of the FMO complex of *C. tepidum* as used in PCD method: BChls green, positively charged amino acids (Arg, Lys) red, negatively charged amino acids (Asp, Glu) blue, neutral amino acids grey. *Right:* Calculation of site energy shifts as in CDC method: all atomic partial charges of the environment (charged and neutral) as well as the difference in charge density between excited and ground state of the pigments (negative charge density red, positive blue) are considered.

where $\Delta\vec{\mu}_m = \vec{\mu}_m^{\mathrm{ex}} - \vec{\mu}_m^{\mathrm{gr}}$ is the difference of the permanent dipole moments of ground- and excited state of the mth pigment and $\vec{r}_{mk} = \vec{r}_m - \vec{r}_k$ is the vector connecting the center of the mth pigment with the kth point charge. The effective dielectric constant $\varepsilon_{\mathrm{eff}}$ in the denominator of Eq 3.35 is used to describe the screening and local field effects by the dielectric environment [84] in an effective way. This method has been successfully applied to calculate electrochromic shifts of pigment transition energies due to oxidized and reduced pigments in bacterial reaction centers [84] and photosystem II reaction centers [32]. Here, the method is applied to calculate site energy shifts due to charged amino acids.

The experiments were performed at pH 8 [42, 43]. For simplicity, we assume that this pH value also applies to the environment of all the titratable groups in the protein and hence arginine (Arg) and lysine (Lys) are negatively charged, whereas aspartic acid (Asp) and glutamic acid (Glu) carry a positive elementary charge (Fig 3.21). The charges were located at the center of charge of the amino acid, obtained from the atomic partial charges of the CHARMM22 [65] force field.

The difference vector of excited and ground state permanent dipole moments $\Delta\vec{\mu}_m$ is assumed to be of equal magnitude and orientation with respect to the BChl*a* macrocycle for all pigments. From Stark spectra of BChl*a* [85] a value for $|\Delta\vec{\mu}|$ between 1.6 D and 2.4 D and an orientation of $\Delta\vec{\mu}$ approximately along the $\mathrm{N_B} \rightarrow \mathrm{N_D}$ axis of the BChl can be estimated [85] [5]. In the present calculations we use $|\Delta\vec{\mu}| = 2.0$ D and determine $\varepsilon_{\mathrm{eff}}$ from the fit of the overall width of the spectrum obtained for the calculated site energies. In the following we refer to this method as the the PCD method.

Poisson – Boltzmann Quantum Chemical Method

In the Poisson-Boltzmann quantum chemical (PBQC) approach, quantum chemistry of BChl*a* in vacuum is combined with electrostatics of the whole protein in atomic detail including polarization effects of the solvent and the protein and an average over the protonation states of the titratable residues [26]. In short, atomic partial charges of the BChls are obtained by a fit of the electrostatic potential of the ground and excited state charge densities [49]. The site energy differences ΔE_m are then obtained by calculating the

[5] For BChl*a* in polystyrene ($\varepsilon = 2.6$) a value $|\Delta\vec{\mu}|/f$ of 2-3 was reported [85]. Using the empty cavity factor $f = 3\varepsilon/(2\varepsilon+1)$ then results in $|\Delta\vec{\mu}| = 1.6 - 2.4$.

electrostatic free energy change that occurs when moving the two sets of partial charges from the solvent (with dielectric constant $\varepsilon_{\rm solv}$) into the specific binding site of BChl m in the protein. Further details are given in [26].

Charge Density Coupling Method

In the charge density coupling (CDC) method, the PBQC approach described above is simplified by (i) assuming a standard protonation pattern and (ii) describing the polarization effects by screening the charge density coupling by an effective dielectric constant $\varepsilon_{\rm eff}$. To evaluate the charge density coupling, two sets of partial charges are needed, $\{\Delta q_I^{(m)}\}$ and $\{q_J^{(\rm bg)}\}$. The $\Delta q_I^{(m)} = q_I^{(m)}(1,1) - q_I^{(m)}(0,0)$ describe the shift in charge density of the PPC when BChl m is excited. It is non-zero only on the macrocycle of BChl m. The remaining charge density of the PPC is described by the background charges $q_J^{(\rm bg)}$ that include the whole protein, certain water molecules [6], all BChls $n \neq m$ in the ground state and also the phytyl chain of BChl m.

The electrochromic shift of the mth pigment is calculated from the Coulomb interaction of the difference of ground and excited state partial charges $\Delta q_I^{(m)}$ of pigment m with the background charges $q_J^{(\rm bg)}$

$$\Delta E_m = \frac{1}{\varepsilon_{\rm eff}} \sum_{I=1}^{N} \sum_{J=1}^{K} \frac{\Delta q_I^{(m)} \cdot q_J^{(\rm bg)}}{|r_I^{(m)} - r_J^{(\rm bg)}|} \,, \tag{3.36}$$

where N is the number of partial charges of the macrocycle of BChl m, K is the total number of background partial charges and $|r_I^{(m)} - r_J^{(\rm bg)}|$ is the distance between the Ith difference partial charge of the mth pigment and the Jth partial charge of the background.

The background charges of the protein and the water are taken from the CHARMM22 force field [65]. The partial charges of BChls are obtained from a fit of the *ab initio* electrostatic potential of the ground and excited state charge densities as described in detail in [49]. The quantum chemical calculations are either performed on a fully geometry optimized BChl*a* resulting in the same partial charges for all BChls, or after performing a restricted geometry optimization where the torsional angle of the acetyl groups of BChls is kept as in the crystal structure [23]. In the latter case, we also included the direct effect of the acetyl group rotation on the transition energy as obtained from the quantum chemical calculations. The site energy is then obtained as $E_m = E_0 + \Delta E_m + \Delta E_m^{(\rm qc)}$ with ΔE_m in Eq 3.36 and adjusting E_0 to describe the spectra. We note that $\Delta E_m^{(\rm qc)}$ is also considered in the PBQC method.

[6] These water molecules are the hydrogen bond donor to the 3-acetyl group of BChl 1, the axial ligand to the Mg atom of BChl 2, and two water molecules bridging the side chains of Asp 234 and Ser 235 via H-bonds.

Chapter 4

Application to FMO

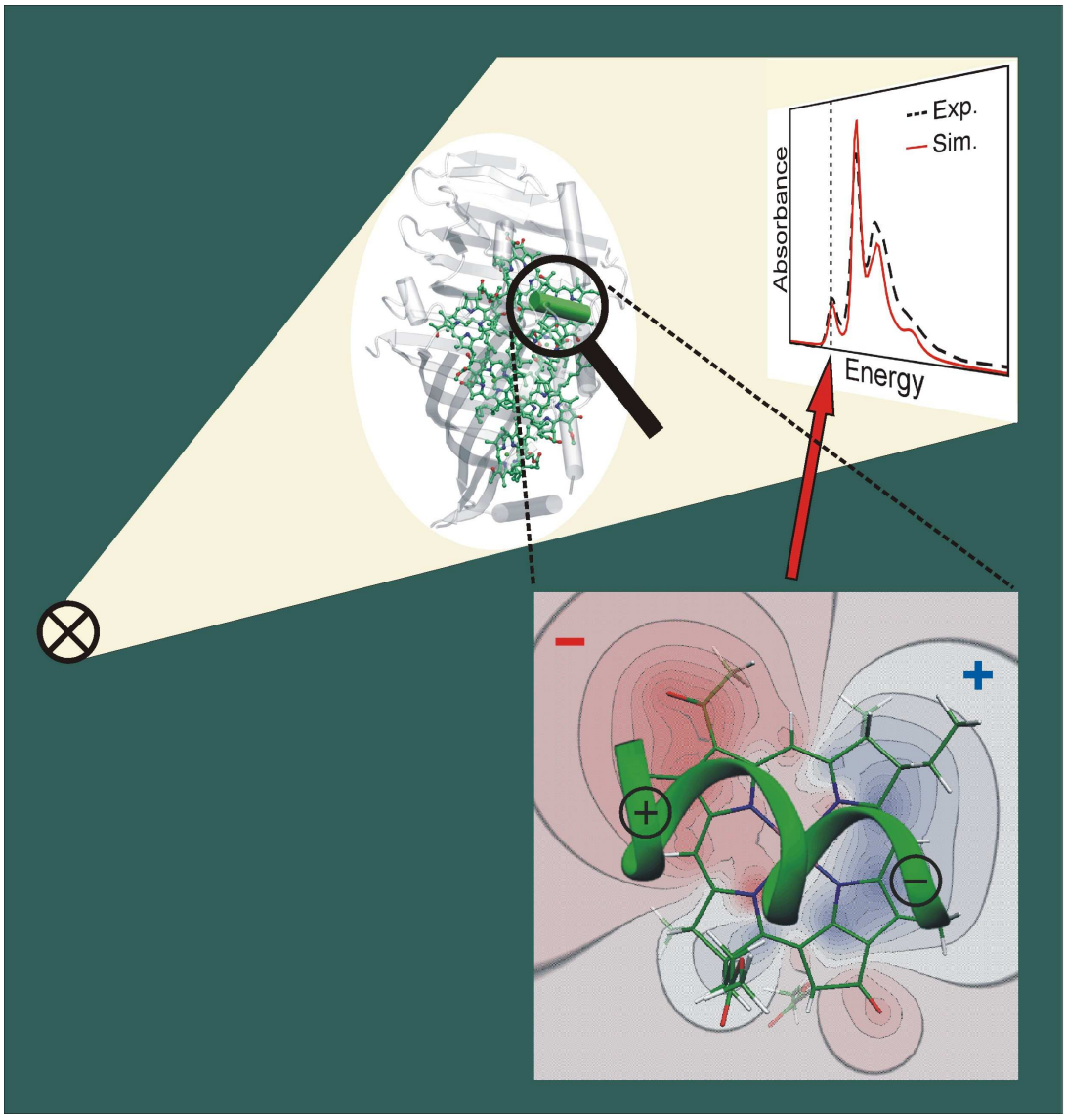

Figure 4.1: The absorbance of light of a photosynthetic pigment-protein complex (FMO protein of *P. aestuarii*) is explained by structure-based simulations. The dipole moment of an α-helix determines the energy sink at a particular pigment in this system by electrostatic interactions as illustrated in the lower part.

Since the first high resolution crystal structure of the FMO protein appeared more than 30 years ago [2], there have been numerous of theoretical approaches trying to explain the low-temperature optical spectra.

In these approaches, the structural data have been used to calculate excitonic couplings between the seven BChl*a* pigments that are bound per FMO monomer and the site energies were treated as fit parameters. Nevertheless, it has been an unsolved problem for more than 20 years to find a satisfying description of the different linear optical spectra and a common set of site energies.

A large part of the puzzle was solved by Aartsma and coworkers [42, 86] who used a smaller effective dipole strengths of the BChls in the calculation of excitonic couplings than assumed previously. The smaller excitonic couplings allowed for a simultaneous description of absorption and linear and circular dichroism. We have recently checked [53] that the values for the optimal site energies do not change qualitatively, if a more sophisticated theory of optical spectra [30] is used that contains vibrational sidebands, life-time broadening and resonance energy transfer narrowing, which were neglected in the original approach [86].

In addition, we presented [53] a quantitative explanation of the low effective dipole strength. In this approach, a Poisson equation is solved for the electrostatic potential of transition charges originating from the transition monopole approximation of the $S_0 \rightarrow S_1$ transition of BChl*a* [58]. The monopoles are positioned in vacuum cavities in the dielectric volume of the protein, where the cavity shapes are determined by van-der-Waals radii of the atoms of the BChl cofactors and the protein volume by the radii of protein atoms.

Recently, a new method (TrEsp) has been developed by Madjet *et al.* [49] to obtain transition charges from a fit of the electrostatic potential of the *ab initio* transition density. The coupling from these transition charges was shown to be identical with the one that is obtained in the transition density cube method [61]. Here, we will use the TrEsp transition charges and simplify the description of the dielectric environment by including the solvent and assigning the same dielectric constant to the protein and the solvent.

The drawback of a fitting procedure for the site energies is that it is impossible to relate the obtained optimal values to structural details of the pigment-protein complex. A first attempt of a direct calculation of site energies from structural data was reported by Gudowska-Nowak *et al.* [87]. Quantum chemical calculations of BChl transition energies were performed taking into account the different conformations of the macrocycles of the BChls, including the acetyl group rotation and also all charged amino acids in the vicinity of the BChls. However, the reported site energies do not describe the optical spectra, most likely because important long-range electrostatic interactions were neglected in this purely quantum chemical approach.

We have recently used a very simple electrostatic method [53] to include all charged amino acids of the protein, assuming a standard protonation pattern. The site energy shifts were obtained from the difference in Coulomb couplings between the charge densities of the charged amino acid residues and the ground and excited state charge densities of the BChls. The former were described by point charges and the latter by the difference permanent dipole moment between ground and excited state. We will therefore term this approach PCD (point charge-dipole) method. A qualitative description of experimental data was obtained, after performing a partial fit of the site energies of those two BChls that are not ligated by His but by Leu (BChl 5) and water (BChl 2). The major drawback of this approach is a too simple description of interactions between BChls and their close environment as is evident from the difference potential between the charge density of the excited and the ground state of BChl*a* [49] in Fig. 4.11. This potential is clearly different from that of a dipole, and therefore, e.g., hydrogen bond effects to the 13^1-keto and 3-acetyl group are incorrectly described in the PCD approach. The difference potential indicates how a partial charge of the protein varies the transition energy of the BChls. For example, if a positive charge is located in the negative difference potential (shown in red) a stronger stabilization of the excited state and therefore a red shift of the transition energy results.

To take into account both, the short- and the long-range interactions in an appropriate way, a new calculation method was proposed by Müh *et al.* [26], combining quantum chemistry with electrostatics

in atomic detail. The charge density of both the protein and the pigments was described by atomic partial charges. Moreover, polarization effects of the dielectric of the protein and the solvent were considered as well as a realistic protonation pattern by solving a Poisson-Boltzmann equation and using a Monte Carlo approach to sample the possible protonation states of the titratable residues. We will call this approach the PBQC (Poisson-Boltzmann Quantum Chemistry) method. For the first time, it became possible to reach quantitative agreement between experimental spectra and calculations that essentially contain no free parameters. On this basis, the importance of different parts of the protein could be analyzed. Rather unexpectedly, the electric field of the backbone of two α-helices was identified to determine the energy sink at BChl 3 [26]. Besides this effect, charged amino acids, hydrogen bonds between the keto and acetyl groups of BChls and their protein environment, and other charge density couplings contribute to the shifts. Polarization effects and the different conformations of the BChls were found to be least important.

The latter finding provided the inspiration to study whether it is possible to simplify the PBQC approach by just taking into account the Coulomb coupling between the charge densities of the ground- and excited states of the BChls and those of the protein. In this approach that we term CDC (charge density coupling) method, any polarization effects are approximated by screening the Coulomb coupling by an effective dielectric constant ε_{eff}. Furthermore, a standard protonation pattern is assumed for the titratable residues.

4.1 Couplings

Here the couplings calculated with the methods introduced in section 3.2 for the FMO complex of *C. tepidum* and *P. aestuarii* are presented.

4.1.1 Couplings Calculated with Point Dipoles and Transition Monopoles

The results for the couplings calculated in the transition monopole approximation and for $\varepsilon = 2$ (Table 4.1, column 3a and 3b) are compared to the values obtained for $\varepsilon = 1$ in the transition monopole (column 1a/b), and point dipole approximation from Eq 3.18, using $f = 1.0$ (column 2a/b) and $f = 0.8$ (column 4a/b). A least mean square fit, $V_{mn}^{\mathrm{TM}}(\varepsilon = 2) = f \cdot V_{mn}^{\mathrm{TM}}(\varepsilon = 1)$, for the transition monopole couplings in columns 1 and 3 results in $f = 0.80$. The closest agreement between $V_{mn}^{\mathrm{TM}}(\varepsilon = 2)$ and the point dipole approximation (column 2) were obtained by using a factor of $f = 0.81$ (*P. aestuarii*) and 0.82 (*C. tepidum*), i.e., we obtain nearly the same correction factor as for the difference between $V_{mn}^{\mathrm{TM}}(\varepsilon = 2)$ and $V_{mn}^{\mathrm{TM}}(\varepsilon = 1)$. It is clear, thereby that the point dipole approximation works well and that the main effect on the couplings is due to the dielectric environment. The present factor of $0.80 - 0.82$ is somewhat larger than the factor 0.72 obtained for point dipoles in a spherical cavity[1].

A closer examination, using extended dipoles instead of transition monopoles, shows that about half of the deviations occur because of the more realistic charge distribution and the remaining half due to the more realistic cavity shape and the fact that cavities of neighboring pigments overlap. However, overall the simple spherical empty cavity model is seen to work surprisingly well, being just off by about 10 %. In the calculation of optical spectra and exciton relaxation presented below we use the point dipole approximation and a factor $f = 0.8$ for both *P. aestuarii* and *C. tepidum*.

4.1.2 Couplings Calculated with TrEsp Charges

The excitonic couplings (only for *P. aestuarii*) were calculated in vacuum ($\varepsilon = 1$) and in a dielectric ($\varepsilon = 2$), representing the protein (prot) or the protein and the solvent (psol). TrEsp transition monopole charges were used obtained either for fully geometry optimized planar BChl*a* (plan) or taking into account the

[1] For $\varepsilon = 2$ inserted into the empty cavity factor that includes the dielectric shielding $\frac{1}{\varepsilon}$, i.e. $f(\varepsilon = 2) = \frac{9\varepsilon}{(2\varepsilon+1)^2} = 0.72$.

conformation of the acetyl group (conf). The results for these various calculations are presented in Table 4.2. As seen from a comparison of columns (1) - (4), there is only a minor influence of the acetyl group conformation on the couplings. The couplings obtained for the *prot* and the *psol* dielectric are also very similar. However, the comparison of these calculations with the vacuum calculations ($\varepsilon = 1$) in columns (5) and (6) shows that there is a reduction of the strongest couplings by about 20 % due to the dielectric medium. The excitonic couplings determined by the various TrEsp methods can be well approximated by the point dipole approximation and a factor $f = 0.8$ as seen in the last column of Table 4.2 and in Fig 4.2, where the optical spectra obtained with TrEsp/psol (conf) and PD ($f = 0.8$) are compared to experimental data [42]. In the TrEsp calculation, the change in transition dipole orientation ($\vec{\mu}_m$) was taken into account. We find, however, that all transition dipole moments $\vec{\mu}_m$ lie within $\pm 2^\circ$ of the $N_B - N_D$ axis of the respective BChl m. The site energies of the PBQC approach [26] were used in the calculation of the spectra.

4.1.3 Comparison of TM and TrEsp Couplings

If we compare the couplings calculated with TrEsp charges for planar BChls (prot) and $\varepsilon = 2$ (column 1, table 4.2) with the couplings calculated with TM charges of Chang [58] (Table 4.1, column 3b), which are also calculated for planar BChls in the same environment, we find that the couplings are very similar. The largest deviation of 14 cm^{-1} is found for the coupling between pigment 5 and 6, the other deviations are smaller than 9 cm^{-1}. The highest coupling ($1 - 2$) is exactly the same for both methods.

The couplings with TrEsp charges have been calculated only for *P. aestuarii*, but we can expect that also for *C. tepidum* the point dipole approximation and a factor $f = 0.8$ is a good approximation.

4.1.4 Discussion

The calculations with TrEsp charges (section 4.1.2) corroborate the conclusion from the former calculations of section 4.1.1 that the excitonic couplings in the FMO protein can be well described by the point-dipole approximation taking into account the influence of the dielectric by an effective dipole strength of $f d_{\text{vac}}^2 = 30\ \text{D}^2$. The semi-empirical transition monopole charges of Chang [58] used in section 4.1.1 were replaced by the *ab initio* TrEsp charges of Madjet *et al.* [49], taking into account the influence of the acetyl group rotation. In addition, the solvent was included by assigning to it the same ε as to the protein. All of these extensions do not change the effective dipole strength and therefore support our earlier explanation. If at all, there is a slight decrease of the factor f from 0.80 in the calculations of section 4.1.1 to $0.76 - 0.78$ in section 4.1.1. However, at the present level of theory, we consider such a small change as not significant. The assumption of the same factor f becomes incorrect for the small couplings obtained at large inter pigment distances [53]. The error made for these small couplings does not influence the spectra significantly because of the dominating influence of the nearest neighbor couplings.

Table 4.1: Excitonic couplings for *C. tepidum* and *P. aestuarii* in units of cm^{-1}. (1) Transition monopole approximation using transition charges of Chang [58], (2) point dipole approximation with $f = 1$ in Eq 3.18, (3) electrostatic calculation of transition monopole coupling in dielectric environment of the protein (with optical dielectric constant $\varepsilon = 2$) using the program Mead and the same transition charges as for the calculations in columns (1), (4) Point-dipole couplings, Eq 3.18, obtained for $f = 0.8$. The large couplings are highlighted.

	C. tepidum				*P. aestuarii*			
BChl	(1a) TM vac $\varepsilon = 1$	(2a) PD Eq 3.18 $f = 1$	(3a) TM prot $\varepsilon = 2$	(4a) PD Eq 3.18 $f = 0.8$	(1b) TM vac $\varepsilon = 1$	(2b) PD Eq 3.18 $f = 1$	(3b) TM prot $\varepsilon = 2$	(4b) PD Eq 3.18 $f = 0.8$
1-2	**-122**	**-110**	**-96**	**-88**	**-133**	**-123**	**-104**	**-98**
1-3	7	7	5	6	7	7	5	5
1-4	-8	-7	-4	-6	-8	-7	-4	-6
1-5	8	8	5	7	9	9	5	7
1-6	-17	-17	-13	-14	-20	-19	-15	-15
1-7	-10	-12	-6	-10	-11	-17	-8	-14
2-3	**39**	**39**	**33**	**31**	**38**	**38**	**33**	**31**
2-4	10	10	7	8	10	10	7	8
2-5	1	1	5	1	2	2	5	1
2-6	13	15	7	12	15	16	8	13
2-7	4	5	-0	4	6	11	1	9
3-4	**-73**	**-67**	**-51**	**-54**	**-69**	**-70**	**-47**	**-56**
3-5	-2	-3	1	-2	-2	-2	1	-2
3-6	-12	-12	-8	-10	-11	-12	-8	-10
3-7	7	8	8	6	4	4	5	3
4-5	**-95**	**-88**	**-77**	**-71**	**-88**	**-82**	**-71**	**-66**
4-6	-21	-21	-14	-17	-22	-23	-15	-18
4-7	**-82**	**-79**	**-67**	**-63**	**-76**	**-73**	**-62**	**-58**
5-6	**95**	**101**	**78**	**81**	**109**	**111**	**90**	**89**
5-7	-3	-2	-0	-1	-6	-4	-3	-3
6-7	**49**	**50**	**38**	**40**	**41**	**46**	**33**	**37**

Table 4.2: Excitonic couplings for *P. aestuarii* in units of cm^{-1} obtained with different methods explained in detail in the text. The large couplings are highlighted.

	P. aestuarii						
BChl	(1) TrEsp plan prot $\varepsilon = 2$	(2) TrEsp plan psol $\varepsilon = 2$	(3) TrEsp conf prot $\varepsilon = 2$	(4) TrEsp conf psol $\varepsilon = 2$	(5) TrEsp plan vac $\varepsilon = 1$	(6) TrEsp conf vac $\varepsilon = 1$	(7) PD Eq 3.18 $f = 0.8$
1-2	**-104**	**-101**	**-101**	**-98**	**-133**	**-130**	**-98**
1-3	5	3	5	3	7	7	5
1-4	-4	-4	-4	-4	-8	-7	-6
1-5	5	4	5	4	9	8	7
1-6	-18	-18	-16	-15	-24	-21	-15
1-7	-8	-8	-7	-7	-12	-11	-14
2-3	**34**	**25**	**33**	**24**	**39**	**38**	**31**
2-4	7	6	7	6	10	10	8
2-5	5	3	6	3	2	3	1
2-6	8	8	8	8	15	14	13
2-7	2	1	2	1	6	6	9
3-4	**-56**	**-52**	**-50**	**-45**	**-81**	**-72**	**-56**
3-5	3	1	-2	0	0	-1	-2
3-6	-8	-6	-8	-6	-11	-11	-10
3-7	6	7	1	2	3	3	3
4-5	**-70**	**-68**	**-71**	**-68**	**-87**	**-88**	**-66**
4-6	-16	-15	-15	-15	-24	-23	-18
4-7	**-58**	**-59**	**-58**	**-59**	**-70**	**-70**	**-58**
5-6	**76**	**77**	**70**	**71**	**97**	**89**	**89**
5-7	7	6	4	3	5	1	-3
6-7	**32**	**27**	**31**	**26**	**40**	**39**	**37**

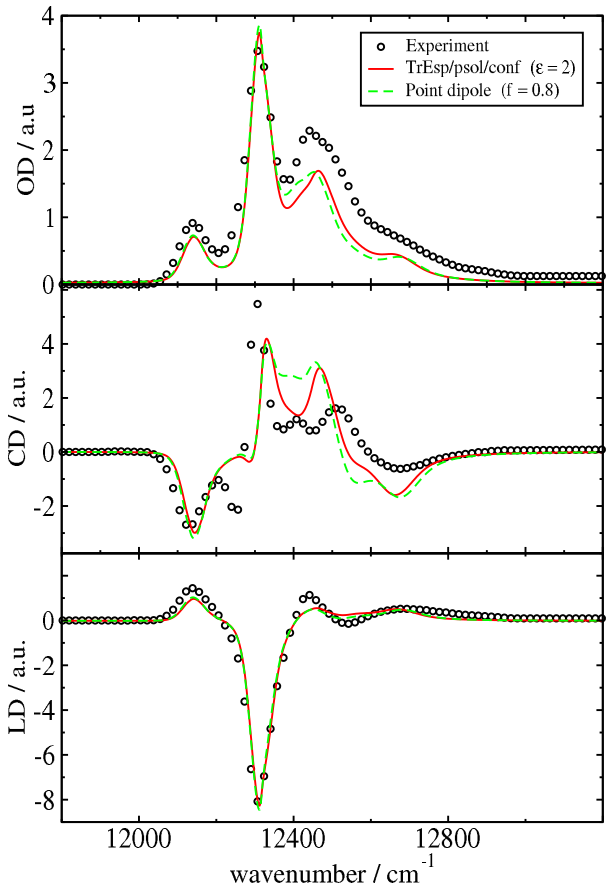

Figure 4.2: Comparison of 4 K absorption (OD), circular dichroism (CD) and linear dichroism (LD) experimental data [42] with calculations using site energies from PBQC in Table 4.5 and different methods for the excitonic couplings: The green dashed curves were obtained for couplings calculated in point dipole approximation with $f = 0.8$, assuming the transition dipoles to be oriented in $N_B - N_D$ direction. The red solid lines were obtained for the TrEsp/prot/solv (conf) couplings including the influence of the BChl conformations on the transition charges and on the orientations of local transition dipole moments $\vec{\mu}_m$.

4.2 Site Energies

The site energies presented in the following are obtained with the methods introduced in section 3.3. They are calculated for the FMO complex of *C. tepidum* and *P. aestuarii* , using the X-ray structures from the protein data bank, i.e., from Tronrud *et al.* [23] for *P. aestuarii* and Li *et al.* [24] for *C. tepidum*.

4.2.1 Site Energies from Fit of Optical Spectra

A genetic algorithm was used for a simultaneous fit of the OD, OD′ (derivative of OD), CD and LD spectra of *C. tepidum* and *P. aestuarii* (Adolphs & Renger [53]), measured by Vulto *et al.* [43] and Wendling *et al.* [42]. The temperature of measurement and simulation was 6 K for *C. tepidum* and 4 K for *P. aestuarii*. A width of 100 cm^{-1} for the distribution function of site energies gave the best agreement between the calculated and experimental spectra. The excitonic couplings in Table 4.1, column (4a/b) for *C. tepidum* respectively *P. aestuarii* were used in the optimization. The fit of site energies was performed for the monomeric as well as for the trimeric structure of the FMO complex, to evaluate the effect of the inter-monomer couplings. Later [67] it turned out that it is more realistic to use the monomer structure, because that includes implicitly the dynamic localization (see below).

The optimal site energies obtained from the fits are shown in Table 4.3. As one can see the maximum deviation of optimal site energies between monomer and trimer calculations (with high energy mode) is 70 cm^{-1} (BChl 7 of *P. aestuarii*) and the ranking of the site energies is almost identical. In accordance with some of the earlier results [42,43], pigment number 3 has the lowest site energy for *C. tepidum* and *P. aestuarii* and the largest deviation in site energies between the two species is obtained for BChl 5. The overall ranking in site energies obtained here, is almost identical to those obtained earlier by Vulto *et al.* [43] and Wendling *et al.* [42] as seen in Table 4.3. The spectra obtained for the present optimal site energies for monomers and trimers are compared in Fig 4.3 with the experimental data [42,43]. Although the spectra for the monomers and the trimers are very similar, there are some quantitative differences for the CD spectrum of *P. aestuarii*, that cannot be ignored. Hence all calculations of optical spectra in Adolphs & Renger [53] have been done for the trimeric structure. The quality of the trimer fit is very good for all spectra of *C. tepidum* and for OD and LD of *P. aestuarii* and somewhat weaker for CD of the latter.

Inspired by the further development of the structure based site energy calculations (PBQC by Müh *et al.* [26] and CDC, section 3.3.2) we revised the genetic fit and got same slightly changed new results: The FMO protein from *P. aestuarii* has been investigated with improved methods in Adolphs *et al.* [67]. Again the genetic algorithm was used for the fit of OD, OD′, CD and LD spectra of Wendling *et al.* [42] at 4 K. The differences to the calculations from Adolphs & Renger [53] are: (i) the high energy mode in the spectra simulation program is skipped, (ii) instead of the same inhomogeneous broadening we used different width for the seven pigments[2], and (iii) instead of using the trimeric structure, only monomeric structures were used, because the strongest excitonic coupling between two BChl*a* molecules in different FMO monomers is around an order of magnitude smaller than the local reorganization energy E_λ. Hence, the coherence between the excited states of these pigments is destructed by protein vibrations. This dynamical localization is included implicitly by assuming that delocalized states can be formed only between pigments of the same FMO monomer, i.e., we neglect inter-monomer excitonic couplings.

The optimal site energies obtained from these new fits for *P. aestuarii* are shown in Table 4.3. The highest deviation to the former results is obtained for BChl 5. The ranking order is the same as for the trimer fit from Adolphs & Renger [67] and Wendling *et al.* [42].

[2]We use different widths for the seven pigments. Pigment 1, 3, 4: fwhm = 60 cm^{-1} ; Pigment 2: fwhm = 100 cm^{-1} ; Pigment 5 - 7: fwhm = 120 cm^{-1}. This empirical assignment is based on the assumption that those BChls, which according to the crystal structure have more water molecules bound in their vicinity, should have a larger disorder because of the structural heterogeneity of the water molecules.

Table 4.3: Site energies in units of cm^{-1} for *C. tepidum* and *P. aestuarii* obtained from the fit of optical spectra in Fig 4.3 for FMO monomers and trimers, together with earlier fit results of Vulto *et al.* [43] and Wendling *et al.* [42]. The bold numbers give the rank starting with the smallest site energy.

	C. tepidum			*P. aestuarii*			
	Adolphs & Renger		Ref [43]	Adolphs & Renger		Adolphs *et al.*	Ref [42]
BChl	Monomer.	Trimer	Monomer	Monomer	Trimer	Monomer	Trimer
1	12445 **3**	12410 **3**	12400 **3**	12475 **5**	12445 **3**	12470 **4**	12430 **4**
2	12520 **6**	12530 **6**	12600 **7**	12460 **4**	12450 **4**	12450 **3**	12405 **3**
3	12205 **1**	12210 **1**	12140 **1**	12225 **1**	12230 **1**	12190 **1**	12175 **1**
4	12335 **2**	12320 **2**	12280 **2**	12405 **2**	12355 **2**	12380 **2**	12315 **2**
5	12490 **5**	12480 **5**	12500 **5**	12665 **7**	12680 **7**	12570 **7**	12625 **7**
6	12640 **7**	12630 **7**	12500 **6**	12545 **6**	12560 **6**	12565 **6**	12500 **6**
7	12450 **4**	12440 **4**	12430 **4**	12440 **3**	12510 **5**	12475 **5**	12450 **5**

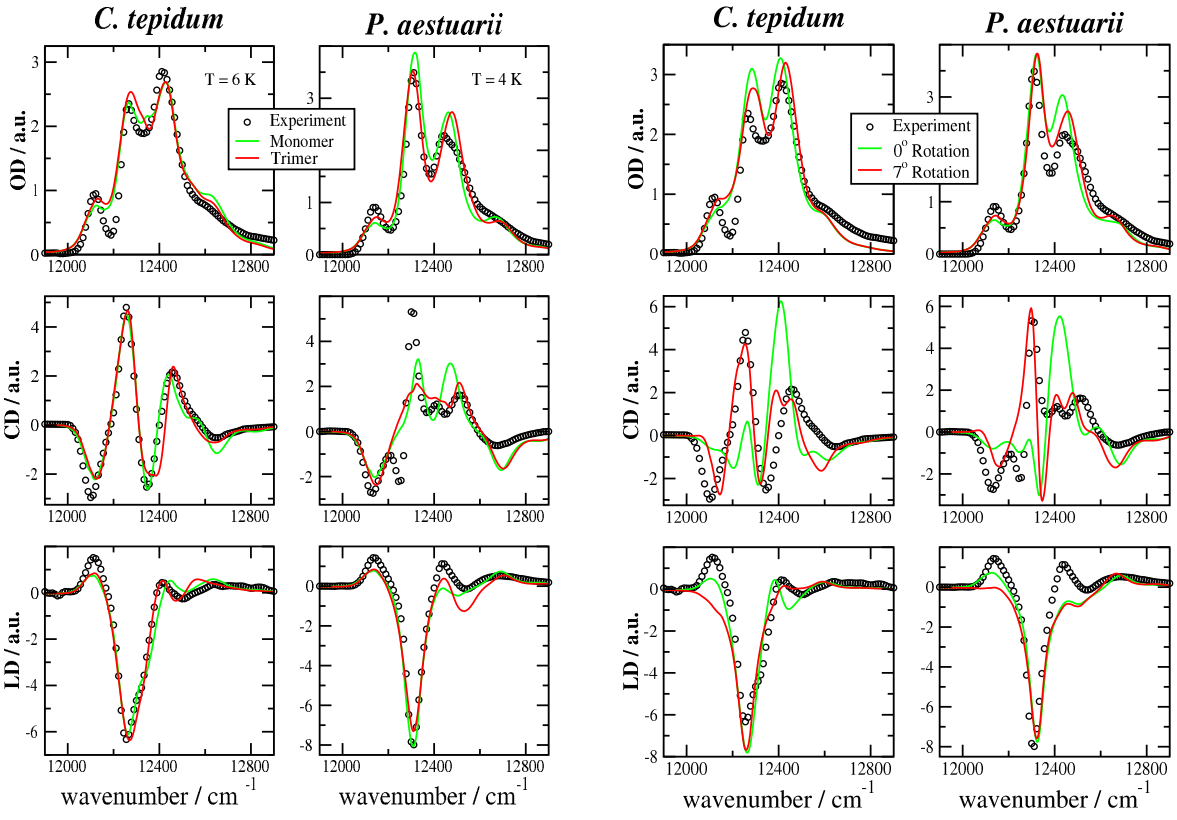

Figure 4.3: Low temperature optical spectra calculated for: *(Left)* optimal site energies from Table 4.3, depicted are monomer (green) and trimer (red) calculations. *(Right)* site energies from electrochromic shifts of Table 4.4 and partial fit of site energies of BChl 2 and 5 as explained in the text. The calculations were performed for the trimer structure assuming two different angles for the tilt of the Q_y transition dipole moment of the BChls toward their 13^1-keto-group: 0° (green line) and 7° (red line). The experimental data of Vulto *et al.* [43] for *C. tepidum* and of Wendling *et al.* [42] for *P. aestuarii* are shown as circles.

Table 4.4: Electrochromic shifts ΔE_m, obtained with PCD method (Eq 3.35) and respective site energies E_m from Eq 3.34 for monomeric FMO structure of *C. tepidum* and *P. aestuarii* in units of cm^{-1}.

BChl	*C. tepidum*		*P. aestuarii*	
m	ΔE_m $\varepsilon_{\text{eff}} = 3.8$	$E_0 + \Delta E_m$ $E_0 = 12315$	ΔE_m $\varepsilon_{\text{eff}} = 4.3$	$E_0 + \Delta E_m$ $E_0 = 12350$
1	115	12430	135	12485
2	-50	12265	-15	12335
3	**-105**	12210	**-135**	12215
4	120	12435	105	12455
5	**-70**	12245	**35**	12385
6	**195**	12510	**165**	12515
7	0	12315	30	12380

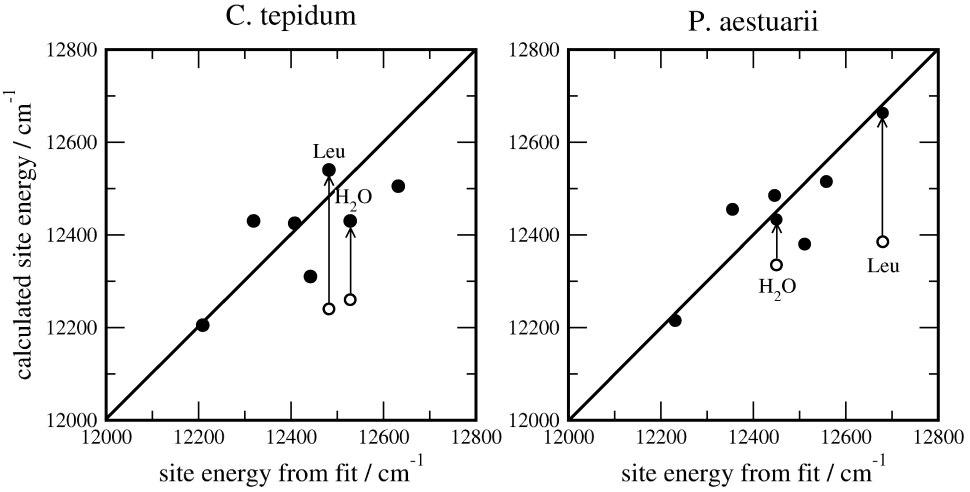

Figure 4.4: Correlation between site energies obtained from electrochromic shift calculations Table 4.4 and fit of optical spectra [53], for *C. tepidum (left)* and *P. aestuarii (right)*. The arrows indicate the shift of the electrochromic site energies of the two BChls which are not ligated by His, obtained from a partial fit as explained in the text.

4.2.2 Electrochromic Site Energy Shifts

First the results calculated with the CDC method are presented. The electrochromic shifts ΔE_i calculated by Eq (3.35) for monomeric FMO structures of *C. tepidum* and *P. aestuarii* are listed in Table 4.4. The strongest red shift is obtained for BChl 3 for both species. The largest difference between the two species is obtained for BChl 5. Whereas the site energy of this pigment shifts to the red in *C. tepidum*, it shifts to the blue in *P. aestuarii*. The main contributors to the redshift of BChl 3 are Arg-32, Asp-260, Lys-30, Lys-34, and Lys-267 in *C. tepidum* and their equivalents Arg-32, Asp-261, Lys-30, Lys-34, and Lys-268 in *P. aestuarii*. The situation is different for BChl 5, where the number of main contributors is much larger and the equivalence of the dominating charged amino acids is much less in the two species. A main contributor to the large blue shift of BChl 6 is its positively charged hydrogen bond donor ARG-95 which is conserved in both species and is responsible for one third of the difference in site energies between BChl 3 and BChl 6. The specific contributions of each titratable group to the electrochromic shift of the different pigments is given in the supplementary material of Adolphs & Renger [53]. The largest deviations between the fitted site energies in Table 4.3 and the values obtained from the electrochromic shift calculation in Table 4.4 are obtained for BChls 2 and 5, which are the only two pigments which are not ligated by histidine but by a water bridge to asparagine (BChl 2) and by leucine (BChl 5).

To take into account the influence of the different ligands on the site energy, a partial fit of the OD, OD', LD and CD spectra was performed using just the site energies of BChls 2 and 5 as fit parameters and applying the site energies obtained from the electrochromic shift calculations in Table 4.4 for the remaining five BChls. In case of BChl 5 which is ligated by leucine (Leu) in both species, *C. tepidum* and *P. aestuarii*, nearly the same blue shifts, 295 cm^{-1} and 280 cm^{-1}, respectively, with respect to the electrochromic shift values in Table 4.4, are obtained. In contrast, the site energy of BChl 2, which is bound by a water bridge, shifts differently in the two bacteria. A blue shift of 170 cm^{-1} results for *C. tepidum*, for *P. aestuarii* the shift is just 100 cm^{-1}. In other words the energy E_0 in Eq 3.34 is now assumed to depend on the ligand. The E_0^{His} for histidine (His) is equal to the E_0 in Table 4.4, for Leu it is $E_0^{\mathrm{His}} + 295\ \mathrm{cm}^{-1}$ and $E_0^{\mathrm{His}} + 280\ \mathrm{cm}^{-1}$ in *C. tepidum* and *P. aestuarii*, respectively and for water it is $E_0^{\mathrm{His}} + 170\ \mathrm{cm}^{-1}$ in *C. tepidum* and $E_0^{\mathrm{His}} + 100\ \mathrm{cm}^{-1}$ in *P. aestuarii*. A correlation plot of the electrochromic shift values (with and without partial fit) and the site energies obtained from the fit of the spectra is shown in Fig 4.4. The spectra calculated are compared in Fig 4.3 with the experimental data [42, 43]. The absorption and LD spectra fit very well, whereas for CD a much better agreement can be obtained if the direction of the $\mathrm{Q_y}$-transition dipole moment is rotated by 7° towards the 13^1-keto-group (IUPAC-numbering) with respect to the $\mathrm{N_I} \rightarrow \mathrm{N_{III}}$ (same as $\mathrm{N_B} \rightarrow \mathrm{N_D}$) axis of the BChls.

In the following the results published in Adolphs *et al.* [67], where only the FMO protein from *P. aestuarii* has been investigated, are presented. In Table 4.5, the site energies obtained by the fit are compared with those of the simple PCD approach [53], the sophisticated PBQC method [26] and the CDC [67] approach. In contrast to the calculations presented in Adolphs & Renger [53], where the electrochromic shifts have been calculated on the basis of the monomeric FMO structures, here the trimeric structure of the FMO protein from *P. aestuarii* is used for the electrochromic shift calculations (the spectra are calculated for the monomer structure). This causes the main difference of the results for *P. aestuarii* from Table 4.4 and the PCD-results from Table 4.5. A small contribution to the difference has its origin in the fact that in Adolphs & Renger [53] only the heavy atoms from the coordinates file are used, while in Adolphs *et al.* [67] also the hydrogen atoms are included. The correlation of the directly calculated and the fitted site energies (Table 4.5) is shown in Fig 4.5 (*left*). There is a significant improvement of the correlation when going from the PCD to the CDC approach. The correlation of the PBQC site energies with the values from the fit is the highest. The spectra obtained with the various sets of site energies are compared in Fig 4.7 with the experimental data [42]. The PCD spectra deviate strongly from the experiment, whereas there is a semi-quantitative agreement between the CDC spectra and the experiment. The PBQC calculations describe the experimental OD and LD spectra quantitatively and the CD spectra semi-quantitatively. The CDC and the PBQC method result in nearly the same E_0,

Table 4.5: Comparison of site energy shifts of the FMO protein from *P. aestuarii* obtained directly from the trimeric structure using different methods with values obtained from the fit. The values for ε_{eff} and E_0 in PCD and CDC were treated as parameters obtained from comparison with experimental data. The values 1.8/10.0 for the dielectric constant in PBQC refer to the dielectric constants used for the protein and the solvent respectively.

BChl	Fit	PCD	PBQC	CDC
1	-90 **4**	305 **7**	-150 **3**	5 **6**
2	-110 **3**	-10 **2**	-60 **5**	-180 **2**
3	-370 **1**	-130 **1**	-365 **1**	-380 **1**
4	-180 **2**	190 **6**	-165 **2**	-85 **4**
5	10 **7**	10 **3**	60 **7**	50 **7**
6	5 **6**	155 **5**	-50 **6**	-70 **5**
7	-85 **5**	90 **4**	-100 **4**	-135 **3**
ε_{eff}	–	1.8	1.8/10.0	2.5
E_0	12560	12320	12560	12540

Table 4.6: Site energy shifts $\Delta E_m \,/\, \mathrm{cm}^{-1}$ caused by certain parts of the PPC: Side chain groups (SC), ligands (Lig), protein backbone (BB), backbone of α-helices (Hel), explicitly modeled water molecules (Wat), hydrogen bonds (HB) and BChls. The calculations were performed with the CDC approach.

BChl	SC	Lig	BB	Hel	Wat	HB	BChl
1	95	15	-5	-25	-95	-85	10
2	-225	65	-20	-25	75	-115	-15
3	15	-35	-320	-225	0	-150	-80
4	130	10	-210	-185	15	-65	-20
5	145	40	-100	-20	30	0	-25
6	-80	0	60	55	25	-115	-75
7	-30	-35	40	115	-50	0	-95

whereas the one in the PCD approach is very different.

In accordance with some of the earlier fitting results [42, 43], pigment number 3 has the lowest site energy, independent of the method. The overall ranking in site energies obtained here from the fit is exactly identical to that obtained earlier [42].

In Fig 4.5 (*right*), the influence of the acetyl group conformation of BChls on the calculated site energies is investigated by taking into account the conformation of this group in the quantum chemical calculation of partial charges. Although there are some quantitative differences, the site energies obtained by using the same set of partial charges for all BChls are very similar. Therefore, all following calculations are performed neglecting the acetyl group conformation in the calculation of BChl partial charges. Here, we use $\varepsilon_{\text{eff}} = 2.5$ in Eq 3.36, as determined from the comparison of calculated CDC spectra and experimental data in Fig 4.7.

Influence of Certain Parts of the PPC

In the following the results of the investigation of certain parts of the FMO protein of *P. aestuarii*, investigated with the CDC method, are presented.

The advantage of a direct structure-based calculation of site energies is, that it is possible to identify the influence of certain parts of the protein. Here, we investigate the influence of the amino acid side chains, the protein backbone, the backbone of the α-helices, the water molecules, the hydrogen bonds and the BChls, using the CDC method. The resulting site energy shifts are summarized in Tables 4.6 and 4.7 and illustrated in Fig 4.6.

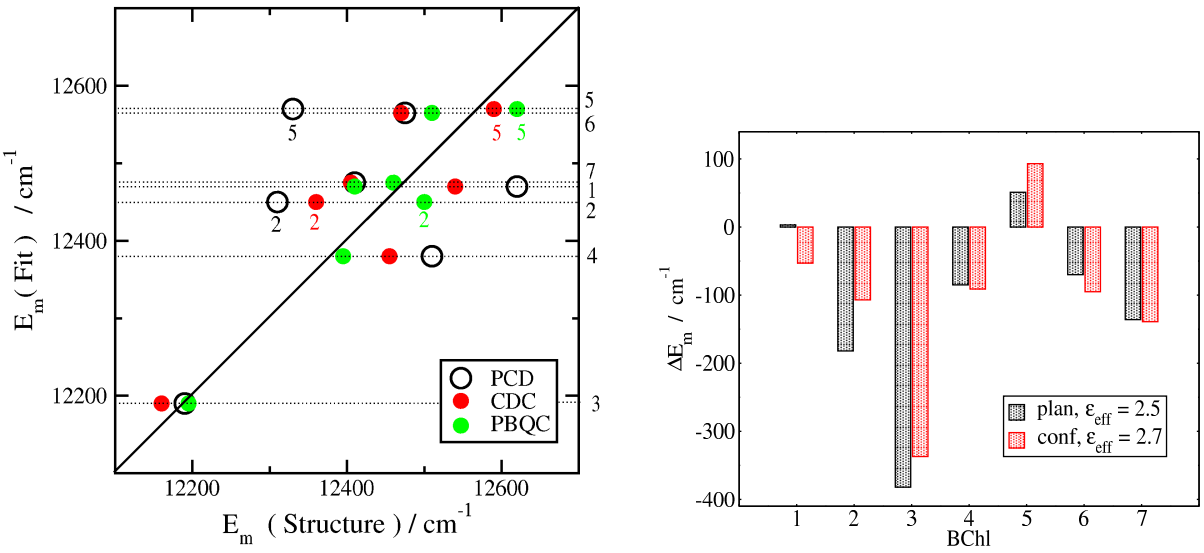

Figure 4.5: *(Left)* Correlation of (*P. aestuarii*) site energies calculated with PCD (black circles), CDC (red circles) and PBQC (green circles) with the site energies from the (monomer) fit, Table 4.5. The horizontal lines refer to the pigments (black numbers on the right axis). *(Right)* Site energy shifts $\Delta E_m/\mathrm{cm}^{-1}$ obtained by using partial charges of fully optimized BChl*a* (plan) or by taking into account the rotation of acetyl groups of the BChls as in the crystal structure (conf).

As seen in Fig 4.6 (*left*), the site energies of BChls are influenced by all of the contributions considered. Side chains have a large influence on BChls 1, 2, 4 and 5, the protein backbone is important for BChls 3 and 4, H-bonds lead exclusively to red shifts (BChls $1-4$, 6) and also the BChl – BChl charge density coupling has some influence (BChls 3, 6, 7). Interestingly, the large red shift of BChl 3 is due to its charge density coupling with the backbone of α-helix 5 and 6 (see Müh *et al.* [26]), as shown in detail in Table 4.7 (*left*) and Fig 4.6.

In the FMO complex, two types of hydrogen bonds to BChl appear, that differ in the H-bond acceptor group of BChl: H-bonds to the 3-acetyl group and to the 13^1-keto group. Two BChls are without hydrogen bonds (BChl 5 [3] and 7), one has a H-bond to a water molecule (BChl 1), and four (BChl 2, 3, 4, 6) have up to three H-bonds to amino acids (Ala, Arg, Ile, Ser, Trp, Tyr). The detailed contributions of these groups are given in Table 4.7 (*right*).

4.3 Exciton Relaxation

In the following the temporal and spatial relaxation of excitons is calculated in the monomeric subunit of the FMO complex of *C. tepidum*. The exciton dynamics in *P. aestuarii* is very similar and therefore not shown.

4.3.1 Delocalization of Excitons

The delocalization of excitons in the FMO complex is investigated by the disorder averaged exciton states pigment distribution function $d_m(\omega)$ (see Eq 2.13) that describes the contribution of a given pigment m to the different exciton states [32]. In Fig. 4.9 the function $d_m(\omega)$ for the 7 pigments of the FMO-monomer of *C. tepidum* is compared with the density of exciton states $d_M(\omega)$, Eq 2.14. In the calculations, the site energies obtained from the genetic fit (trimer) in Table 4.3 were used. It is seen, that the excited states

[3] The close proximity of one water molecule to the 13^1-keto group of BChl 5 suggests formation of an H-bond there, but in our structural model this water molecule is oriented towards the negatively charged Asp 234, so that no H-bond is formed. Turning the water molecule towards the 13^1-keto group of BChl 5 results in a moderate red shift of $\approx 50\ \mathrm{cm}^{-1}$.

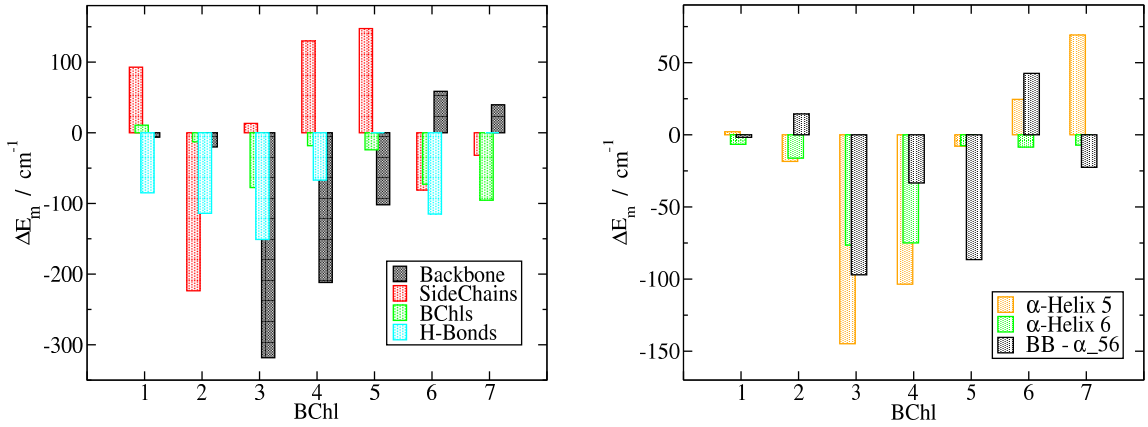

Figure 4.6: *(Left)* Site energy shifts $\Delta E_m \,/\, \mathrm{cm}^{-1}$ (Table 4.6) caused by the backbone, side chains, BChls and H-bonds. *(Right)* Site energy shifts $\Delta E_m \,/\, \mathrm{cm}^{-1}$ caused by α-helices 5 and 6 and the remaining backbone (Tables 4.6 and 4.7, *left*).

Table 4.7: *(Left)* Site energy shifts $\Delta E_m \,/\, \mathrm{cm}^{-1}$ caused by the backbone of certain α-helices, obtained with the CDC method. *(Right)* Site energy shifts $\Delta E_m \,/\, \mathrm{cm}^{-1}$ caused by hydrogen bond donors, obtained with the CDC approach. In the second column, the hydrogen bond donor is specified, where (B) indicates that the backbone is the H-bond donor. The side chain of Arg 95 is positively charged.

BChl	α-Helix					
	1	2	3	4	5	6
1	5	-35	5	5	0	-5
2	-5	-10	15	10	-20	-15
3	0	-5	-5	5	-145	-75
4	0	0	0	-10	-105	-75
5	-5	-5	0	10	-10	-10
6	0	15	-20	45	25	-10
7	15	20	25	-10	70	-5

BChl	H-Bond donor	H-Bond acceptor	ΔE cm^{-1}
1	H_2O	3-acetyl	-85
2	Ser 72	3-acetyl	-57
	Ile 137 (B)	13^1-keto	-36
	Tyr 138 (B)	13^1-keto	-21
3	Tyr 15	3-acetyl	-103
	Ala 40 (B)	13^1-keto	-48
4	Tyr 345	13^1-keto	-67
5	-	-	-
6	Trp 184	3-acetyl	-40
	Arg 95	13^1-keto	-75
7	-	-	-

of the pigments contribute to more than one exciton state. BChl 1 and BChl 2 form an excitonic hetero dimer and dominate exciton levels 3 and 6. BChls 3 and 4 dominate the two lowest exciton levels 1 and 2, and BChl 4 has additional contributions in exciton levels 4 and 5. The excited states of the remaining pigments $5-7$ are distributed over $2-4$ different exciton states predominantly in the blue side of the spectrum.

4.3.2 Spectral Density and Exciton Relaxation

The spectral density $S_0 J_0(\omega)$ that is used in the calculations of exciton relaxation is compared in the upper part of Fig. 3.3 to the vibrational sideband measured by Wendling *et al.* [44] on the FMO complex of *C. tepidum*. The $J_0(\omega)$, that was originally extracted from fluorescence line narrowing spectra of B777-complexes [30], is similar to the experimental sideband measured for *C. tepidum*. Based on this comparison a high frequency vibrational mode with a wavenumber of 180 cm^{-1} was included in the calculation of optical spectra in addition to the low-frequency part $S_0 J_0(\omega)$, as noted before.

The lower part of Fig. 3.3 contains the function $\tilde{C}^{(\mathrm{Re})}(\omega)$ that is obtained from the spectral density

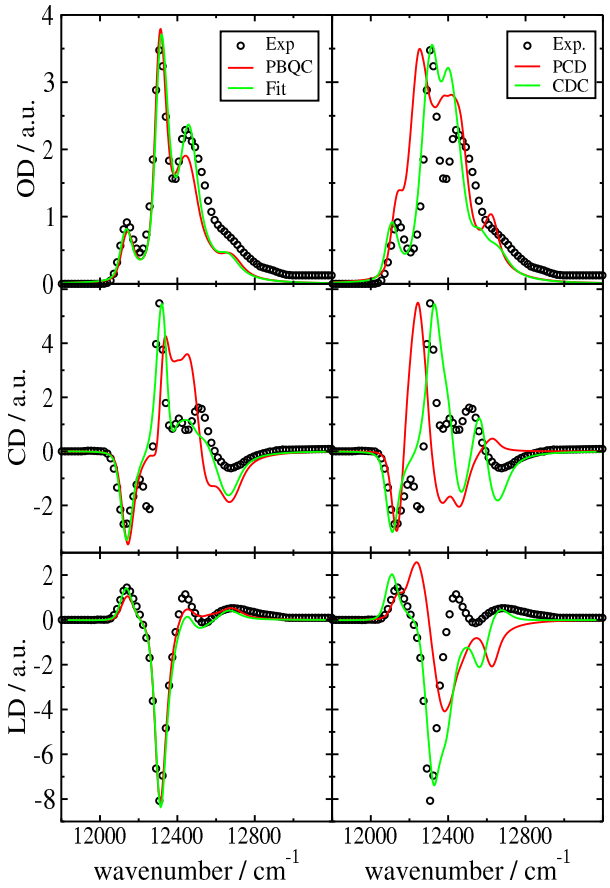

Figure 4.7: Comparison of 4 K absorption (OD), circular dichroism (CD) and linear dichroism (LD) experimental data [42] (circles) with calculations, using the site energies obtained with different methods (Table 4.5) and a point dipole approximation for the excitonic couplings (Eq 3.18, $f = 0.8$).

$S_0 J_0(\omega)$ in the upper part of this figure by Eq. 2.24. Whereas the $S_0 J_0(\omega)$ peaks at about 20 cm^{-1} the quadratic ω dependence of $\tilde{C}^{(\mathrm{Re})}(\omega)$ shifts the maximum to larger energies at around 200 cm^{-1}. The vertical bars in the lower part of this figure contain the function γ_{MN} in Eq. 2.20 at the average energetic position of the exciton transition energies $\hbar\omega_{MN}$. The $\tilde{C}^{(\mathrm{Re})}(\omega)$ covers the whole range of transition energies between the different exciton states.

4.3.3 Exciton Relaxation after Excitation by a Short Pulse

The population of exciton states after initial excitation by a 50 fs (fwhm) pulse centered at the blue edge (12626 cm^{-1}) of the spectrum was calculated and is shown in Fig 4.8 (*left*). For comparison, Redfield (solid lines) as well as modified Redfield (dashed lines) rate constants were used in the calculation of exciton relaxation. The two types of rate constants give very similar results, the modified Redfield theory predicts slightly slower exciton relaxation. The pulse, which is spectrally broad, populates exciton levels $2-7$. The high energy exciton state populations decay on a subpicosecond time scale and the low energy ones on a picosecond timescale. After 4 ps the lowest state and to a very minor extent the third exciton state carry the whole excitation.

4.3.4 Exciton Relaxation Perpendicular to the Trimer Plane

It is finally investigated how the transfer of excitation energy occurs along the normal of the trimer plane. For this purpose as an initial condition the exciton states which have the largest contribution of pigments

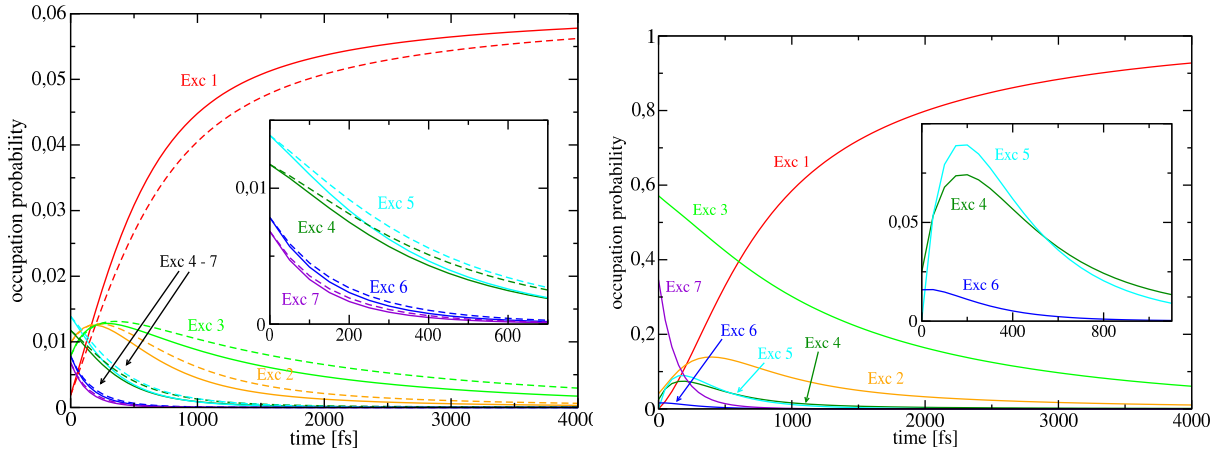

Figure 4.8: *(Left)* Disorder averaged population dynamics of exciton states, after optical excitation with a 50 fs pulse centered energetically at 12626 cm^{-1}. The solid lines were obtained using Redfield theory rate constants (Eq. 2.61) and the dashed lines show the modified Redfield theory results.
(Right) Disorder averaged population dynamics of exciton states calculated in Redfield theory, where the initial population was created assuming that the excitation energy arrives from above the trimer in Fig. 4.10 as explained in detail in the text.

1 and 6 located on the upper part of the trimer in Fig. 4.10 were populated, weighted by the transition dipole moment square of those exciton states. The evolution of exciton state populations $P_M(t)$ for this initial condition is shown in Fig. 4.8 (*right*). At time zero mainly exciton states 3 and 7 are populated. The subsequent relaxation times of the two populations differ by an order of magnitude. The exciton initially on exciton state 7 relaxes within 200 fs and the one on state 3 in 2 ps. The corresponding local occupation probabilities of the pigments, $P_m(t) = \sum_M |c_m^{(M)}|^2 P_M(t)$ are shown in the lower part of Fig. 4.10 for three different times. At time zero BChls 1, 2, 5, and 6 in the upper half of the trimer carry the excitation. After 200 fs, all the pigments are excited, at 1 ps the excitation is localized on pigments $1-4$, and after about 5 ps the equilibrated excited state of the complex is reached were only pigments 3 and 4 at the bottom of the trimer are in the excited state.

4.4 Discussion

Discussion of the Results for *C. tepidum* and *P. aestuarii*

For the first time, a convincing correlation between two independent calculation methods of pigment transition energies in proteins, the so-called site energies, is obtained [53]. The site energies of FMO complexes from two different green sulfur bacteria, *P. aestuarii* and *C. tepidum*, were obtained from a fit of optical spectra and, independently, by a calculation of electrochromic shifts due to charged amino acids. The three main results of those calculations are (i) pigment number three has the lowest site energy, (ii) for pigment number five the strongest deviation occurs between the two species and (iii) for the five BChls which are bound to His, BChl 6 has the largest site energy. From the two possible orientations of the FMO trimer relative to the membrane, that were identified by LD measurements on isolated FMO trimers and membrane fragments [88], only the one with BChl 3 at the bottom and BChl 6 at the top allows for an efficient transfer of excitation energy to the reaction center.

From the earlier fits [42, 43, 86, 89–92] those by Vulto [43] and Wendling [42] predicted the correct site energies. The main difference between the present and those two earlier fits [42, 43] is the use of a more advanced theory for optical spectra that results in a better agreement with experimental data, and the explanation of the low effective dipole strength used in the calculation of the excitonic couplings. The effective dipole strength $f\mu_{\mathrm{vac}}^2 = 30\ \mathrm{D}^2$ obtained here justifies the earlier use of similar

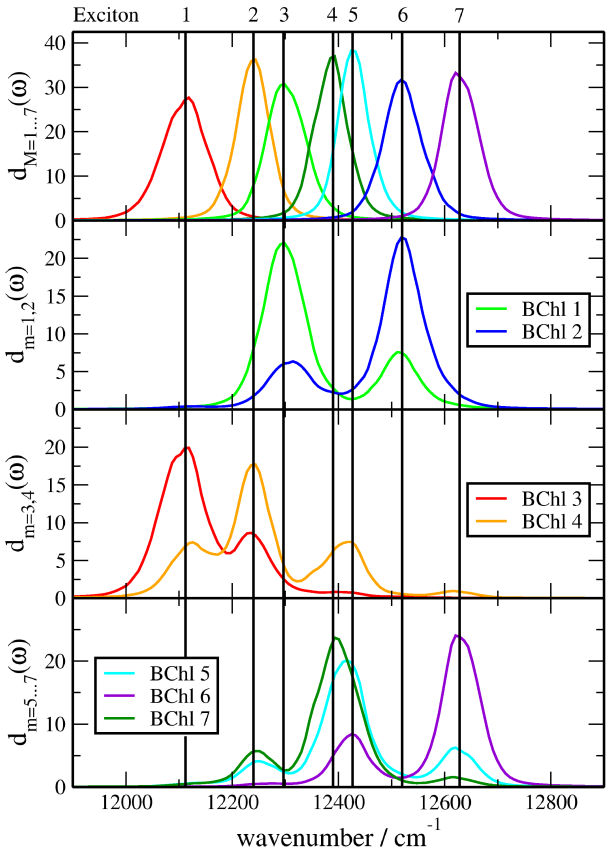

Figure 4.9: The top part contains the disorder averaged density of exciton states $d_M(\omega)$ defined in Eq. 2.14, and the lower parts the exciton states pigment distribution functions $d_m(\omega)$ in Eq. 2.13.

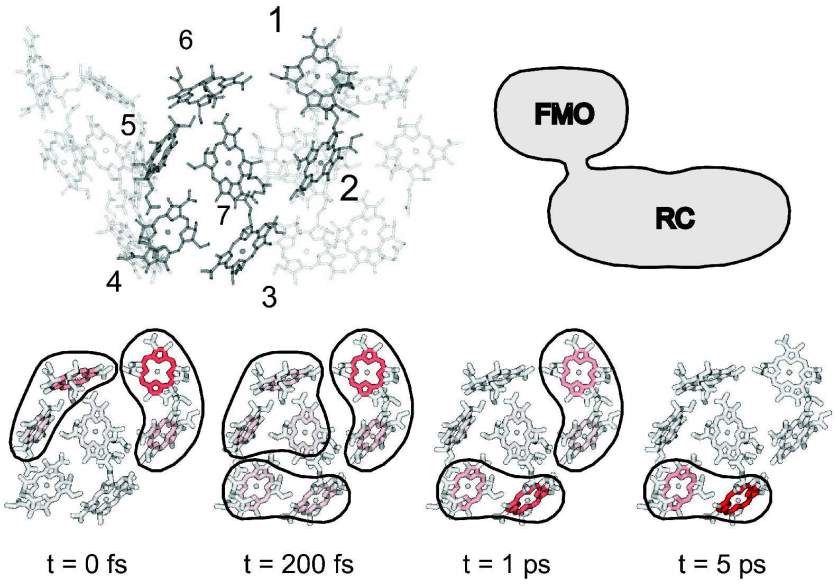

Figure 4.10: *Left upper part:* BChls of the FMO trimer. The BChls $1-7$ of one monomeric subunit are high lighted (numbering according to Fenna and Matthews [2]). *Right upper part:* sketch of the mutual arrangement of the FMO complex and the reaction center, as obtained from an electron-microscopic study [11, 22] Lower part: spatial and temporal relaxation of excitons from the top to the bottom of the complex. As initial condition the exciton states with large contributions from BChls 1 and 6 were populated. The color of the π-system of the BChls is varied between light and dark red according to the population of the excited states. The enclosed areas mark the delocalized exciton states that are populated (see also Fig. 4.8, *right*).

low values $f\mu^2_{\rm vac} = 29$ D^2 in [43] and $f\mu^2_{\rm vac} = 31$ D^2 in [42], which have been treated essentially as fit parameters. The present explanation of the effective dipole strength is based on electrostatic calculations of the Coulomb coupling between transition charges of BChl in the dielectric environment of the protein, assuming an optical dielectric constant $\varepsilon = 2$ for the latter and a vacuum dipole strength of $\mu^2_{\rm vac} = 37.1$ D^2 as determined recently by Knox & Spring [18] for the present empty cavity model. The explanation of the low effective dipole strength is important since, it seems, the use of a higher dipole strengths ($51 - 55$ D^2) prevented the other fits [89–92] from finding the right site energies.

However, also for the present low effective dipole strength it is not guaranteed that there exists a unique fit and that there is no other set of site energies which can explain the spectra. In the present study we tried to minimize this possibility by a check of the genetic algorithm using calculated spectra as a test set for the algorithm. However, a real proof of the global minimum requires an independent determination of the site energies. Such a determination was achieved here by the calculation of electrochromic shifts in site energies due to charged amino acids. Although, as the correlation plot in Fig 4.4 shows, there are deviations between the fitted and directly determined site energies, there is a clear correlation. In particular the large difference in site energies between BChl 3 and BChl 6 in the genetic fit is well reproduced by the electrochromic shifts, allowing to decide about the orientation of the FMO trimer relative to the membrane containing the reaction center. The red shift of BChl 3 and the blue shift of BChl 6 are caused by charged amino acids that are conserved in the two bacteria, as for example the positively charged hydrogen bond donor ARG-95 of BChl 6.

The effective dielectric constants $\varepsilon_{\rm eff}$ of 3.8 and 4.3 inferred from the electrochromic shift calculations for *C. tepidum* and *P. aestuarii*, respectively, are in between earlier values estimated for the two branches of bacterial reaction center [84] and agree also with values for the dielectric constant of proteins obtained independently: From molecular dynamics calculations [93, 94] and normal mode calculations [95] using Kirkwood-Fröhlich dielectric theory a dielectric constant in the range of $2 - 6$ has been calculated for the interior of proteins. A value of $\varepsilon_{\rm eff} = 4$ is routinely used in calculations of redox potentials of cofactors in proteins [96–99].

The major deviations between the electrostatic calculations and the fitted values of site energies are obtained for the two BChls which are not ligated by His. To take into account the effect of the ligand a partial fit was performed, where the two site energies of the pigments with non-His ligand were optimized. In agreement with mutation studies, which suggest that His ligands lead to low transition energies [100], a blue shift of the site energy of the two BChls which are not ligated by His is obtained from the partial fit. A reason for the low transition energies of the BChls with a His ligand might be the large polarizability of the conjugated π-electrons of His that results in a large dispersive interaction [101–103] which is known to yield a red shift of the transition energy. Taking into account the effect of the ligand, there is an approximately equal additional blue shift of the site energies of BChl 5, which is bound by Leu, for, both, *C. tepidum* and *P. aestuarii*. In contrast, the site energy of BChl 2, which is bound by a water bridge to Asn-79 (asparagin), shifts differently for the two species. An inspection of the water ligand of the Mg atom of BChl 2 in the structures reveals that the Mg-O distance in *C. tepidum* is 2.4 Å, whereas in *P. aestuarii* it is just 1.9 Å, a difference that might explain the different shifts of the site energies of BChl 2. A reason for the different position of the water molecule could be that one neighboring amino acid of Asn 79, which binds the water, is different in the two species. Mutation studies would be helpful to clarify this point.

The optical spectra calculated from the electrochromic and the two partially fitted site energies in Fig 4.3 agree surprisingly well despite the simplicity of the model. The agreement suggests that the major contribution to the shift in site energies in the present system is from charged amino acids and the ligands. In particular, these effects explain the difference in the absorption spectra between the two bacteria, i.e., the switch in relative intensity of the two main bands. A major contributor to this switch is BChl 5 which is the only pigment for which the electrochromic shift in Table 4.4 has a different sign in the two species.

The largest deviation between experimental and calculated spectra occur for the CD spectra, both

of *C. tepidum* and *P. aestuarii*. Those deviations might have several reasons, the neglect of site energy shifts by hydrogen bonds, by the different conformations of the pigments and by different protonation states of the titratable groups of the protein. We are currently investigating those effects in detail. Alternatively, the deviations in the CD spectra become much smaller when a 7° rotation of the Q_y transition dipole moment of the BChls towards the 13^1-keto-group is assumed. It is interesting to note that such a rotation is discussed in the literature for bacteriochlorophyll *a* [104, 105] and for the related chlorophyll *a* molecule [106, 107]. The exact value of the tilt angle is still an open question, and might depend also on the protein environment. From experiments on BChl*a* embedded in a liquid crystal matrix, evidence was reported for a partial x-polarization of the Q_y transition [104], that depends on the type of matrix environment. In [105] an angle of 7° has been inferred for the $B850_\alpha$ BChls of the LH2 light-harvesting complex on the basis of modeling CD data. For chlorophyll *a*, from an analysis of time resolved fluorescence anisotropy measurements on the peridinin-chlorophyll-*a*-protein, an angle of $(4.5 \pm 2.5)^\circ$ was estimated [107]. An angle of 20° was reported [106], based on linear dichroism experiments on chlorophyll *a* oriented in a lamellar phase of glycerylmonooctanoate/H_2O.

By the tuning of site energies, the proteins can trigger the spatial and temporal way of excitons through the FMO-complex, on their way from the outer antenna, the chlorosomes, to the reaction center. Since this spatial transfer is connected with an energetic relaxation, on the basis of the site energies determined here, we conclude that the linker pigments between the FMO complex and the reaction center are BChls 3 and 4 which form the lowest exciton state (Fig 4.9) and are situated at the bottom of the trimer shown in Fig 4.10. The actual calculation of exciton relaxation, either initiated by assuming an excitation by an ultrashort optical pulse or by assuming that the excitation arrives from above the trimer, where the chlorosomes are situated in *vivo*, reveals the occurrence of a fast subpicosecond as well as a relatively slow picosecond transfer branch of excitons between the upper part of the trimer and the bottom containing BChls 3 and 4. The fast branch involves BChls 5, 6 and 7, and the slow branch BChls 1 and 2. It is not clear whether there is a physiological significance of the difference of one order of magnitude in relaxation times between the two branches. Those different relaxation times were found also in transient absorption measurements [108, 109] as discussed in the introduction. A difference of the present calculations with respect to the earlier Redfield calculations [108] is the use of the correct $\tilde{C}^{(\mathrm{Re})}(\omega) \propto \omega^2 J(\omega)$ instead of the $\tilde{C}^{(\mathrm{Re})}(\omega) \propto J(\omega)$ that incorrectly favors relaxation between exciton state with small energy differences. In addition, the present study contains an estimation of the maximum rate constants (obtained for uncorrelated fluctuation of site energies) of exciton relaxation without using a free parameter to adjust the relaxation times [108]. A difference between the present calculation of exciton relaxation with the modified Redfield/Förster theory study [109] is the use of a spectral density that was extracted from experiments and the comparison of the modified Redfield theory with the much simpler Redfield theory. The spectral density that was originally extracted from calculations of fluorescence line narrowing spectra of B777-complexes is very similar in shape to the fluorescence line narrowing spectrum measured on the FMO-complex of *C. tepidum* (Fig 3.3). This similarity, that is also found with respect to spectral densities extracted for other complexes [110, 111], suggests that the local modulation of pigment transition energies by the protein environment is a global quantity that does not so much differ for the specific environments of the pigments. The comparison of the relaxation dynamics obtained in modified Redfield theory with that in Redfield theory in Fig 4.8 (*left*) shows that there are only minor differences. The slightly slower modified Redfield rates might be due to the barriers created between the excitonic PES due to their mutual shifts which are neglected in Redfield theory. On the other hand the delocalization of excited states leads to rather large off-diagonal parts of the exciton vibrational coupling, and so there are also corrections to the modified Redfield rates due to the fact that the nuclei do not relax in the excitonic PES determined solely by the diagonal part of the exciton vibrational coupling.

An advantage of Redfield theory is the simple form of the rate constant that allows to analyze the different relaxation channels, present in the FMO complex. We focus therefore on the Redfield rate constant in Eq. 2.23 in the following. The latter is given as a product of the function γ_{MN} in Eq. 2.20 and $\tilde{C}^{(\mathrm{Re})}(\omega_{MK})$ in Eq. 2.24. The former contain the exciton coefficients and the correlation radius

of protein vibrations that describes in an effective way how the fluctuation of site energies of different pigments are correlated. In the limit $R_c \rightarrow \infty$ we have $\gamma_{MN} = \delta_{MN}$, i.e. there is no relaxation of excitons, whereas the fastest relaxation occurs for uncorrelated fluctuations of site energies. In this case $\gamma_{MN} = \sum_m |c_m^{(M)}|^2 |c_n^{(M)}|^2$, i.e. relaxation occurs between such exciton states which have contributions from the same pigments. From a comparison with relaxation data measured in transient absorption experiments [54, 108, 112, 113] it can be concluded that the site energies of the pigments in the FMO complex fluctuate rather uncorrelated, i.e., $R_c < 10$ Å [4]. Important insights into the relaxation channels are obtained by investigating the disorder averaged exciton states pigment distribution functions $d_m(\omega)$, shown for *C. tepidum* in Fig 4.9. As seen there, BChl 1 and BChl 2 form an excitonic dimer, there are no major contributions from those two pigments in other exciton states, explaining why the γ_{31} and γ_{32} and therefore the exciton relaxation rates from exciton state 3 to the lower states are so small. In contrast, the remaining pigments via their exciton states distributions efficiently connect the remaining exciton states and lead to the fast subpicosecond relaxation times. The disorder averaged factors γ_{MN} are shown as bars in the lower part of Fig 3.3 together with the function $\tilde{C}^{(\mathrm{Re})}(\omega)$ which describes how well the protein vibrations can dissipate the excess energy of excitons during relaxation. The respective transition energies that occur during relaxation, depicted by the energetic position of the γ_{MN} bars, fit very well into the energetic range of the function $\tilde{C}^{(\mathrm{Re})}(\omega)$, which at low temperature is proportional to $\omega^2 J(\omega)$ with the $J(\omega)$ from the upper part of this figure. It is seen thereby that the spectral density of the pigment-protein coupling is well optimized to dissipate the excess energy of excitons during relaxation.

The present method of obtaining site energies and excitonic couplings from electrostatics calculations provides an additional basis for the elucidation of structure function relationships in pigment-protein complexes and a testing ground for the development of dynamical theories. The latter will allow for a more complete comprehension of the rich information contained in the newly measured 2D photon echo spectra [109, 115]. The present calculations of excitonic couplings show that it is very unlikely that the second strongest excitonic coupling occurring between BChl 5 and 6 in the FMO complex is reduced by almost 60 % with respect the to coupling obtained in point dipole approximation, a reduction that was inferred from the calculation of the photon echo spectra [109, 115]. Neither deviations from the point dipole approximation nor the influence of the dielectric protein environment support this reduction. Besides the point dipole approximation, which in the present study is shown to be valid, Cho *et al.* [109, 115] pointed out that another approximation in the calculations of the photon echo spectra, that could be crucial, was the neglect of electronic coherence transfer terms in the non – linear polarization. It is interesting to note that although those terms were found to be small in the calculations of linear absorption spectra of the LH2-light harvesting complex [116], in the calculation of non – linear fluorescence anisotropy decay spectra on the same complex they were reported to be important [117]. Another correction that could improve the agreement between the calculated and measured photon echo spectra concerns the detuning of two exciton state energies [118], for example, by intramolecular excited state absorption of the BChls [92].

Conclusions

Based on two independent methods, using a fit of optical spectra with a genetic algorithm, and by direct electrochromic shift calculations, the site energies of the 7 BChls in the FMO monomeric subunits of the FMO-complexes of *C. tepidum* and *P. aestuarii* were determined and used to calculate the spatial and temporal relaxation of excitons. From those calculations it can be concluded: (i) the most important contributions to the shift in site energies are due to charged amino acids and the ligands, (ii) the charged amino acids are responsible for the low site energy of BChl 3, the large site energy of BChl 6 and the large difference in site energy of BChl 5 between *C. tepidum* and *P. aestuarii*, (iii) histidine ligands lead to lower site energies than leucine or water, (iv) in order to allow for efficient excitation energy

[4] A value of $R_c = 5$ Å is used, that was determined from transient spectra of photosystem II reaction centers in [114]. The stationary spectra calculated here do not depend critically on this value.

transfer to the reaction center, the relative orientation of the FMO trimer with respect to the reaction center is such that BChls 3 and 4 are at the interface between the two complexes, (v) exciton relaxation through the FMO complex between the chlorosomes and the reaction center in green sulfur bacteria occurs along a fast subpicosecond and a slow picosecond branch. The present simple electrostatic method of calculating site energies can be readily applied to larger complexes for which an unambiguous fit of site energies from optical spectra is not possible because of the large number of pigments, and hence the large number of parameters. The advantage of an electrostatic method, compared to a solely quantum chemical method [87, 119], is that the whole protein, and not just a small environment of the pigments, can be included in the calculations. At the moment, the method is developed further by performing an average over the different protonation states of the titratable groups, using a more sophisticated electrostatic description in atomic detail that is capable also of including the effect of hydrogen bonds, the influence of the charge density of the neutral amino acid residues and the influence of the water/glycerol dielectric environment.

Discussion of Molecular Details

As seen in Figs 4.5 (*left*) and 4.7, there is an impressive improvement in accuracy of site energies calculated with the new CDC method compared to our earlier PCD approach. The RMSD between the site energies directly calculated and those obtained from the fit decreases from 245 cm^{-1} in PCD to 65 cm^{-1} in CDC and to 40 cm^{-1} in PBQC. The significant improvement between PCD and CDC demonstrates the importance of the charge density of neutral amino acid residues and of the correct description of the difference potential of BChls, which allows now to describe also hydrogen bonding effects to the 13^1-keto and 3-acetyl groups.

In our earlier PCD calculations, it was necessary to readjust the site energies of BChls 2 and 5 by performing a partial fit. The resulting blue shifts of E_2 and E_5 were ascribed to the different nature of the axial ligands of these BChls, i. e., water and the backbone of Leu, respectively, compared to His [53]. An inspection of the ligand contributions to the site energy shifts in the CDC approach in Table 4.6 shows that indeed the strongest blue shifts are obtained for BChl 2 and 5. However, the magnitudes are smaller than predicted by the partial fit, indicating a certain amount of error compensation in our earlier approach.

As with the PBQC approach [26], it turns out with the CDC method that the dominating effect on the energy sink at BChl 3 is due to the electric field of the backbone of α-helices 5 and 6. The dipole moments of these α-helices amount to 33 D and 37 D, respectively. The large dipole moments of α-helices were suggested to stabilize the structure of helix bundles [120] and were found important for the tuning of redox potentials in photosynthetic reaction centers [121]. The present and our recent PBQC results [26] provide clear evidence that α-helices can tune transition energies of pigments and, in this way, direct the energy flow. The mechanism of this tuning can be understood in the following way. As reported by [120], the electric field of an α-helix can be well approximated by two partial charges of opposite sign and a magnitude of 0.5 elementary charges, placed at the ends of the helix. As seen in Fig 4.11 (*left*), the positive partial charge of α-helix 5 is located in the negative difference potential $\Delta\phi$ and the negative partial charge in the positive $\Delta\phi$ of BChl 3. Therefore, a larger stabilization of the excited state and hence a red shift of the site energy results. This red shift is further increased by α-helix 6 which, however, points away from BChl 3 so that only its negative end contributes significantly.

In qualitative agreement with experimental results on other antenna systems [122], hydrogen bond donors to BChl cause red shifts of the site energies as seen in Fig 4.6 (*left*) and Table 4.7 (*right*). The result that hydrogen bonds always lead to red shifts can be understood on the basis of the difference potential in Fig 4.11: It is negative around the acetyl and the keto group. A hydrogen bond donor from the protein will place a partially positively charged hydrogen atom into the negative difference potential, causing thereby a red shift of the transition energy. As an example, the site energy shift of BChl 2 by the hydrogen bond of its 3-acetyl group with Ser 72 is illustrated in Fig 4.11 (*center*).

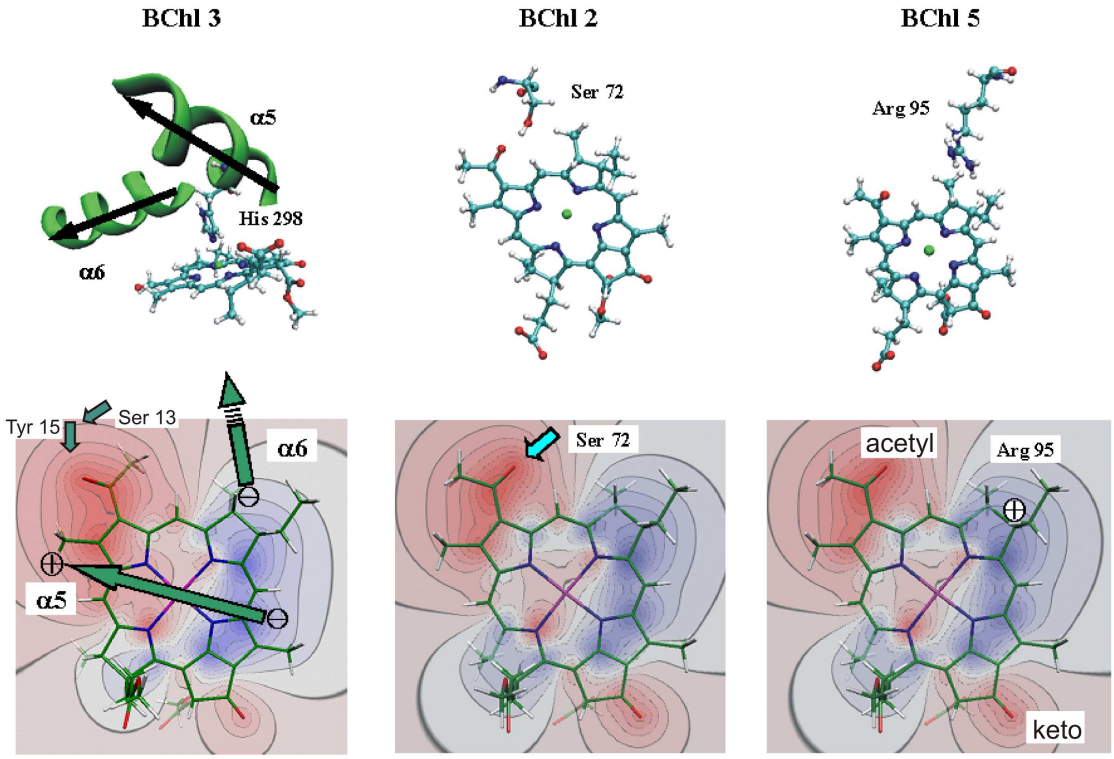

Figure 4.11: Dominant influence of local protein environments on optical transition energies of BChl 3, 2, and 5. The upper part contains structural elements (α-helices, hydrogen bond donors, charged amino acid residues) and the lower part places the charge distribution of these elements relative to the difference in electrostatic potential $\Delta\phi(r) = \phi_{11}(r) - \phi_{00}(r)$ between excited state S_1 and ground state S_0 of BChl*a* [49], shown as a contour plot in the plane of the pigment. *Blue:* Positive potential values. *Red:* Negative potential values.

Besides the α-helices and the hydrogen bond donors, the charged amino acid residues influence the site energies. The largest blue shift of a site energy in the present system is caused by the positively charged Arg 95 that is located in the positive $\Delta\phi$ (blue) of BChl 5 (Fig 4.11, *right*). We note that this residue is calculated to be protonated in the PBQC approach, i. e., the standard protonation state assumed in CDC is correct for this group. In general, however, the titratable residues could be in a non-standard state.

Therefore, the best description of experimental data is obtained with the PBQC method, which includes an average over the protonation probabilities and takes into account polarization effects in a more sophisticated way by solving a Poisson-Boltzmann equation. Assuming a standard protonation pattern in the PBQC approach results in a broader spectrum, i. e., the maximal difference between site energies is 495 cm^{-1} compared to 425 cm^{-1} in the non-standard protonation pattern [26]. This effect is compensated for in the CDC method by using a higher effective dielectric constant, resulting in a maximal site energy difference of 430 cm^{-1}.

These results are very valuable because one can exploit it in calculations of the spectral density $J(\omega)$ of the pigment protein coupling by combining CDC with molecular dynamics (MD) simulations. The important advantage of CDC compared to PBQC in this respect is the fast evaluation of the (time-dependent) site energies.

Up to now the $J(\omega)$ has been extracted [30] from experiments and the same $J(\omega)$ was assumed for all sites in the calculation of the spectra. With the MD simulations we plan to compare the spectral densities of all seven pigments, and we will also study the correlation between modulations of different site energies. We aim at a microscopic model for the correlation radius of the exciton-vibrational coupling, that we introduced as an empirical quantity earlier [30, 92].

4.5 Molecular Dynamics Simulations

Molecular dynamics (MD) simulations are a mighty instrument to investigate molecules with known structures from X-ray crystallography. It is of high interest to inspect whether the X-ray structure is roughly kept or if major changes take place. Also it is very interesting what the timescales of these changes are and if these changes are periodically (as obtained in a normal-mode analysis). Due to rising computer power, it is even possible to treat large molecules of many kDa[5], like the FMO complex, that has a size of 41 kDa and is a rather big complex for a MD simulation.

The idea behind a MD simulation of the FMO complex is not only to show that the X-ray structure is stable. Rather we want to get information about the dynamics of the system, in particular we are interested in the calculation of time dependent site energies. These site energies can be calculated with the CDC method (section 3.3.2) very efficiently for each time step of a MD simulation. With these time dependent site energies we can calculate a correlation function (Eq 3.11), that is connected with the spectral density. Hence we can extract the spectral density from MD simulations (Eq 3.16), independently and compare this result with the spectral density extracted for the B777-complex by Renger & Marcus [30].

The MD simulations performed here, have been done for the whole FMO trimer in a water-box with the program NAMD [123]. The site energies were obtained with the CDC method, processed with Charmm [124], in cooperation with Jorge Numata from the AG Knapp. The calculation of the correlation function and the spectral density was done with a C-program, including *Numerical Recipes* FFT-routines.

Test of the Fourier Transformation

For testing the fast Fourier transformation (FFT) and the calculation of the spectral density following Eq 3.16, we used the correlation function of Renger & Marcus [30], following Eq 3.3 ($J(\omega)$ of Eq 3.2) and calculated the spectral density following $\tilde{C}_{\mathrm{cl}}(\bar{\omega}) = \mathrm{FT}\{C_{\mathrm{cl}}(t)\}$ and Eq 3.16, to compare it with the spectral density of [30], Fig 3.2. In [30] the spectral density was found by fitting fluorescence line narrowing spectra of the B777-complex and then the correlation function was calculated, here it was done in the inverse direction.

As one can see by comparing Fig 4.12 with Fig 3.2, the calculated $C(t)$ and $J(\omega)$ is in agreement with the correlation function and spectral density of [30] for high temperature, but not for low temperature, reflecting that the classical correlation function from Eq 3.12 is only valid for high temperatures.

First Results

A time-trace of the site energy fluctuation (Eq 3.8) of BChl 1 is shown in Fig 4.12 (*right*, top), together with the resulting correlation function (Eq 3.11, *right*, center) and the resulting spectral density (Eqs 3.13, 3.16, *right*, bottom). The short-time behavior of the $C(t)$ and the spectral density from MD is in the same range as the one of Renger & Marcus [30]. Longer time-traces are required for higher resolution.

We can conclude from these first results that it is in principle possible to calculate a reasonable correlation function of site energy fluctuations with MD simulations.

[5] Da (dalton) = unified atomic mass unit (u)

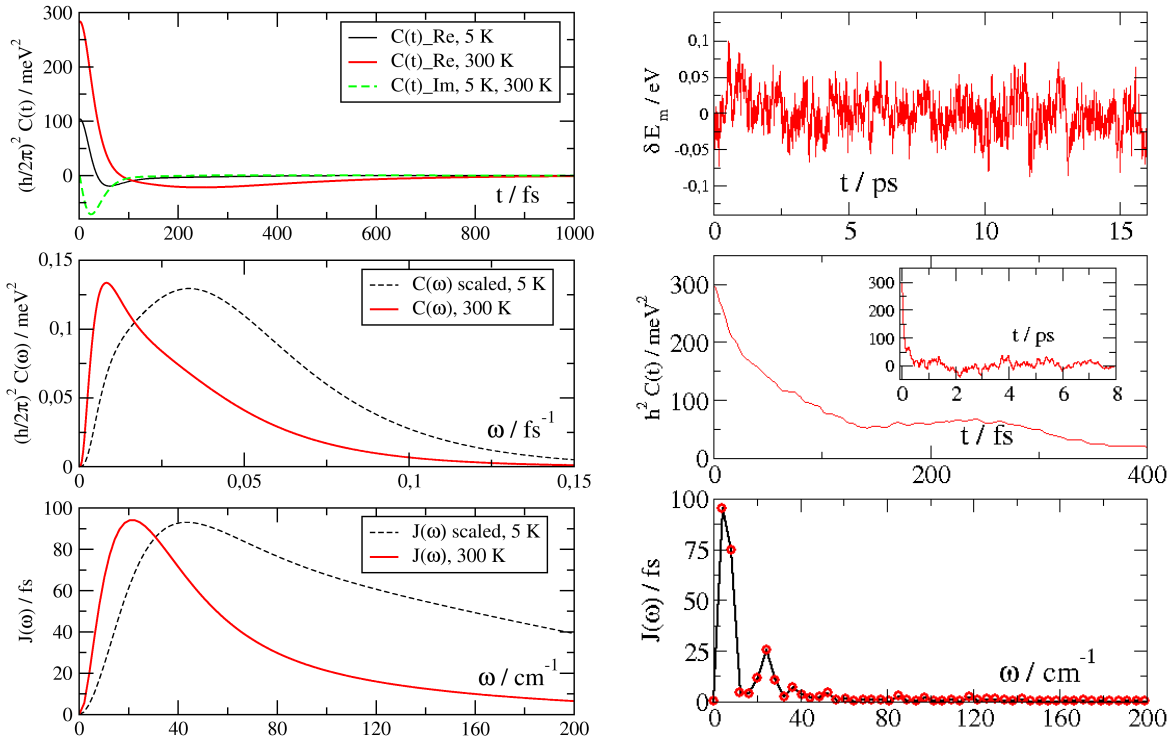

Figure 4.12: *(Left)* Test of the Fourier transform, transforming the $C(t)$ from Eqs 3.2, 3.3 and calculation of the spectral density following, Eq 3.16. Top: correlation function $C(t)$. Center: Fourier transformation $\tilde{C}(\omega)$ of $C(t)$. Bottom: spectral density $J(\omega)$ following from Eq 3.16. *(Right)* Preliminary results for BChl 1. Top: time dependent fluctuation of the site energies, Eq 3.8. Center: Correlation function $C(t)$, Eq 3.11. Bottom: spectral density $J(\omega)$ following from $C(t)$, $\tilde{C}_{\mathrm{cl}}(\bar{\omega}) = \mathrm{FT}\{C_{\mathrm{cl}}(t)\}$, Eq 3.16.

Chapter 5

Application to Photosystem I

Since the 2.5 Å structure of photosystem I from the thermophilic cyanobacterium *Synechococcus elongatus* appeared in 2001 [5], for the first time a high resolution crystal structure of PSI is available. It is a photosynthetic pigment protein complex that binds both reaction center pigments and light harvesting antenna pigments inseparably on the same protein subunit. It is a property of PSI that all primary photosynthetic processes take place within one and the same protein complex. Therefore it is on the one hand possible to study the interplay of light absorption, excitation energy transfer and trapping by electron transfer within one functional unit. On the other hand the size and complexity of PSI is a challenge for theory and it is necessary to apply methods, that have been developed and tested on simple systems first.

The PSI complex of *S. elongatus* consists of 12 subunits. The structure we refer to [5] identifies 96 Chls, 22 carotenoids, two phylloquinones, three iron-sulfur clusters, four lipids, around 200 water molecules and a metal ion. The two largest subunits are termed PsaA and PsaB and bind most of the antenna pigments, as well as the following redox cofactors: special pair P700 (dimer of P_A (Chl*a*) and P_B (Chl*a*')), accessory chlorophyll A_0 (Chl*a*), A_1 (phylloquinone), F_X and the terminal electron acceptors F_A and F_B are both coordinated by the PsaC subunit, which is one of the three stromal side subunits. F_X, F_A, F_B, are $4Fe-4S$ iron sulfur clusters.

In this chapter the methods developed and tested on the FMO complex will be applied to PSI. The main difference is, that it is not appropriate to run a fitting procedure for the absorption, circular dichroism and linear dichroism optical spectra [125] in which the site energies of the 96 Chls of PSI are treated as fit parameters in the same way as for FMO, because the number of parameters is too large. But there are some difference spectra available [126], which can be calculated by only using the reaction center of PSI. The number of pigments determining these difference spectra is only six, hence a fit will give reasonable results.

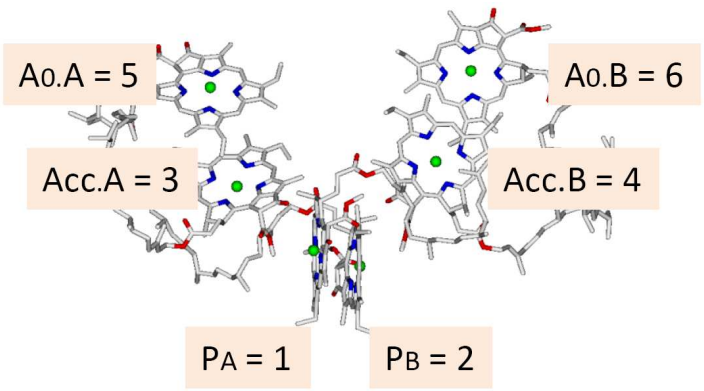

Figure 5.1: The six reaction center pigments of photosystem I with the numbering used here for the couplings.

5.1 Couplings

Here the couplings are calculated for the PSI reaction center of *S. elongatus* , using the methods introduced in section 3.2. The numbering used here is depicted in Fig 5.1.

The excitonic couplings for PSI from *S. elongatus* were calculated in vacuum ($\varepsilon = 1$) and in a dielectric medium ($\varepsilon = 2$), representing the protein and the solvent (*psol* in chapter 4). TrEsp transition monopole charges were used obtained for fully geometry optimized planar Chl*a* (*plan* in chapter 4) [49] which have been rescaled to result in a Chl*a* dipole strength of 21 D^2 as determined by Knox & Spring [18]. For the extended dipole approximation (ED), Eq 3.19, a dipole extend of 8.7 Å, suggested for Chl*a* in PSI by Madjet *et al.* [49], was used. The magnitude of the two partial charges was determined as $\pm 0.11\, e$ such as to result in a dipole moment square of 21 D^2. The same dipole strength was used in the point dipole approximation (PD), Eq 3.18.

The results for these calculations are presented in Table 5.1. In column (1) the couplings for TrEsp charges in vacuum are presented, in column (2) the couplings for TrEsp charges in cavities ($\varepsilon = 1$) surrounded by a dielectric medium ($\varepsilon = 2$). In the right half of the table the results for extended dipole (column 5) and point dipole approximation (column 6) in vacuum are presented. For the special pair coupling (1 – 2) unexpected couplings result: the coupling is tiny in the exact and extended dipole calculation and huge in the point dipole approximation. I will come back to the reason for this discrepancy later and skip the special pair coupling in the following.

A least mean square fit, $V_{mn}^{\mathrm{TrEsp}}(\varepsilon = 2) = f \cdot V_{mn}^{\mathrm{TrEsp}}(\varepsilon = 1)$ is done with the couplings of column (1) and (2) (skipping the special pair coupling), resulting in a factor $f = 0.8$. For better comparison the vacuum TrEsp couplings are multiplied with this factor 0.8 in column (3). A second least mean square fit, $V_{mn}^{\mathrm{TrEsp}}(\varepsilon = 2) = f \cdot V_{mn}^{\mathrm{ED}}(\varepsilon = 1)$ is done with the couplings of column (2) and (5) (also skipping the special pair coupling) resulting in a factor $f = 0.7$. Also the extended dipole couplings are multiplied with this factor f and shown in in column (4). From the comparison of column (2) and (3) one finds that the maximum deviation between these values is 4 cm^{-1} , i.e., the couplings of PSI can be obtained by calculating the TrEsp couplings in vacuum and multiplying them with a factor of 0.8. From the comparison of column (2) and (4) one finds that the maximum deviation between these couplings is 9 cm^{-1} , i.e., the couplings of PSI can even be obtained by a simple extended dipole approximation in vacuum and multiplying them with a factor of 0.7 instead of running relatively complicated and time consuming MEAD [75] calculations. The point dipole approximation is unsuitable for PSI, as one can see by comparing the vacuum couplings of 1 – 3 and 2 – 4, which are undersized in point dipole approximation and 3 – 5 and 4 – 6, which are oversized in point dipole approximation.

Taking into account the different conformations of the acetyl groups of the pigments (*conf*) in the quantum chemical calculation of transition charges, was skipped because the investigations on the FMO complex have shown that there are only minor differences in the results if the different conformations are included. In chapter 4 two slightly different ways to consider the protein, *psol* and *prot*, have been used. The results did not differ significantly, hence we used here the simple method *psol*.

5.1.1 Summary

The PSI couplings, except for the special pair coupling, can either be approximated by Coulomb couplings of extended dipoles, scaled by a factor of 0.7 representing the influence of the dielectric (Eq 3.19) or by the Coulomb couplings between the TrEsp point charges in vacuum, scaled by a factor of 0.8. The point dipole approximation is not appropriate for the RC.

The special pair coupling has only a tiny Coulomb part, the main contribution is of the Dexter type and must be calculated by quantum chemical methods. In principle the other pigments have Dexter type contributions to the couplings, too, but due to calculations of Madjet *et al.* [127], even for those where one can expect larger contributions because of small inter-pigment distances, i.e., Acc.A – A_0A (3 – 5) and Acc.B – A_0B (4 – 6), these are around 10 % of the Coulomb part, i.e. are of minor importance. Due to

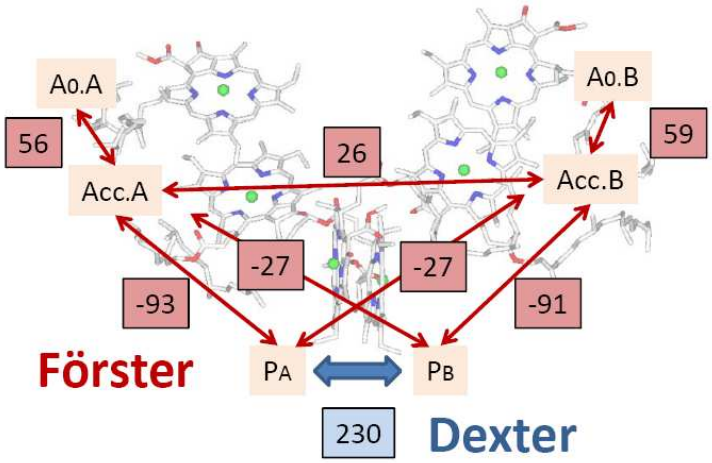

Figure 5.2: The six RC pigments of PSI with the major couplings in wavenumbers (cm^{-1}).

Table 5.1: Excitonic couplings for PSI from *S. elongatus* in units of cm^{-1} obtained with different methods explained in detail in the text. The large couplings are highlighted and the special pair couplings are separated in an own line.

	Excitonic Couplings / cm^{-1}					
Chl	(1) TrEsp $\varepsilon = 1$	(2) TrEsp $\varepsilon = 2$	(3) TrEsp $\varepsilon = 1$ *0.8	(4) ED $f = 0.7$	(5) ED $f = 1$	(6) PD $f = 1$
1 – 2	-5	17	-4	1	2	465
1 – 3	**-119**	**-93**	**-93**	**-93**	**-133**	**-101**
1 – 4	**-35**	**-27**	**-27**	**-21**	**-30**	**-27**
1 – 5	16	9	12	10	15	16
1 – 6	6	5	4	5	7	7
2 – 3	**-35**	**-27**	**-27**	**-21**	**-30**	**-26**
2 – 4	**-115**	**-91**	**-90**	**-87**	**-124**	**-95**
2 – 5	4	4	3	4	6	7
2 – 6	15	9	12	9	13	15
3 – 4	**39**	**26**	**30**	**27**	**38**	**31**
3 – 5	**75**	**56**	**59**	**65**	**93**	**177**
3 – 6	-10	-6	-8	-7	-10	-10
4 – 5	-11	-6	-8	-8	-12	-11
4 – 6	**72**	**59**	**56**	**62**	**89**	**215**
5 – 6	3	1	2	2	3	3

the exponential distance dependence of the Dexter coupling, the excitonic couplings between pigments with larger distances do not contain a significant Dexter contribution.

5.2 Site Energies

In contrast to the site energy determination for the FMO complex, in PSI the number of pigments is too large for a fit of the site energies of all 96 pigments. Nevertheless there exist the attempt of Byrdin *et al.* [125] who did a fit by hand, considering symmetry relations, axial ligands, H-bonding and functional arguments concerning the location of the red pigments, and the attempt of Brüggemann *et al.* [79], who used an genetic algorithm after assigning some chromophores to the red-most states.

Furthermore there exist measurements of Schlodder *et al.* [126, 128] (Fig 5.3) that contain information exclusively about the reaction center pigments. These spectra are triplet minus singlet (T – S) and cation minus neutral ($P^+ - P$) spectra. In the T – S case by optical excitation a triplet state is created on one of the special pair pigments and the absorption spectrum is measured. The triplet carrying pigment

does not absorb in the Q_y region anymore, hence a spectrum of the remaining 95 pigments of PSI is measured. After the decay of the triplet state the so called singlet spectrum is measured, which is identical with the absorption spectrum (Eq 2.16) of all 96 pigments. As one can see in Fig 1.7 (*right*), in the center of PSI are there six pigments that are spatially separated from the outer pigments. These six pigments are strongly coupled, while the coupling to the outer pigments is weak. Hence, it is possible to describe the spectrum as a sum of the spectrum of the outer 90 pigments and the spectrum of the inner 6 pigments. If a triplet state is generated on one of the inner pigments, only the spectrum of the inner pigments changes. As a result in the difference of triplet and singlet spectra the spectrum of the outer pigments vanishes and the difference spectrum is a spectrum of the six RC pigments, in good approximation.

The $P^+ - P$ spectrum is similar to the $T - S$ spectrum: by optical excitation a cation is created on one of the special pair pigments and the absorption spectrum is measured. The pigment with the cation is optically deactivated, the difference to the effect of the triplet state is, that the cation causes electrochromic shifts of the pigment site energies. Again the absorption with and without the cation is measured and in the difference the spectrum of the outer pigments vanishes. That means that we can determine the site energies of the six RC pigments by fitting $T - S$ and $P^+ - P$ spectra.

5.2.1 Reaction Center Site Energies from Fit of Optical Spectra

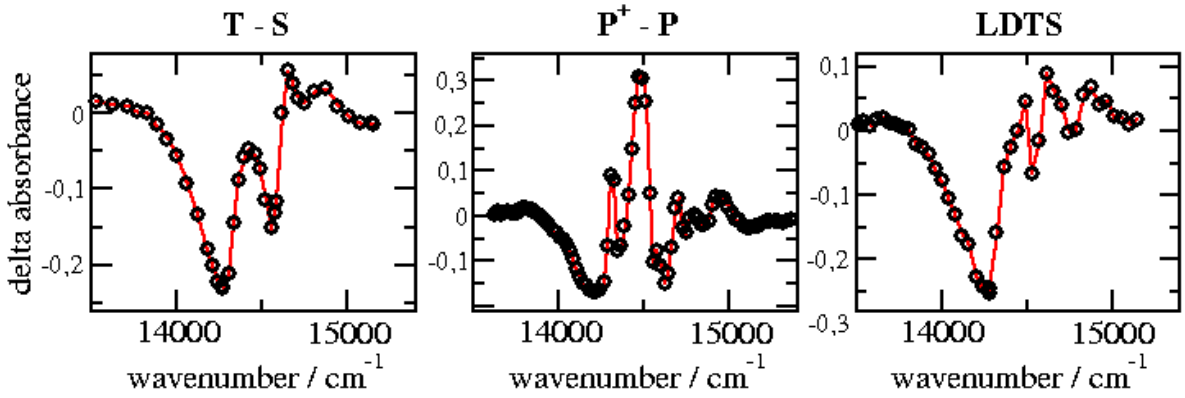

Figure 5.3: Difference spectra of PSI measured by Schlodder *et al.* [126]: triplet minus singlet ($T - S$), cation minus neutral ($P^+ - P$) and linear dichroism of triplet minus singlet, LDTS, at a temperature of 5 K.

The fits presented here are simultaneous fits of $T - S$ and $P^+ - P$ spectra, where the excitonic couplings were calculated in extended dipole approximation with a transition dipole moment of 4.58 D [18] and a dipole extension of 8.7 Å [49] together with a scaling factor of 0.7 for all but the special pair coupling. The special pair coupling was varied between 10 cm^{-1} and 280 cm^{-1} for different fits, because the Coulomb coupling of the special pair is very small, but Madjet *et al.* [127] calculated a Dexter coupling of 230 cm^{-1}, including a small Coulomb contribution.

I note that the spectra are nearly identical, due to the spatial symmetry, if the triplet position, the cation position and all site energies (and inhomogeneous broadenings) are interchanged between the two branches A and B. Therefore the fits were performed only assuming triplet state localization on P_A and cation localization on P_B. The triplet and the cation are located on the special pair, but not on the same pigment (section 5.2.5).

From the test of the genetic algorithm (section 3.3.1, *Test of the Algorithm for PS1*) we have an estimate of the error of the fit result: $\Delta E_m \geq 10$ cm^{-1} and $\Delta\text{fwhm} \geq 30$ cm^{-1}. As an additional test of the fit results, the linear dichroism of the triplet minus singlet spectrum (LDTS) is calculated with the site energies and inhomogeneous broadenings obtained from the fit of $T - S$ and $P^+ - P$.

It was tried to fit the RC spectra only with the six site energies as fit parameters and with fixed and

Table 5.2: Fitness values for fits of T – S and P$^+$ – P spectra for different special pair couplings V_{sp} in units of cm^{-1}. The maximum value is highlighted. The fitness value is defined as explained in section 3.3.1.

V_{sp} / cm^{-1}	10	110	150	180	210	220	**230**	240	260	280
Fitness	0.121	0.126	0.130	0.151	0.151	0.160	**0.167**	0.152	0.163	0.161

identical inhomogeneous broadenings (analog to FMO, chapter 4). It was not possible to find any satisfying result. Hence I tried to run the fit with additional 6 inhomogeneous broadenings as fit parameters, that were allowed to vary between 100 and 300 cm^{-1}. For large enough special pair couplings it was possible to find satisfactory solutions. Interestingly the fitness value of the resulting set of site energies and inhomogeneous broadenings has a maximum for a special pair coupling of 230 cm^{-1} (Tab 5.2), i.e. the best fit is obtained for the special pair coupling also calculated by Madjet *et al.* [127] directly from the structural data by an ab initio method. As one can see in Fig 5.4, the fit with the small Coulomb coupling for the special pair (10 cm^{-1}, blue) does not fit at all, while the result for a special pair coupling of 230 cm^{-1} fits, also for the LDTS-spectrum (Fig 5.4 and 5.5, red), at least qualitatively.

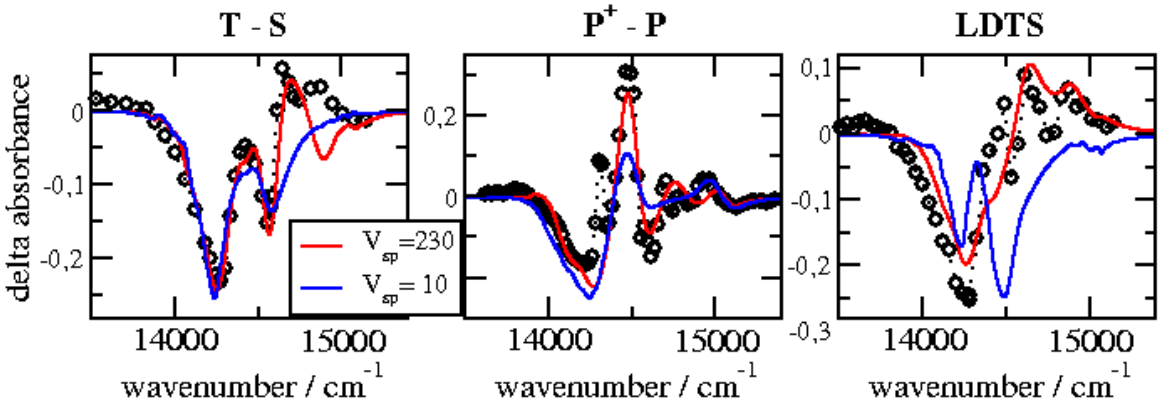

Figure 5.4: Fit result for special pair couplings of 10 cm^{-1} (blue) and 230 cm^{-1} (red) of the T – S, P$^+$ – P and LDTS spectra in comparison to experimental spectra [126, 128] .

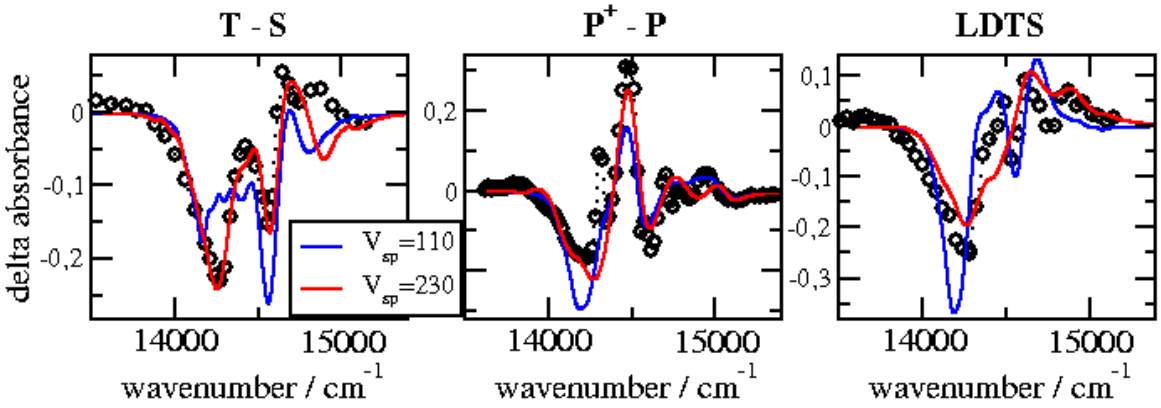

Figure 5.5: Fit result for special pair couplings of 110 cm^{-1} (blue) and 230 cm^{-1} (red) of the T – S, P$^+$ – P and LDTS spectra in comparison to experimental spectra [126, 128] .

Table 5.3: Site energies for PSI from *S. elongatus* in units of cm^{-1} obtained from fit of T – S and $P^+ - P$ spectra with a genetic algorithm, using different special pair couplings V_{sp}. The highlighted values are those obtained for maximum fitness value.

V_{sp}	P_A	P_B	Acc.A	Acc.B	A_0A	A_0B
10	14495	14231	14342	14448	14582	15113
210	14680	14500	14770	14440	14730	14170
220	14700	14480	14690	14410	15100	14140
230	**14730**	**14480**	**14690**	**14430**	**15140**	**14160**
240	14720	14510	14740	14430	14710	14150
260	14740	14490	14760	14380	14690	14130
280	14740	14510	14750	14370	14700	14160

Table 5.4: Inhomogeneous broadenings for PSI from *S. elongatus* in units of cm^{-1} obtained from fit of T – S and $P^+ - P$ spectra with a genetic algorithm, using different special pair couplings V_{sp}. The highlighted values are those obtained for maximum fitness value.

V_{sp}	P_A	P_B	Acc.A	Acc.B	A_0A	A_0B
10	250	250	150	150	150	150
210	250	290	160	190	140	180
220	200	290	100	220	100	150
230	**110**	**290**	**100**	**180**	**100**	**160**
240	190	290	100	180	160	160
260	100	290	130	250	100	160
280	110	280	120	290	120	170

5.2.2 Electrochromic Site Energy Shifts

The site energies presented in this section are calculated with the CDC method (section 3.3.2), following Eq 3.34 and Eq 3.36. The site energies are calculated for all 96 pigments of the PSI complex from *S. elongatus* with the amino acids of the protein in standard protonation state. The spectral width suggested values $\varepsilon_{\text{eff}} = 1.8$, and $E_0 = 14450$ cm^{-1} in Eq 3.34 respectively Eq 3.36. In Tab 5.5 only the RC site energies are shown, together with the site energies from the fit[1], for comparison. The site energies for all 96 Chls are shown in Table 5.7. If one compares the CDC site energies of the RC (Table 5.5) with each other, one finds that the values for Acc.A and Acc.B as well as A_0A and A_0B are nearly equal, due to the structural symmetry. For the special pair the site energies of P_A is significantly smaller than P_B, according to the broken structural symmetry of the special pair: in contrast to P_B, P_A has an H-bond, which causes a redshift. Furthermore one finds that the CDC site energies from the A-branch are very close to the site energies from the fit, while all CDC site energies from the B-branch are blue shifted, compared to the site energies from the fit. In Table 5.6 the fitted inhomogeneous broadenings, are shown. A remarkable result is that the inhomogeneous broadening is much larger for P_B than for all other pigments.

Conclusions

From the comparison of site energies from the free fit and the CDC method, it is evident that not all site energies from the free fit are reasonable. On the one hand due to the spatial symmetry it is expected that the site energies for Acc.A and Acc.B are nearly equal, as well as the site energies of A_0A and A_0B. The special pair is not symmetric, because there exist an H-bond to P_A but not to P_B. Hence we expect different site energies for P_A and P_B. Moreover it is expected that the energy sink is on the primary electron donor (special pair or accessory Chl), otherwise the energy flux would not be efficient (see Fig

[1] *Free Fit* in Table 5.5 and in the following, because all site energies were allowed to vary independently from each other.

Table 5.5: Site energies in cm^{-1} from free fit and fits with boundary conditions (BC) of $T-S$ and P^+-P spectra, and site energies from CDC-method. BC Fit 6 respectively 9 means fit with BC only for the RC respectively for the RC and the 3 additional pigments. All fits were performed with a special pair coupling of 230 cm^{-1}.

	P_A	P_B	Acc.A	Acc.B	A_0A	A_0B	1239	1237	1238
Free Fit	14730	14480	14690	14430	15140	14160	-	-	-
CDC	14680	15010	14810	14800	15190	15270	14590	15080	15080
BC Fit 6	14740	14420	14780	14780	14690	14690	-	-	-
BC Fit 9	14730	14420	14820	14820	14670	14670	14870	14840	14930

Table 5.6: Inhomogeneous broadenings in cm^{-1} from free fit and fits with boundary conditions (BC) of $T-S$ and P^+-P spectra. BC Fit 6 respectively 9 means fit with BC only for the RC respectively for the RC and the 3 additional pigments. All fits performed with a special pair coupling of 230 cm^{-1}.

	P_A	P_B	Acc.A	Acc.B	A_0A	A_0B	1239	1237	1238
Free Fit	110	290	100	180	100	160	-	-	-
BC Fit 6	110	290	190	190	110	110	-	-	-
BC Fit 9	110	390	190	190	90	90	150	160	190

4.10). This is not the case for the site energies from free fit, there the pigment with the lowest site energy is A_0B.

5.2.3 Fit of RC Site Energies with Boundary Conditions

Because of the former conclusions we decided to run a new fit with the boundary conditions that the site energy of Acc.A equals the site energy of Acc.B and the site energy of A_0A equals the site energy of A_0B, while P_A and P_B can vary freely. The inhomogeneous broadening was allowed to vary between 60 cm^{-1} and 400 cm^{-1} (that yielded better results than the interval $100-300$ cm^{-1}). As one can see in Table 5.5, the resulting site energies for the special pair are very similar to those of the free fit, and as in the free fit, P_A has a higher site energy than P_B. More convincing at these new site energies is, that the lowest site energy is in the special pair, namely on P_B, and not on A_0B as for the free fit. As one can see in Fig 5.6 (red), the resulting spectra do fit not as well as for the free fit, but they fit in a reasonable way.

In the experimental spectra there are more peaks than we can reproduce by our fit with 6 pigments. Therefore we tried to increase the quality of the fit by including 3 more pigments (1237, 1238, 1239) which are coupled relatively strongly to the RC pigments (section 5.2.6, Fig 5.11). As one can see in Table 5.5, the site energies of the six RC pigments resulting from the 9-pigments-BC-fit are very similar to those obtained from the 6-pigments-BC-fit. In Fig 5.6, one can see that the result for nine pigments (blue) fits slightly better to the experiment than the result for six pigments (red).

5.2.4 Delocalization of Excitons

The delocalization of excitons in the RC is investigated by the disorder averaged exciton states pigment distribution function $d_m(\omega)$, Eq 2.13, that describes the contribution of a given pigment m to the different exciton states [32]. In Fig 5.7 the function $d_m(\omega)$ for the six pigments[2] of the RC of *S. elongatus* is compared with the density of exciton states $d_M(\omega)$, Eq 2.14. In the calculations, the site energies obtained from the genetic fit with boundary conditions (Table 5.5, BC Fit 6) were used. It is evident, that the excited states of the pigments contribute to more than one exciton state. P_A and P_B form an excitonic hetero dimer and dominate the lowest and the highest exciton level. Acc.A and Acc.B as well as A_0A and A_0B form also dimers, what seems to be astonishing in the case of A_0A and A_0B, because these pigments

[2]The result for nine pigments did not include additional information, but was not so clearly as for six pigments.

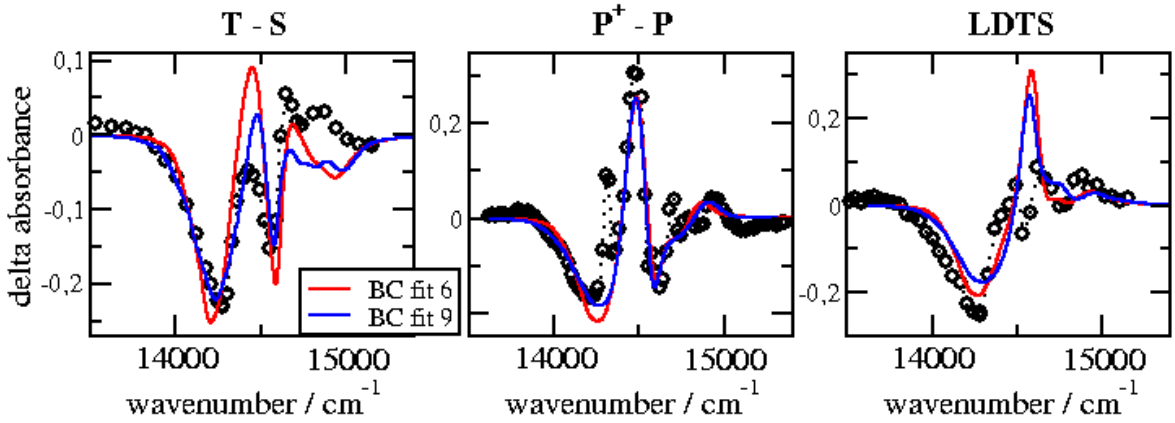

Figure 5.6: Fit result of BC fit for 6 (red) and 9 (blue) pigments (Table 5.5) obtained for a special pair couplings of 230 cm^{-1} in comparison to experimental $T-S$, P^+-P and LDTS spectra [126, 128].

are coupled weakly to each other (Fig 5.2), but the coupling is conveyed over the other pigments. Exciton level 5 is mainly determined by Acc.B, and exciton levels 2 and 3 are mainly determined by A_0A and A_0B, but all in all one has to say that the exciton levels $2-5$ are determined of the four non-special pair pigments. Although the reaction center pigments are more dimer like, P_A has a significant contribution to exciton levels 3 and 4. Altogether, the delocalization is more pronounced compared to FMO. The most important conclusion is, that the lowest exciton level is mainly determined by P_B, i.e. P_B represents the energy sink of the RC.

5.2.5 Localization of the Triplet State

First we notice that both, the triplet state and the cation are located on the two special pair pigments. It hast been concluded from EPR/ENDOR experiments [129] that the cation is mainly localized of one of the special pair pigments. For the triplet state there is some evidence from virtually identical zero-field-splitting parameters of ^{3}P700 and of monomeric ^{3}Chl*a* or ^{3}Chl*a*′ in organic solvents at low temperature that it is localized mainly on one chlorophyll [130]. Additionally, the orientation dependence of the triplet state showed that the plane of the triplet carrying pigment is oriented perpendicular to the membrane [131], i.e. the triplet state is localized on P_A or P_B.

Under that condition, four combinations are possible: (i) both the triplet state and the cation on P_A, (ii) both on P_B, (iii) triplet on P_A and cation on P_B and (iv) cation on P_A and triplet on P_B. We conclude that the triplet state and the cation are located on different special pair pigments from the following considerations. The effect of the triplet state and the cation is in principle the same: the respective pigment does not absorb in the Q_y region and hence only a spectrum of the five remaining pigments results (in good approximation). The difference between the effect of triplet and cation is, that in the case of a cation additionally an electrochromic shift results. Because this shift is rather small (see below), the $T-S$ and P^+-P spectra are rather similar, if the cation and the triplet are located on the same pigment. The P^+-P spectrum is calculated with and without including electrochromic shifts, for comparison. As one can see in Fig 5.8, the P^+-P spectrum obtained without including electrochromic shifts still is similar to the experimental P^+-P spectrum, while it differs strongly from the $T-S$ spectrum. From this result we conclude that the large difference between the experimental P^+-P and $T-S$ spectra is not due to electrochromic effects. Hence we can conclude that the triplet state and the cation are located on different special pair pigments.

Due to the fact that the difference spectra look like nearly identical for interchanged site energies and triplet/cation localization of A- and B-branch, mutation experiments are needed to distinguish whether

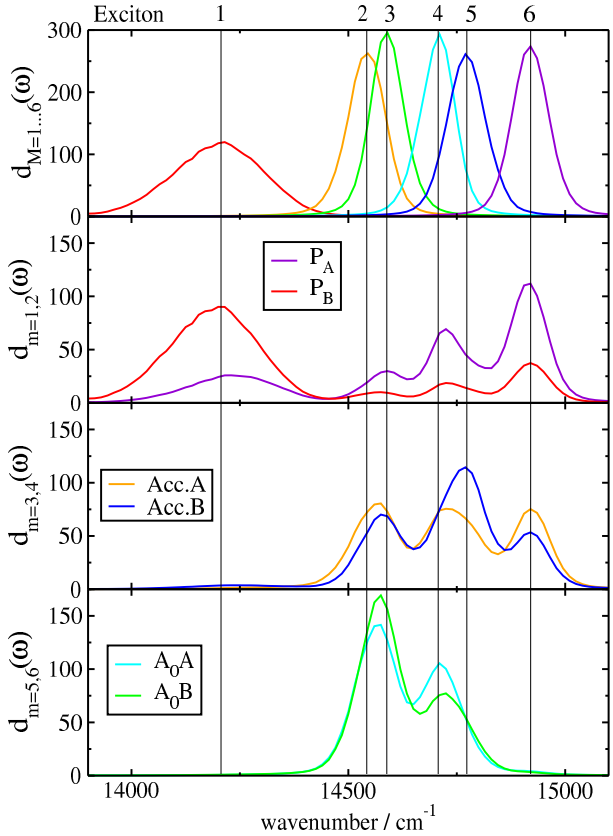

Figure 5.7: The top part contains the disorder averaged density of exciton states $d_M(\omega)$ defined in Eq 2.14, and the lower parts the exciton states pigment distribution functions $d_m(\omega)$ in Eq 2.13.

the triplet state is located on P_A or P_B. Suitable experiments on PSI from *Chlamydomonas reinhardtii* have been done by Witt *et al.* [128]: T – S spectra have been measured for the wilde type of *C. reinhardtii* and for a mutant with removed H-bond[3] to P_A, what causes a blue-shift of the site energy of that pigment. These mutation spectra enable us to decide whether the triplet is located on P_A or P_B.

For that we calculate a T – S spectrum with a suitable set of site energies from fit, with triplet localized on P_A, this is the simulated wild type spectrum (Fig 5.9, *left*, black). For the same set of site energies but blue-shifted P_A site energy we calculate a T – S spectrum again, which is the mutant spectrum (Fig 5.9 *left*, red). To simulate the mutation, we have to blue-shift the site energy of P_A by a reasonable value, we used 200 cm^{-1}. For the calculation with the triplet on P_B we have to interchange the site energies of A- and B-branch (without blue-shift). The simulated wild type T – S spectrum is obtained by these site energies (Fig 5.9, *right*, black). The mutant T – S spectrum is obtained by blue-shifting the new P_A site energy (Fig 5.9, *right*, red).

The resulting spectra are compared to the experimental spectra in Fig 5.9. The special pair coupling used here was 230 cm^{-1} and the site energies as well as the inhomogeneous broadenings from *S. elongatus* (Tab 5.5, Free Fit) were used. The fact that we use the structure, couplings, site energies and inhomogeneous broadenings from *S. elongatus* to simulate the spectra of a different species (*C. reinhardtii*), results in calculated spectra with a higher deviation from the experimental data than for *S. elongatus*. Nevertheless, from comparing the experimental spectra with the simulations (Fig 5.9) assuming triplet localization on P_A (*left*) or on P_B (*right*), it is evident that the triplet is localized on P_A. Even the blue-shift of the red-most peak can be reproduced by the simulation with triplet on P_A (green arrows) although the simulated shift is smaller than the measured. Furthermore the trend of the intensity relation

[3] A present hydrogen bond shifts the local transition energy of a pigment to the red (explained in section 4.4, *Discussion of Molecular Details*), hence a removed H-bond shifts it in comparison to the present H-bond to the blue.

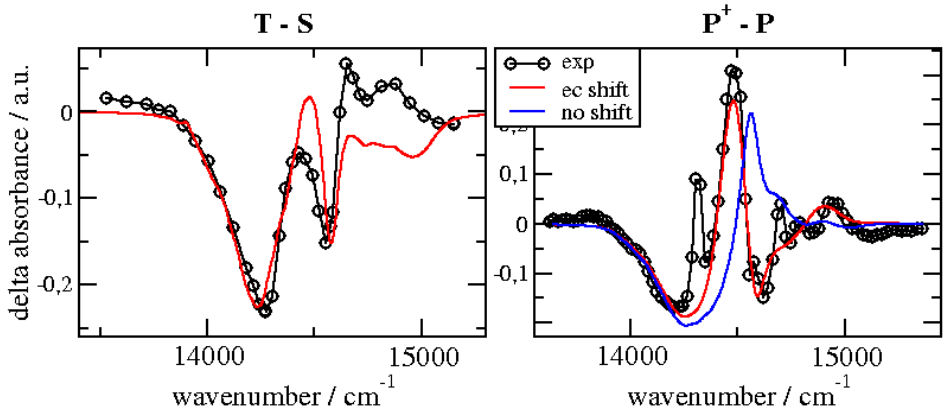

Figure 5.8: Simulated $T-S$ spectra assuming triplet localized on P_A and P^+-P spectra assuming cation localized on P_B, using the site energies from Table 5.5 (BC Fit 9) in comparison to experimental data [126, 128].

between the 14250 cm^{-1} and 14550 cm^{-1} peaks is reproduced by the simulation with triplet on P_A.

From that we can draw the conclusion that the cation is located on P_B, in accordance with ENDOR studies of $p700^+$ which led to the conclusion that at least 85 % of the spin density is localized on P_B [129].

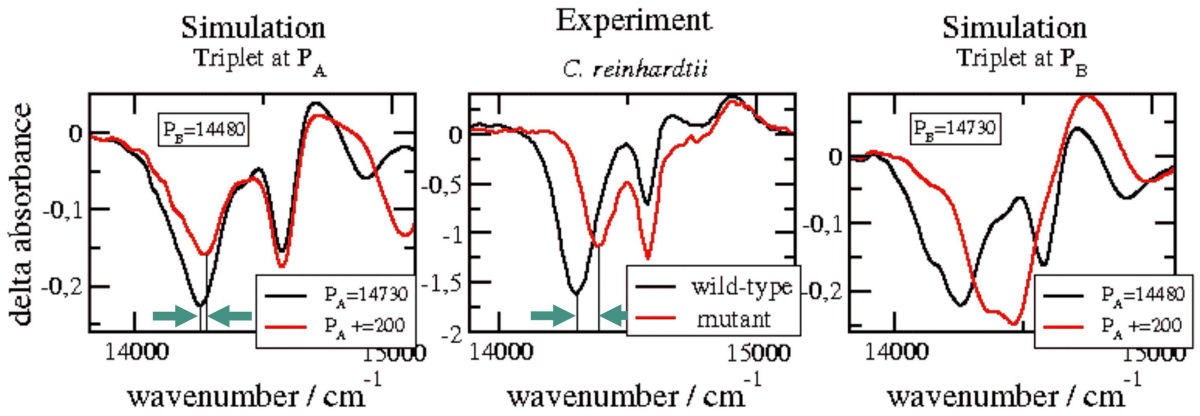

Figure 5.9: *(Left)* Simulated $T-S$ spectra with triplet localized on P_A. Wild type (black), mutant (red). *(Center)* Experimental $T-S$ spectra of the PSI complex from *C. reinhardtii* for the wilde type (black) and a mutant with removed H-bond to P_A (red), measured by Witt *et al.* [128]. *(Right)* Simulated $T-S$ spectra with triplet localized on P_B. Wild type (black), mutant (red).

5.2.6 Linear Optical Spectra of PSI

In the following, spectra of whole PSI complexes are calculated using the 96 site energies, obtained with the CDC-method. If these spectra are calculated as described in chapter 2, for each cycle of the Monte Carlo method a matrix with dimension 96×96 has to be diagonalized. Because not all of the 96 pigments have a significant excitonic coupling with all other 95 pigments, it is reasonable to determine *domains*. That has also the advantage that the dynamic localization is implicitly included by the use of domains. Up to now there is no theory for an explicit treatment of the dynamic localization through the protein vibration, hence the use of all 96 pigments as a single domain results in a stronger delocalization of excitation energy than we expect to be realistic.

The domains are defined to contain pigments with couplings larger than a certain cutoff coupling

strength (here 35 cm^{-1}), that is chosen in the same order as the reorganization energy of the local optical excitations of the pigments to take into account dynamical localization effects in an effective way. For a 35 cm^{-1} cutoff we find 21 domains. The largest domain contains 27 pigments, the second largest 26 pigments and the third largest domain is the domain with the RC, that contains 9 pigments, the former six RC pigments and three additional pigments (Fig 5.11). Eleven domains consist of single pigments.

For the fit of $T-S$ and P^+-P spectra we first used the six RC pigments, but now it turns out that we cannot find a cutoff that results in a domain that contains exactly the six RC molecules. Interestingly the three antenna pigments that belong to the RC domain are located on the B-side of the RC. This result reflects a certain asymmetry in the organization of the antenna pigments around the RC. The maximum coupling of the three antenna pigments on the B-side (1237, 1238, 1239) occurs between 1239 and 1023 (A_0B), and amounts 65 cm^{-1}, while the maximum coupling of the three antenna pigments on the A-side (1138, 1139, 1140) occurs between 1140 and 1013 (A_0A) with a value of around 31 cm^{-1}.

After determination of the domains, we can calculate the spectrum as a sum of the 21 domain spectra, i.e., we have a maximum matrix of dimension 27×27 for diagonalization. This procedure decreases the computation time by a factor of $(96/27)^3 \approx 45$. The parameters of the simulations are: equal inhomogeneous broadenings of 300 cm^{-1} (fwhm) for all pigments, a temperature of 295 K, a special pair coupling of 230 cm^{-1}, a screening factor of 0.8[4] and 100 Monte Carlo steps for each spectrum (due to the high temperature and the large inhomogeneous broadenings more Monte Carlo steps do not improve the spectra).

In Fig 5.10 the experimental LD, CD and absorption spectra of Byrdin *et al.* [125] (*left* and *right*), together with simulated spectra are shown. In the left part of Fig 5.10, the spectra calculated with the site energies obtained with the CDC method (Table 5.7, red) are shown. Alternatively the spectra were calculated using the nine site energies fitted for the RC domain (Table 5.5) and the remaining 87 site energies from Table 5.7 (blue). In the right part of Fig 5.10, the spectra calculated by Yin *et al.* [132] with site energies from two quantum chemical methods are shown, for comparison. Our CD and absorption spectra fit very well with the experimental ones. The deviation of the calculation from the experiment is much larger for the LD spectrum, but still there is some similarity, including the position of the main peak and the fact that the spectrum is mainly positive. In comparison with the simulation of Yin *et al.* [132], our LD spectrum fits much better. In their calculations two positive main peaks are obtained for the INDO method, one on the low energy side and one the high energy side of the experimental peak, and a very large negative peak. With the CAM – B3LYP method they obtain a very large negative peak, and a slightly red shifted main peak.

5.3 Discussion

In this chapter the excitonic couplings of the photosystem I reaction center from *S. elongatus* have been calculated using TrEsp transition monopoles [49] and considering the dielectric medium by solving the Poisson equation numerically [75]. It was shown that the couplings can also be calculated by extended dipole approximation and representing the influence of the environment by an effective factor of 0.7, extracted from the comparison between the exact solution and the extended dipole approximation. The extended dipole approximation together with the factor of 0.7 is valid for all RC pigments but the special pair pigment. From fits of difference spectra, $T-S$ and P^+-P, we found the same special pair coupling of 230 cm^{-1} which was calculated by Madjet *et al.* [127] with a quantum chemical method. The extended dipole approximation yields wrong results for that coupling, because the mayor part of it is of the Dexter type and only a small contribution is of the Coulomb type and our method is only capable to consider the Coulomb part.

It was possible to find a set of site energies for the RC pigments, that is able to reproduce the spectra

[4]The couplings have been calculated by the domain-program using TrEsp charges. Hence the factor $f = 0.8$, determined for this case in section 5.1 has been used.

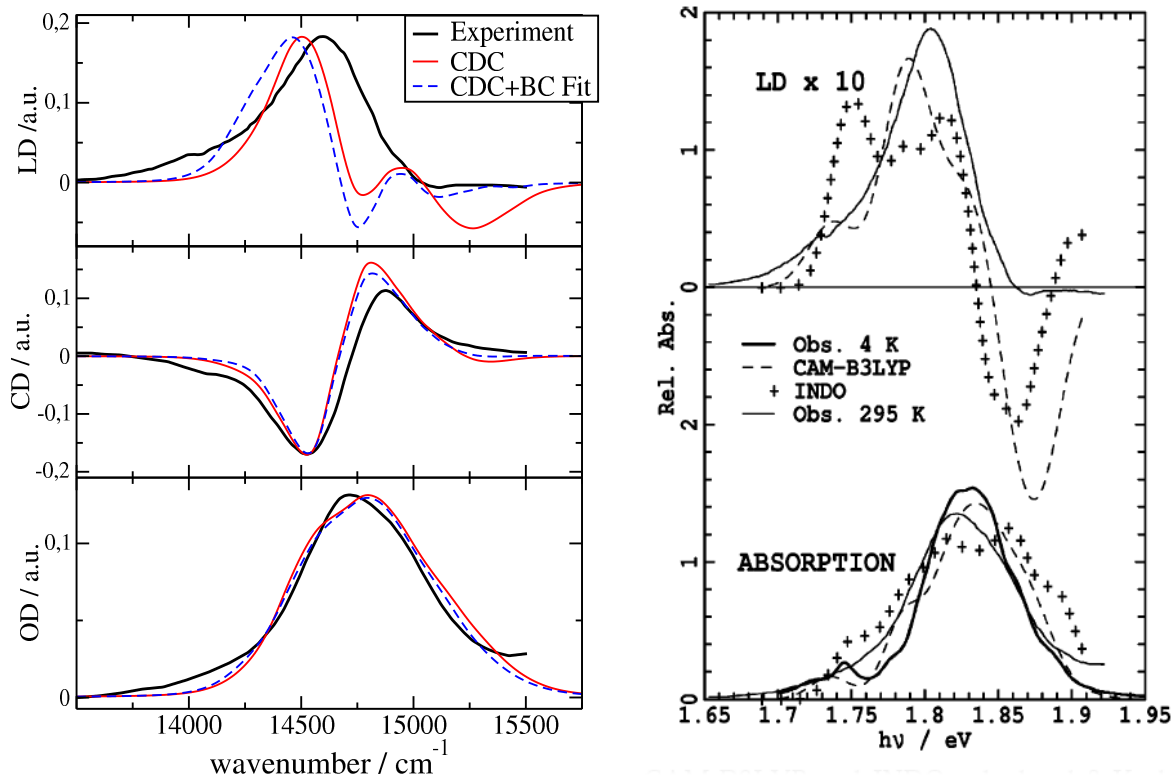

Figure 5.10: (*Left*) Spectra simulated with site energies from CDC method (Table 5.7), and site energies of RC domain from fit (Table 5.5) combined with site energies of antenna from CDC method (Table 5.7). (*Right*) Simulated spectra from the literature for site energies obtained with two different quantum chemical methods (Yin *et al.* [132]). The calculated spectra in the left and right half are compared with experimental data [125].

sufficiently and to be reasonable in terms of energy flux. This set of site energies was found by a fit with boundary conditions, taking into account the spatial symmetry of the system. With this set of site energies the delocalization of the excitation energy over the RC pigments was calculated. It turned out that the lowest exciton level is mainly determined by P_B, i.e., this pigment acts as an energy sink. Interestingly, P_A which has a red-shifting H-bond is not the energy sink, but P_B, which has no H-bond. This might be due to exchange effects of the wave function, which can not be considered in the CDC method.

With the CDC method site energies of the PSI complex have been calculated. These site energies have been used to calculate optical spectra of the PSI complex. Alternatively the fitted values were applied for the 6 RC and the 3 additionally pigments (Fig 5.11) and combined with the CDC values for the remaining 87 pigments. The absorption and CD spectra where reproduced very well, while the LD spectrum did not fit as well as OD and CD, but much better than the spectra obtained from quantum chemical calculations by Yin *et al.* [132]. The agreement between the spectra calculated with CDC site energies and the experiment might improve if it will be possible to identify the red Chls and to consider them in the calculation of the spectra.

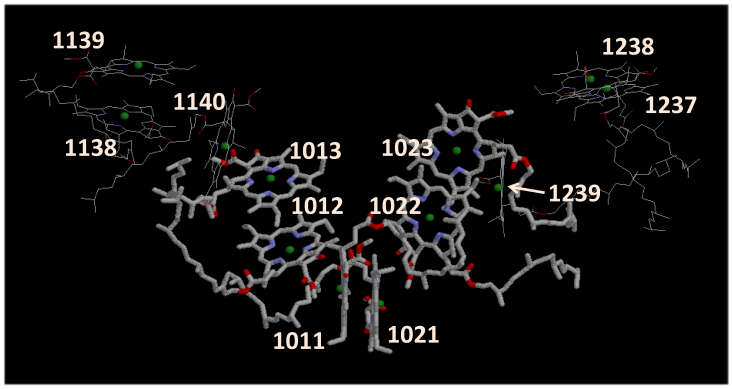

Figure 5.11: RC complex (1011=P_A, 1012=Acc.A, 1013=A_0A, 1021=P_B, 1022=Acc.B, 1023=A_0B) with six additional excitonically coupled antenna pigments (A-side: 1138, 1139, 1140. B-side: 1237, 1238, 1239). The three antenna pigments of the B-side belong to the RC domain. The numbering is according to the protein data base numbering of the file 1JB0.pdb.

Table 5.7: Site energies (SE) of 96 Chls of PSI from *S. elongatus* in cm^{-1}, determined with the CDC method. Numbering according to the pdb nomenclature (1JB0.pdb).

No.	SE	No.	SE	No.	SE	No.	SE	No.	SE	No.	SE
1011	14680	1111	14620	1127	14580	1203	14810	1219	14500	1235	14670
1021	15010	1112	14840	1128	15170	1204	14500	1220	14570	1236	14780
1012	14810	1113	14670	1129	14940	1205	14300	1221	14840	1237	15200
1022	14800	1114	14970	1130	15230	1206	14960	1222	14700	1238	14500
1013	15190	1115	14950	1131	15150	1207	14760	1223	15090	1239	14920
1023	15270	1116	15110	1132	14570	1208	14760	1224	14670	1301	14990
1101	15080	1117	14580	1133	14490	1209	15120	1225	14710	1302	14760
1102	15080	1118	14800	1134	14780	1210	14790	1226	14870	1303	14720
1103	14590	1119	14610	1135	14960	1211	14930	1227	14790	1401	14790
1104	14990	1120	14710	1136	14720	1212	14690	1228	15170	1402	14970
1105	14750	1121	14930	1137	14710	1213	14970	1229	14940	1501	14750
1106	14420	1122	14690	1138	14790	1214	14990	1230	14610	1502	14940
1107	15060	1123	14820	1139	14480	1215	14620	1231	14540	1503	14880
1108	14890	1124	14780	1140	15040	1216	14540	1232	14830	1601	15300
1109	14990	1125	15140	1201	14950	1217	14730	1233	15000	1701	14780
1110	14970	1126	14730	1202	14520	1218	14560	1234	14750	1801	14770

Chapter 6

Summary

Since the first high resolution X-ray crystal structure of a pigment-protein-complex (FMO complex [2]) has been determined more than 30 years ago, numerous publications tried to explain the optical low-temperature spectra of this complex. The X-ray crystal structure has been used to calculate the excitonic couplings of the pigments, while their local transition energies (site energies) have been treated as fit parameters. The main reason why it took over 20 years to find a satisfying description of the different linear spectra and a unique set of site energies, was the usage of an oversized dipole strength (up to 51.6 D^2 [89]) for the optical transition dipole moment of the pigments. Aartsma and coworkers [42, 43, 86] found that using a smaller effective dipole strength (28.7 D^2) allows one to significantly improve the description of optical spectra. They treated the dipole strength as a fit parameter. Here, for the first time, the effective dipole strength has been calculated directly.

For that purpose we have developed a theory of excitonic couplings in dielectric media using a perturbative treatment of the pigment-solvent interaction. With this theory, it is possible to calculate the excitonic couplings in the dielectric medium by solving the Poisson equation numerically. We calculated the excitonic couplings for two different pigment-protein-complexes (FMO and PSI) with an existing software [75]. Thereby we used the values of Knox & Spring [18][1] for the transition dipoles of BChl*a*/Chl*a* and the TrEsp charges of Madjet *et al.* [49][2] for the atomic transition charges. We found that the effective dipole strength is nearly equal to the value fitted before in [42, 43, 86], namely 29.7 D^2 for BChl*a*. We also pointed out that the usage of the point dipole approximation for the FMO complex, respectively the extended dipole approximation for the PSI complex, are suitable for the calculation of the excitonic couplings, if the factors, $f = 0.8$ for FMO and $f = 0.7$ for PSI, are considered. These factors suggested here, describe the influence of the dielectric (shielding and local field effects) in an effective way. These factors are not universally valid (see below), but are valid for the large couplings (the small couplings are not relevant for the spectra) in the geometries of FMO and the PSI reaction center.

With the methodology of coupling calculation, a systematic study of the distance and angle dependence of couplings in a dielectric medium has been performed. We found the relation $V_{\text{med}} \approx V_{\text{vac}}^{\text{ED}}(d_0) - f \cdot V_{\text{vac}}^{\text{ED}}(d_1)$, where f is distance and angle dependent. $V_{\text{vac}}^{\text{ED}}(d_1)$ is the vacuum coupling of an extended dipole of extension $d_1 = 10$ Å, and $V_{\text{vac}}^{\text{ED}}(d_0)$ is the vacuum coupling of an extended dipole of extension $d_0 = 8.8$ Å. The advantage of this method is, that it is not necessary to solve the Poisson equation numerically. Nevertheless the couplings can be determined with high accuracy. The parameters f and d_0 have to be recalculated for each pigment type. The parameters given here are valid for BChl*a*.

The exponential distance dependence of the ratio between the coupling in medium and the coupling in vacuum, recently published by Scholes *et al.* [71], has been confirmed only for specific geometries of the interacting molecules.

[1] An analysis of the dipole strength of BChl*a* in 15 different solvents yielded a vacuum dipole strength of 37.1 D^2.

[2] The TrEsp-method determines atomic transition charges by fitting the electrostatic potential of point charges to the electrostatic potential of the quantum chemical transition densities.

For a long time the theory used for the calculation of spectra was based on the calculation of stick-spectra, resulting from the exciton eigenstates and their convolution with Gauß functions [43,86,133] that take into account the pigment-protein-coupling in an effective way. In the present work a theory of higher complexity [30] was applied. It considers the Hamiltonian of the complete pigment-protein-complex $H_{\text{ppc}} = H_{\text{ex}} + H_{\text{ex-vib}} + H_{\text{vib}}$, composed of the excitonic and the vibrational part, and the contribution of exciton-vibrational coupling. Previously, often only the excitonic part was included. Finally the pigment-protein-complex Hamiltonian used here yields (i) lifetime broadening, (ii) vibrational sidebands and (iii) an energy shift of the transitions compared to the transition energy following from the exciton Hamiltonian.

In the framework of this thesis two basically different methods for the calculation of site energies were developed: A genetic algorithm, which is capable to fit one or several spectra (and their derivatives) simultaneously to the respective experimental spectra. Thereby the site energies are the fit parameters. During the application to PSI it turned out that it is necessary to treat the inhomogeneous broadening of each pigment as additional fit parameter.

The other method (CDC) is based on a direct calculation of the charge density interaction of ground and excited states of the pigments with the protein. Both methods are based on the X-ray crystal structure. The fit needs only the positions of the pigments (respectively of the Nitrogen atoms $N_A - N_D$) for the calculation of the excitonic couplings. In the CDC method the atomic structure of the complete pigment-protein-complex is considered for a direct calculation of site energies.

It is of large benefit to have two independent methods for the calculation of the site energies, because it gives corresponding results a high relevance, if they are achieved in two independent ways. Furthermore the CDC method allows to draw conclusions about the structure-function relationships of the pigment-protein-complex. Contributions of single amino acids and their side chains, hydrogen bonds, as well as the influence of the protein backbone, respectively parts of it, have been calculated.

A more accurate method, the Poisson-Boltzmann Quantum Chemical (PBQC) method [26] combines quantum chemical methods on BChl*a* in vacuum with electrostatic calculations for the whole pigment-protein-complex. Different protonation states of the titratable residues and the polarizability of the medium are also considered. This method is more realistic than the CDC method, but much more complex and highly expensive, in terms of computational costs. Nevertheless, the results of the CDC method are rather similar to the results from the PBQC method [67].

For the FMO complex of two different green sulfur bacteria, *Prosthecochloris aestuarii* and *Chlorobium tepidum*, beside the excitonic couplings also the site energies have been determined. They differ only slightly from those determined earlier by Vulto *et al.* [43] and Wendling *et al.* [42]. Whereas the spectra calculated here with the advanced theory are clearly more similar to the experimental spectra. A main result is, that pigment 3 (numbering according to Fenna & Matthews [2]) has the lowest site energy. Calculations of the excitation energy relaxation confirm that the main part of the excitation energy relaxes within 5 ps to pigment 3. Therefore we were able to answer the question concerning the orientation of the FMO complex relative to the reaction center. It was known before, that either pigment 1 and 6 or pigment 3 and 4 are oriented towards the reaction center [11, 22]. Since the FMO complex functions as an excitation energy bridge between the outer chlorosomes and the reaction center, it follows that it must be oriented with pigments 3 and 4 toward the reaction center and with pigments 1 and 6 toward the chlorosomes. Investigations on the contributions of certain parts of the protein to the shift of the site energies of the seven pigments show that the electric field of the backbone of two α-helices determines the energy sink on pigment 3 and 4 and thereby the direction of the excitation energy transfer.

Molecular dynamics simulations have been performed for a FMO trimer in a water-box, to determine the spectral density and the correlation radius. First results are promising, however it is necessary to calculate longer time traces to obtain meaningful correlation functions and spectral densities with higher resolution. The calculation of the correlation function is based on the CDC method, developed and tested first for static structures.

For the PSI complex of the cyanobacterium *Synechococcus elongatus* beside the excitonic couplings, the site energies of the reaction center have been determined using a fit and the CDC method. In addition, with the fit also the inhomogeneous broadenings have been determined, i.e. the width of the Gaussian distribution of the site energies due to slow (in comparison to excited state life-times) protein vibrations. Since the special pair is coupled mainly by the Dexter mechanism, it was not possible to calculate that contribution by solving a Poisson equation, because only the Coulomb part is considered. Hence the fits have been performed for a set of special pair couplings ($10 \ldots 280$ cm^{-1}). We obtained the best fit (highest fitness-value) for a special pair coupling of 230 cm^{-1} in agreement with the value Madjet *et al.* [127] obtained for the sum of Dexter and Coulomb contribution by the use of quantum chemical methods.

For the fit of the site energies it was necessary to consider two boundary conditions, following from the symmetry of the crystal structure and from the CDC calculations: the site energies of pigments Acc.A and Acc.B as well as those of pigments A_0A and A_0B have to be equal. The resulting spectra are similar to the experimental spectra and the site energies have reasonable values, in particular the special pair pigment P_B has the lowest site energy, i.e. the excitation energy relaxes to P_B.

With the help of mutation experiments [130], where the H-bond to P_A has been removed, from the calculation of the spectra the localization of the triplet state could be assigned to P_A, while the cation is located on P_B.

With the CDC approach, a method is available that allowed to calculate the site energies for all 96 pigments of the complete PSI complex. With these site energies we calculated absorption, CD and LD spectra and compared them with the experimental spectra from Byrdin *et al.* [125]. For the absorption and CD spectra the agreement was rather good, while it was less agreeing for the LD spectrum. An improvement could be achieved by assigning the red chlorophylls, what was not possible up to now. In comparison with the spectra calculated with the site energies obtained by Yin *et al.* [132] from an ab initio method, our spectra are much more similar to the experiment, especially the LD spectrum.

In the framework of this thesis two of the three parameter sets of the pigment-protein-complex Hamiltonian, namely the excitonic couplings and site energies have been determined based on a microscopic model. The third parameter of the pigment-protein-complex Hamiltonian is the spectral density, that is obtained from fluorescence line narrowing spectra [30]. With these quantities it is now possible to calculate optical spectra on the basis of the crystal structure, practically without fit parameters. The electrostatic calculation of site energies provides the basis for a direct calculation of the spectral density by a combined electrostatic / molecular dynamics approach. First results in that direction are promising.

Chapter 7

Zusammenfassung

Nachdem die erste hochaufgelöste Röntgen-Kristallstruktur eines Pigment-Protein-Komplexes (FMO-Komplex [2]) vor über 30 Jahren aufgeklärt worden war, wurde in zahlreichen Veröffentlichungen versucht die optischen Tieftemperatur-Spektren dieses Komplexes zu erklären. Dabei wurde die Röntgen-Kristallstruktur verwendet, um die exzitonischen Kopplungen zwischen den Pigmenten zu berechnen und die lokalen Übergangsenergien der Pigmente wurden als Fit-Parameter behandelt.

Der Hauptgrund, warum die Suche nach einer zufriedenstellenden Beschreibung der verschiedenen linearen Spektren und einem einheitlichen Satz lokaler Übergangsenergien über 20 Jahre dauerte, war die Verwendung einer zu großen effektiven Dipolstärke (bis zu 51.6 D^2 [89]) für das optische Übergangsdipolmoment der Pigmente. Eine geringere effektive Dipolstärke wurde erstmals von Aartsma und Mitarbeitern [42, 43, 86] vorgeschlagen, und zwar 28.7 D^2 (für BChl*a*), wobei sie die Dipolstärke als Fit-Parameter behandelt hatten. Wir konnten hier die effektive Dipolstärke erstmals quantitativ begründen.

Dazu haben wir über eine störungstheoretische Behandlung der Pigment-Lösungsmittel-Wechselwirkung eine Theorie der exzitonischen Kopplung in dielektrischen Medien entwickelt. Nach dieser Theorie ist es möglich, die exzitonischen Kopplungen im dielektrischen Medium über die (numerische) Lösung der Poisson-Gleichung zu berechnen. Wir haben die exzitonischen Kopplungen für zwei verschiedene Pigment-Protein-Komplexe (FMO und PSI) unter Verwendung einer bestehenden Software [75] berechnet. Dabei haben wir als Vakuum Übergangsdipolstärken die Werte für BChl*a*/Chl*a* von Knox & Spring [18][1] und für die atomaren Übergangsladungen die TrEsp-Ladungen von Madjet *et al.* [49][2] verwendet.

Wir haben dabei herausgefunden, dass sich die effektive Dipolstärke auf ungefähr den zuvor schon in [42, 43, 86] verwendeten Wert reduziert (29.7 D^2 für BChl*a*). Weiterhin konnten wir zeigen, dass die Verwendung der Punktdipol Näherung für den FMO-Komplex beziehungsweise die *extended*-Dipol Näherung für PSI geeignet sind um die exzitonischen Kopplungen zu berechnen, wenn man dabei die von uns angegebenen Faktoren berücksichtigt ($f = 0.8$ für FMO und $f = 0.7$ für PSI), die den Einfluß des Dielektrikums beschreiben (Abschirmung und Lokalfeld-Korrektur). Die hier angegebenen Faktoren sind nicht allgemeingültig (s.u.), sondern gelten nur für die großen Kopplungen (die kleinen sind nicht relevant für die Spektren) und nur aufgrund der hier vorliegenden Geometrien.

Mit der in der Arbeit entwickelten Methode der Kopplungsberechnung wurde eine systematische Studie zur Abstands- und Richtungsabhängigkeit der Kopplungen in einem dielektrischen Medium durchgeführt. Es ergab sich der Zusammenhang $V_{\text{med}} \approx V_{\text{vac}}^{\text{ED}}(d_0) - f \cdot V_{\text{vac}}^{\text{ED}}(d_1)$, wobei f abstands- und winkelabhängig und $V_{\text{vac}}^{\text{ED}}(d_1)$ die Vakuum-Kopplung eines *extended*-Dipols der Länge $d_1 = 10$ Å ist, während $V_{\text{vac}}(d_0)$ die Vakuum-Kopplung in *extended*-Dipol Näherung mit einem Dipol der Länge $d_0 = 8.8$ Å ist. Der Vorteil dieser Beziehung ist, dass es nicht mehr nötig ist die Poisson Gleichung numerisch zu lösen

[1] Eine Analyse der Dipolstärken von BChl*a* in 15 verschiedenen Lösungsmitteln ergab eine Vakuum-Dipolstärke von 37.1 D^2.

[2] Die TrEsp-Methode bestimmt atomare Übergangsladungen durch anpassen des electrostatischen Potentials von Punktladungen an das electrostatischen Potential der quantenchemischen Übergangsdichten.

und dennoch die Kopplungen recht genau berechnet werden können. Die Parameter f und d_0 müssen für jeden Pigment-Typ neu bestimmt werden, die hier bestimmten Parameter gelten für BChl*a*. Die kürzlich von Scholes *et al.* [71] veröffentlichte exponentielle Abhängigkeit des Verhältnisses der Kopplung im Medium zur Kopplung im Vakuum konnte nur für bestimmte Geometrien der wechselwirkenden Moleküle bestätigt werden.

Die zur Berechnung der Spektren verwendete Theorie basierte lange Zeit lediglich auf der Berechnung von Strich-Spektren, die aus den Exzitonen Eigenzuständen und deren Faltung mit Gauß-Kurven [43, 86, 133] (zur effektiven Beschreibung der Pigment-Protein-Kopplung) resultieren. In der vorliegenden Arbeit wurde eine komplexere Theorie [30] verwendet, die zwar ähnliche lokale Übergangsenergien ergab wie zuvor [42, 43], jedoch Spektren erzeugt, die dem Experiment stärker ähneln als die vorhergender Ansätze. Die in dieser Arbeit verwendete Theorie berücksichtigt den Hamilton-Operator des gesamten Pigment-Protein-Komplexes $H_{\text{ppc}} = H_{\text{ex}} + H_{\text{ex-vib}} + H_{\text{vib}}$, bestehend aus dem exzitonischen und dem vibronischen Anteil, und dem Anteil der Exziton-Schwingungs Kopplung, während zuvor oft nur der exzitonische Teil berücksichtig wurde. Letztlich führt der hier verwendete Pigment-Protein-Komplex-Hamiltonian zu (i) Lebensdauerverbreiterung, (ii) Schwingungs-Seitenbanden und (iii) einer Verschiebung der einzelnen Übergänge relativ zu der Übergangsenergie die aus dem Exziton-Hamiltonian resultiert.

Im Rahmen dieser Arbeit wurden zwei im Ansatz sehr unterschiedliche Methoden zur Berechnung von lokalen Übergangsenergien entwickelt: Zum einen wurde ein genetischer Algorithmus entwickelt, der ein oder mehrere Spektren (und deren Ableitungen) simultan an die entsprechenden experimentellen Spektren anpassen kann. Die Fit-Parameter sind dabei die lokalen Übergangsenergien. Bei der Anwendung auf das Reaktionszentrum des Photosystem I hat es sich als notwendig herausgestellt, die inhomogenen Verbreiterungen für jedes einzelne Pigment ebenfalls als Fit-Parameter zu behandeln. Die zweite Methode (CDC) basiert auf einer direkten Berechnung der Ladungsdichte-Wechselwirkung der Grund- und angeregten Zustände der Pigmente mit dem Protein. Beide Methoden basieren auf der Röntgen-Kristallstruktur, wobei für den Fit nur die Positionen der Pigmente (bzw. der Stickstoff Atome N_A – N_D) benötigt werden, um daraus die exzitonische Wechselwirkung zu berechnen. In der CDC-Methode hingegen wird die atomare Struktur des gesamten Pigment-Protein-Komplexes berücksichtigt.

Es ist von großem Vorteil zwei unabhängige Methoden zur Berechnung der lokalen Übergangsenergien zur Verfügung zu haben, da es einem übereinstimmenden Ergebnis eine hohe Glaubwürdigkeit verleiht, wenn es auf zwei völlig unabhängigen Wegen erhalten wurde. Zudem erlaubt die CDC-Methode Rückschlüsse auf die Struktur-Funktions-Beziehung des Pigment-Protein-Komplexes. Die Beiträge einzelner Aminosäuren und deren Seitenketten, Wasserstoff-Brückenbindungen, sowie der Einfluß des Protein-Rückgrates beziehungsweise Teile dessen, konnten berechnet werden.

Die PBQC-Methode [26], die quantenchemische Rechnungen an BChl*a* im Vakuum und elektrostatische Rechnungen für den gesamten Pigment-Protein-Komplex kombiniert, sowie die verschiedenen Protonierungs-Zustände der titrierbaren Residuen und die Polarisierbarkeit des Mediums berücksichtigt, ist zwar einerseits realistischer als die CDC-Methode, andererseits jedoch sehr viel komplexer, und mit hohem Rechenaufwand verbunden. Die mit der CDC-Methode erhaltenen Ergebnisse ähneln den mit der PBQC-Methode erhaltenen recht stark [67].

Für den FMO-Komplex zweier verschiedener grüner Schwefelbakterien, *Prosthecochloris aestuarii* und *Chlorobium tepidum*, wurden neben den exzitonischen Kopplungen auch die lokalen Übergangsenergien bestimmt, die sich nur wenig von den von Vulto *et al.* [43] und Wendling *et al.* [42] früher bestimmten unterscheiden. Allerdings sind die hier mit der weiterentwickelten Theorie [30] berechneten Spektren dem Experiment deutlich ähnlicher. Ein wesentliches Resultat ist, dass das Pigment mit der Nummer drei (in der Nummerierung nach Fenna & Matthews [2]) die niedrigste lokale Übergangsenergie hat. Rechnungen zur Relaxation der Anregungsenergie bestätigten, dass ein Großteil der Anregungsenergie innerhalb von 5 ps auf Pigment 3 relaxiert. Somit konnten wir die Frage der Orientierung des FMO-Komplex relativ zum Reaktionszentrum beantworten. Es war zuvor bekannt, dass entweder Pigment 1 und 6 oder Pigment 3 und 4 zum Reaktionszentrum hin orientiert sind [11, 22]. Da der FMO-

Komplex als Anregungsenergie-Brücke zwischen den äußeren Chlorosomen und dem Reaktionszentrum fungiert, muß er mit den Pigmenten 3 und 4 zum Reaktionszentrum und mit den Pigmenten 1 und 6 zu den Chlorosomen hin orientiert sein. Untersuchungen zum Beitrag einzelner Teile des Proteins zu den Verschiebungen der lokalen Übergangsenergien für die sieben Pigmenten zeigten, dass das elektrische Feld des Rückgrates zweier α-Helizes die energetische Senke bei den Pigmenten 3 und 4 und damit die Richtung des Anregungsenergietransfers bestimmt.

Zur Bestimmung der Spektraldichte und des Korrelationsradius wurden Moleküldynamik Simulationen des FMO-Trimers in einer Wasserbox durchgeführt. Die ersten Ergebnisse sind vielversprechend, es ist jedoch notwendig längere Zeitspuren zu berechnen, um aussagekräftigere und besser aufgelöste Korrelationsfunktionen und sich daraus ergebende Spektraldichten zu erhalten. Die Berechnung der Korrelationsfunktion basiert hierbei auf der zuvor für statische Strukturen entwickelten CDC-Methode.

Für das Photosystem I des Cyanobakteriums *Synechococcus elongatus* wurden neben den exzitonischen Kopplungen die lokalen Übergansenergien für das Reaktionszentrum mittels Fit und CDC-Methode bestimmt, desweiteren wurden mit dem Fit auch die inhomogene Breiten bestimmt, d.h. die Breite der Gauß-Verteilung der lokalen Übergangsenergien aufgrund der langsamen (im Vergleich zur Lebensdauer angeregter Zustände) Proteinschwingungen. Da das *special pair* hauptsächlich über den Dexter-Mechanismus gekoppelt ist, war es nicht möglich diese Kopplung über die Lösung der Poisson Gleichung zu bestimmen, da dabei nur der Coulomb Anteil berücksichtigt werden kann. Die Fits wurden daher für eine Reihe von Werten für die *special pair* Kopplung ($10 \ldots 280$ cm^{-1}) berechnet. Dabei erhielten wir den besten Fit (höchster Fitnesswert) für eine *special pair* Kopplung von 230 cm^{-1}, in Übereinstimmung mit den Werten die Madjet *et al.* [127] mit quantenchemischen Methoden für die Summe von Dexter- und Coulomb-Anteil erhalten haben.

Beim Fit der lokalen Übergangsenergien war es notwendig zwei Randbedingungen, die aus der Symmetrie der Röntgen-Kristallstruktur und den CDC-Rechnungen folgen, zu beachten, und zwar, dass die lokalen Übergangsenergien der Pigmente Acc.A und Acc.B gleich sind, ebenso wie die der Pigmente A_0A und A_0B. Die resultierenden Spektren ähneln den experimentellen Spektren stark und die lokalen Übergansenergien haben plausible Werte. Insbesondere hat das *special pair* Pigment P_B die niedrigste lokale Übergangsenergie, dass heißt, die Anregungsenergie relaxiert nach P_B.

Mit Hilfe von Mutations-Experimenten [130], bei denen eine Wasserstoff- Brückenbindung zu P_A entfernt wurde, konnte aus der Berechnung der Spektren die Lokalisierung des Triplett-Zustandes P_A zugeordnet werden, während das Kation auf P_B lokalisiert ist.

Durch die CDC-Methode stand uns eine Methode zur Verfügung, mit der wir die lokalen Übergangsenergien für den gesamten PSI-Komplex mit seinen 96 Pigmenten berechnen konnten. Mit den so erhaltenen lokalen Übergangsenergien haben wir die optischen Absorptions-, CD- und LD-Spektren berechnet und mit den experimentellen Spektren von Byrdin *et al.* [125] verglichen. Für Absorption und CD ergab sich dabei eine recht gute Übereinstimmung, für LD eine weniger gute. Eine Verbesserung könnte hier durch die Zuordnung der rotverschobenen Chlorophylle erreicht werden, die aber bis jetzt noch nicht eindeutig möglich war. Im Vergleich mit den Spektren, die sich mit den lokalen Übergangsenergien ergeben haben, die Yin *et al.* [132] mit einer ab-initio Methode berechnet haben, sehen unsere Spektren den experimentellen wesentlich ähnlicher, insbesondere beim LD-Spektrum.

Im Rahmen dieser Arbeit wurden zwei der drei Parametersätze des Hamilton-Operators des Pigment-Protein-Komplexes, nämlich die exzitonischen Kopplungen und die lokalen Übergangsenergien, basierend auf einem mikroskopischen Modell, bestimmt. Der dritte Parameter dieses Hamilton-Operators ist die Spektraldichte, die aus Fluoreszenz-*line-narrowing*-Spektren erhalten wurde [30]. Mit diesen Größen ist es nun möglich, optische Spektren praktisch ohne Fit-Parameter nur auf der Röntgen-Struktur basierend, zu berechnen. Die elektrostatische Berechnung der lokalen Übergangsenergien bildet die Basis für die direkte Berechnung der Spektraldichte durch Kombination von elektrostatischen Rechnungen mit Moleküldynamik-Simulationen. Erste Ergebnisse in dieser Richtung sind vielversprechend.

Bibliography

[1] L. Taiz and E. Zeiger. *Plant Physiology*. Sinauer Associates, third edition edition, 2002.

[2] R.E. Fenna and B.W. Matthews. Chlorophyll arrangement in a bacteriochlorophyll protein from *Chlorobium-Limicola*. *Nature*, 258:573–577, 1975.

[3] J. Deisenhofer, O. Epp., K. Miki, R. Huber, and H. Michel. Structure of the protein subunits in the photosynthetic reaction centre of *Rhodopseudomonas viridis* at 3 Å resolution. *Nature*, 318:618–624, 1985.

[4] R. Emerson and W. Arnold. The photochemical reaction in photosynthesis. *J. Gen. Physiol.*, 16:191–205, 1932.

[5] P. Jordan, P. Fromme, H.T. Witt, O. Klukas, W. Saenger, and N. Krauß. Three-dimensional structure of cyanobacterial photosystem I at 2.5 Å resolution. *Nature*, 411:909–917, 2001.

[6] K.N. Ferreira, T.M. Iverson, K. Maghlaoui, J. Barber, and S. Iwata. Architecture of the photosynthetic oxygen-evolving center. *Science*, 303:1831–1838, 2004.

[7] B. Loll, J. Kern, W. Saenger, A. Zouni, and J. Biesiadka. Towards complete cofactor arrangement in the 3.0 Å resolution structure of photosystem II. *Nature*, 438:1040–1044, 2005.

[8] R.E. Blankenship, J.M. Olson, and M. Mette. Antenna complexes from green photosynthetic bacteria. In R.E. Blankenship, M.T. Madigan, and C.E. Bauer, editors, *Anoxygenic photosynthetic bacteria*, pages 399–435. Kluwer Academic Publishers, Dordrecht, Netherlands, 1995.

[9] J.M. Olson. The FMO protein. *Photosynth. Res.*, 80:181–187, 2004.

[10] A. Egawa, T. Fujiwara, T. Mizoguchi, Y. Kakitani, Y. Koyama, and H. Akutsu. Structure of the light-harvesting bacteriochlorophyll *c* assembly in chlorosomes from *Chlorobium limicola* determined by solid-state NMR. *Proc. Natl. Acad. Sci. USA*, 104:790–795, 2007.

[11] H.W. Rémigy, G. Hauska, S.A. Müller, and G. Tsiotis. The reaction centre from green sulphur bacteria: progress towards structural elucidation. *Photosynth. Res.*, 71:91–98, 2002.

[12] H. Scheer. Structure and Occurrence of Chlorophylls. In H. Scheer, editor, *Chlorophylls*, pages 3–30. CRC Press, London, 1991.

[13] H. Miyashita, H. Ikemoto, N. Kurano, K. Adachi, M. Chihara, and S. Miyachi. Chlorophyll *d* as a major pigment . *Nature*, 383:402, 1996.

[14] Y. Koyama, M. Kuki, P.O. Andersson, and T. Gillbro. Singlet excited states and the light harvesting function of Carotenoids in bacterial photosynthesis. *Photochem. Photobiol.*, 63:243–256, 1996.

[15] H.A. Frank and R. Cogdell. Carotenoids in photosythesis. *Photochem. Photobiol.*, 63:257–264, 1996.

[16] L.K. Hanson. Molecular Orbital Theory Of Monomer Pigments. In H. Scheer, editor, *Chlorophylls*, pages 993–1014. CRC Press, London, 1991.

[17] M. Gouterman. Spectra of Porphyrins. *J. Molec. Spectr.*, 6:138–163, 1961.

[18] R.S. Knox and B.Q. Spring. Dipole strengths in the chlorophylls. *Photochem. Photobiol.*, 77(5):497–501, 2003.

[19] J.B. Sumner. The Isolation and Crystallization of the Enzyme Urease. Preliminary Paper. *J. Biol. Chem.*, 69:435–441, 1926.

[20] M.F. Perutz, M.G. Rossmann, A.F. Cullis, H. Muirhead, G. Will, and A.C.T. North. Structure of haemoglobin. A three-dimensional Fourier synthesis at 5.5 Å resolution, obtained by X-ray analysis. *Nature*, 185:416–422, 1960.

[21] J.C. Kendrew, G. Bodo, H.M. Dintzis, R.G. Parrish, H. Wyckoff, and D.C. Phillips. A Three-Dimensional Model of the Myoglobin Molecule Obtained by X-ray Analysis. *Nature*, 181:662–666, 1958.

[22] H.W. Rémigy, H. Stahlberg, D. Fotiadis, B. Wolpensinger, A. Engel, G. Hauska, and G. Tsiotis. The reaction centre complex from green sulphur bacterium *C. tepidum*: a structural analysis by scanning transmission electron microscopy. *J. Mol. Biol.*, 290:851–858, 1999.

[23] D.E. Tronrud, M.F. Schmid, and B.W. Matthews. Structure and X-ray amino acid sequence of a bacteriochlorophyll *a* protein from *Prosthecochloris aestuarii* refined at 1.9 Å resolution. *J. Mol. Biol.*, 188:443–454, 1986.

[24] Y.F. Li, W. Zhou, R.E. Blankenship, and J.P. Allen. Crystal structure of the bacteriochlorophyll *a* protein from *Chlorobium tepidum*. *J. Mol. Biol.*, 271:456–471, 1997.

[25] H. Li, N.U. Frigaard, and D.A. Bryant. Molecular contacts for chlorosome envelope proteins revealed by cross-linking studies with chlorosomes from Chlorobium tepidum. *Biochemistry*, 45:9095–9103, 2006.

[26] F. Müh, M.E. Madjet, J. Adolphs, A. Abdurahman, B. Rabenstein, H. Ishikita, E.W. Knapp, and T. Renger. α-helices direct excitation energy flow in the Fenna-Matthews-Olson protein. *Proc. Natl. Acad. Sci. USA*, 104(43):16862–16867, 2007.

[27] R. Emerson. Yield of Photosynthesis from Simultaneous Illumination with Pairs of Wavelengths. *Science*, 127:1059–1060, 1958.

[28] T. Förster. Zwischenmolekulare Energiewanderung und Fluoreszenz. *Ann. d. Physik*, 437(1-2):55–75, 1948.

[29] D.L. Dexter. A Theory of sensitized Luminescence in Solids. *J. Chem. Phys.*, 21:836–850, 1953.

[30] T. Renger and R.A. Marcus. On the relation of protein dynamics and exciton relaxation in pigment-protein complexes: An estimation of the spectral density and a theory for the calculation of optical spectra. *J. Chem. Phys.*, 116:9997–10019, 2002.

[31] V. May and O. Kühn. *Charge and Energy Transfer Dynamics in Molecular Systems: A Theoretical Introduction*. Wiley-VCH, Berlin, 2000.

[32] G. Raszewski, W. Saenger, and T. Renger. Theory of optical spectra of Photosystem II reaction centers: Location of the triplet state and the identity of the primary electron donor. *Biophys. J.*, 88:986–998, 2005.

[33] S. Mukamel. Non-Markovian Theory of Molecular Relaxation. I. Vibrational Relaxation and Dephasing in Condensed Phases. *Chem. Phys.*, 37:33–47, 1979.

[34] J. Breton, A. Hardisson, F. Mauricio, and S. Velasco. Relaxation of quantum systems weakly coupled to a bath. I. Total-time-ordering-cumulant and partial-time-ordering-cumulant non-Markovian theories. *Phys. Rev. A*, 30:542–552, 1984.

[35] T. Renger, V. May, and O. Kühn. Ultrafast Excitation Energy Transfer Dynamics in Photosynthetic Pigment-Protein Complexes. *Phys. Reports*, 343:138–254, 2001.

[36] T. Renger and V. May. Simulations of frequency-domain spectra: Structure-function relationships in photosynthetic pigment-protein complexes. *Phys. Rev. Lett.*, 84:5228–5231, 2000.

[37] A.D. McNaught and A. Wilkinson. *Compendium of Chemical Terminology*, volume 68. Blackwell Science, the gold book, second edition edition, 1997.

[38] S. Jang, J. Cao, and R.J. Silbey. On the temperature dependence of molecular line shapes due to linearly coupled phonon bands. *J. Phys. Chem.*, 106:8313–8317, 2002.

[39] T. Renger. Theory of optical spectra involving charge transfer states: Dynamic localization predicts a temperature dependent optical band shift. *Phys. Rev. Lett.*, 93(18):188101(1)–188101(4), 2004.

[40] W.H. Press, S.A. Teukolsky, W.T. Vetterling, and B.P. Flannery. *Numerical Recipes in C, second edition*. Cambridge, 1992.

[41] E.W. Knapp. Lineshapes of molecular aggregates - exchange narrowing and intersite correlation. *Chem. Phys.*, 85:73–82, 1984.

[42] M. Wendling, M.A. Przyjalgowski, D. Gülen, S.I.E. Vulto, T.J. Aartsma, R. van Grondelle, and H. van Amerongen. The quantitative relationship between structure and polarized spectroscopy in the FMO complex of *Prosthecochloris aestuarii*: Refining experiments and simulations. *Photosynth. Res.*, 71:99–123, 2002.

[43] S.I.E. Vulto, M.A. de Baat, R.J.W. Louwe, H.P. Permentier, T. Neef, M. Miller, H. van Amerongen, and T.J. Aartsma. Exciton simulations of optical spectra of the FMO complex from the green sulfur bacterium *Chlorobium tepidum* at 6 K. *J. Phys. Chem. B*, 102:9577–9582, 1998.

[44] M. Wendling, T. Pullerits, M.A. Przyjalgowski, S.I.E. Vulto, T.J. Aartsma, R. van Grondelle, and H. van Amerongen. Electron-vibrational coupling in the Fenna-Matthews-Olson complex of *Prosthecochloris aestuarii* determined by temperature-dependent absorption and fluorescence line-narrowing measurements. *J. Phys. Chem. B*, 104:5825–5831, 2000.

[45] W.M. Zhang, T. Meier, V. Chernyak, and S. Mukamel. Exciton-migration and three–pulse femtosecond optical spectroscopies of photosynthetic antenna complexes. *J. Chem. Phys.*, 108:7763–7774, 1998.

[46] M. Yang and G.R. Fleming. Influence of phonons on exciton transfer dynamics: comparison of the Redfield, Förster, and modified Redfield equations. *Chem. Phys.*, 275:355–372, 2002.

[47] T. Renger and R.A. Marcus. Variable–range hopping electron transfer through disordered bridge states: Application to DNA. *J. Chem. Phys.*, 107:8404–8419, 2003.

[48] J. Adolphs and T. Renger. Theory of Excitonic Couplings in Dielectric Media. *In preparation*, 2008.

[49] M.E. Madjet, A. Abdurahman, and T. Renger. Interpigment Coulomb couplings from ab-initio transition charges: Application to strongly coupled pigments in photosynthetic antennae and reaction centers. *J. Phys. Chem. B*, 110:17268–17281, 2006.

[50] P. Atkins and R. Friedman. *Molecular Quantum Mechanics*. Oxford University Press, fourth edition edition, 2005.

[51] G. McDermott, S.M. Prince, A.A. Freer, A.M. Hawthornthwaite-Lawless, M.Z. Papiz, R.J. Cogdell, and N.W. Isaacs. Crystal structure of an integral membrane light-harvesting complex from photosynthetic bacteria. *Nature*, 374:517–521, 1995.

[52] T.M.H. Creemers, C.A. de Caro, R.W. Visschers, R. van Grondelle, and S. Völker. Spectral hole burning and fluorescence line narrowing in subunits of the light-harvesting complex LH1 of purple bacteria. *J. Phys. Chem. B*, 103:9770–9776, 1999.

[53] J. Adolphs and T. Renger. How proteins trigger excitation energy transfer in the FMO complex of green sulfur bacteria. *Biophys. J.*, 91:2778–2797, 2006.

[54] A. Freiberg, S. Lin, K. Timpmann, and R.E. Blankenship. Exciton dynamics in FMO bacteriochlorophyll-protein at low temperatures. *J. Phys. Chem. B*, 101:7211–7220, 1997.

[55] A. Warshel and J.-K. Hwang. Simulation of The Dynamics of Electron Transfer Reactions in Polar Solvents: Semiclassical Trajectories and Dispersed Polaron Approaches. *J. Chem. Phys.*, 84:4938–4957, 1986.

[56] T. Renger. Basic photophysical principles: Absorption of light, excitation energy transfer and electron transfer reactions. In G. Renger, editor, *Primary processes in photosynthesis: Basic principles and apparatus*, pages 37–97. Springer, 2008.

[57] C. Jr. Weiss. Title. *J. Mol. Spectrosc.*, 44:37, 1972.

[58] J.C. Chang. Monopole effects on electronic excitation interaction between large molecules. I. Application to energy transfer in chlorophylls. *J. Chem. Phys.*, 67:3901–3909, 1977.

[59] G.D. Scholes. Long range resonance energy transfer in molecular systems. *Annu. Rev. Phys. Chem.*, 54:57–87, 2003.

[60] R. McWeeny. *Methods of Molecular Quantum Mechanics*. Academic Press Inc., U.S., 1992.

[61] B.P. Krueger, G.D. Scholes, and G.R. Fleming. Calculation of couplings and energy-transfer pathways between the pigments of LH2 by the ab initio transition density cube method. *J. Phys. Chem. B*, 102:5378–5386, 1998.

[62] J.D. Jackson. *Classical Electrodynamics*. John Wiley & Sons, second edition edition, 1975.

[63] R.S. Knox and H. van Amerongen. Refractive index dependence of the Förster resonance excitation transfer rate. *J. Phys. Chem. B*, 106(20):5289–5293, 2002.

[64] C.-P. Hsu, M. Head-Gordon, T. Head-Gordon, and G.R. Fleming. Excitation energy transfer in condensed media. *J. Chem. Phys.*, 114:3065–3072, 2001.

[65] A.D. MacKerell Jr., D. Bashford, M. Bellott, R.L. Dunbrack Jr., J.D. Evanseck, M.J. Field, S. Fischer, J. Gao, H. Guo, S. Ha, D. Joseph-McCarthy, L. Kuchnir, K. Kuczera, F.T.K. Lau, C. Mattos, S. Michnick, T. Ngo, D.T. Nguyen, B. Prodhom, W.E. Reiher, III, B. Roux, M. Schlenkrich, J.C. Smith, R. Stote, J. Straub, M. Watanabe, J. Wiorkiewicz-Kuczera, D. Yin, and M. Karplus. All-atom empirical potential for molecular modeling and dynamics studies of proteins. *J. Phys. Chem. B*, 102:3586–3616, 1998.

[66] D. Bashford and M. Karplus. pK_a's of ionizable groups in proteins: atomic detail from a continuum electrostatic model. *Biochemistry*, 29:10219–10225, 1990.

[67] J. Adolphs, F. Müh, M.E. Madjet, and T. Renger. Calculation of Pigment Transition Energies in the FMO Protein: From Simplicity to Complexity and Back. *Photosynth. Res.*, 95(2-3):197–209, 2008.

[68] Jaguar 5.5, Schrödinger, L.L.C., Portland, OR, 1991-2003.

[69] J. Kong, C.A. White, A.I. Krylov, C.D. Sherrill, R.D. Adamson, T.R. Furlani, M.S. Lee, A.M. Lee, S.R. Gwaltney, T.R. Adams, C. Ochsenfeld, A.T.B. Gilbert, G.S. Kedziora, V.A. Rassolov, D.R. Maurice, N. Nair, Y. Shao, N.A. Besley, P.E. Maslen, J.P. Dombroski, H. Dachsel, W.M. Zhang, P.P. Korambath, J. Baker, E.F.C. Byrd, T. Van Voorhis, M. Oumi, S. Hirata, C.P. Hsu, N. Ishikawa, J. Florian, A. Warshel, B.G. Johnson, P.M.W. Gill, M. Head-Gordon, and J.A. Pople. Q-Chem 2.0: a high-performance ab initio electronic structure program package. *J. Comput. Chem.*, 21:1532–1548, 2000.

[70] E. Sigfridsson and U. Ryde. Comparison of methods for deriving atomic charges from the electrostatic potential and moments. *J. Comp. Chem.*, 19:377 – 395, 1998.

[71] G.D. Scholes, C. Curutchet, B. Mennucci, R. Cammi, and J. Tomasi. How solvent controls electronic energy transfer and light harvesting. *J. Phys. Chem. B*, 111:6978–6982, 2007.

[72] O. Kühn, T. Renger, and V. May. On the Theory of Ultrafast Exciton Transfer Dynamics: The Chlorophyll a/b Dimer. *Chem. Phys.*, 204:99–114, 1996.

[73] T. Renger, O. Kühn, J. Voigt, and V. May. Theory of Pump-Probe-Spectroscopy on the Light Harvesting Complex of Photosystem II. *J. Phys. Chem.*, 100:15654–15662, 1996.

[74] W. Humphrey, A. Dalke, and K. Schulten. VMD - Visual Molecular Dynamics. *J. Molec. Graphics*, 14:33–38, 1996.

[75] D. Bashford. MEAD (Macroscopic Electrostatics with Atomic Detail), Download: anonymous FTP from ftp.scripps.edu, directory pub/bashford using an FTP program. *The Scripps Research Institute*, 1990-1998.

[76] *Gnuplot* is a command-driven interactive function plotting program. *Gnuplot* is copyrighted, but freely distributable.

[77] W. Kinnebrock. *Optimierung mit genetischen und selektiven Algorithmen*. Oldenbourg, 1994.

[78] H. Pohlheim. *Evolutionäre Algorithmen*. Springer, Berlin Heidelberg, 1999.

[79] B. Brüggemann, K. Sznee, V. Novoderezhkin, R. van Grondelle, and V. May. Modeling exciton dynamics in the photosynthetic antenna PS1. *J. Phys. Chem. B*, 108:13536–13546, 2004.

[80] P. Kjellberg, Z. He, and T. Pullerits. Bacteriochlorophyll in electric field. *J. Phys. Chem. B*, 107:13737–13742, 2003.

[81] A.Y. Mulkidjanian, D.A. Cherepanov, M. Haumann, and W. Junge. Photosystem II of green plants: Topology of core pigments and redox cofactors as inferred from electrochromic difference spectra. *Biochemistry*, 35:3093–3107, 1996.

[82] L.M.P. Beekman, R.N. Frese, G.J.S. Fowler, R. Picorel, R.J. Cogdell, I.H.M. van Stokkum, C.N. Hunter, and R. van Grondelle. Characterization of the light-harvesting antennas of photosynthetic purple bacteria by Stark spectroscopy. 2. LH2 complexes: Influence of the protein environment. *J. Chem. Phys. B*, 101:7293–7301, 1997.

[83] I. Renge. Solvent effects on the visible absorption maxima of tetrapyrrolic pigments. *J. Phys. Chem.*, 97:6582–6589, 1993.

[84] M.A. Steffen, K. Lao, and S.G. Boxer. Dielectric asymmetry in the photosynthetic reaction center. *Science*, 264:810–816, 1994.

[85] D.J. Lockhart and S.G. Boxer. Magnitude and direction of the change in dipole moment associated with excitation of the primary electron donor in *Rhodopseudomonas sphaeroides* reaction centers. *Biochemistry*, 26:664–668, 1987.

[86] R.J.W. Louwe, J. Vrieze, A.J. Hoff, and T.J. Aartsma. Towards an integral interpretation of the optical steady state spectra of the FMO-complex of *Prosthecochloris-aestuarii*. 2. Exciton simulations. *J. Phys. Chem. B*, 101:11280–11287, 1997.

[87] E. Gudowska-Nowak, M.D. Newton, and J. Fajer. Conformational and environmental effects on bacteriochlorophyll optical spectra: Correlations of calculated spectra with structural results. *J. Phys. Chem.*, 94:5795–5801, 1990.

[88] A.N. Melkozernov, J.M. Olson, Y.F. Li, J.P. Allen, and R.E. Blankenship. Orientation and excitonic interactions of the Fenna-Matthews-Olson bacteriochlorophyll *a* protein in membranes of the green sulfur bacterium *Chlorobium tepidum*. *Photosynth. Res.*, 56:315–328, 1998.

[89] R.M. Pearlstein. Theory of the optical spectra of the bacteriochlorophyll *a* antenna protein trimer from *Prosthecochloris aestuarii*. *Photosynth. Res.*, 31:213–226, 1992.

[90] X. Lu and R.M. Pearlstein. Simulations of *Prosthecochloris* bacteriochlorophyll *a*-protein optical spectra improved by parametric computer search. *Photochem. Photobiol.*, 57:86–91, 1993.

[91] D. Gülen. Interpretation of the excited-state structure of the Fenna-Matthews-Olson protein of the photosynthtetic pigment-protein complex of *Prosthecochloris aestuarii* based on simultaneous simulation of the 4 K absorption, linear dichroism, and singlet-triplet absorption difference spectra: A possible excitonic explanation? *J. Phys. Chem.*, 100:17683–17689, 1996.

[92] T. Renger and V. May. Ultrafast exciton motion in photosynthetic antenna systems: The FMO-complex. *J. Phys. Chem. A*, 102:4381–4391, 1998.

[93] T. Simonson and III C.L. Brooks. Charge screening and the dielectric constant of proteins: Insights from molecular dynamics. *J. Am. Chem. Soc.*, 118:8452–8458, 1996.

[94] T. Simonson. Electrostatics and dynamics of proteins. *Rep. Prog. Phys.*, 66:737–787, 2003.

[95] M.K. Gilson and B.H. Honig. The dielectric constant of a folded protein. *Biopolymers*, 25:2097–2119, 1986.

[96] B.H. Honig and A. Nicholls. Classical electrostatics in biology and chemistry. *Science*, 268:1144–1149, 1995.

[97] G.M. Ullmann and E.W. Knapp. Electrostatic models for computing protonation and redox equilibria in proteins. *Eur. Biophys. J.*, 28:533–550, 1999.

[98] B. Rabenstein, G.M. Ullmann, and E.W. Knapp. Electron transfer between the Quinones in the photosynthetic reaction center and its coupling to conformational changes. *Biochemistry*, 39:10487–10496, 2000.

[99] H. Ishikita and E.W. Knapp. Variation of Ser-L223 hydrogen bonding with the QB redox state in reaction centers from Rhodobacter sphaeroide. *J. Am. Chem. Soc.*, 126:8059–8064, 2004.

[100] B.A. Diner, E. Schlodder, P.J. Nixon, W.J. Coleman, F. Rappaport, J. Lavergne, W.F.J. Vermaas, and D.A. Chisholm. Site-directed mutations at D1-HIS198 and D2-HIS197 of Photosystem II in *Synechocystis* PCC 6803: Sites of primary charge separation and cation and triplet stabilization. *Biochemistry*, 40:9265–9281, 2001.

[101] H. Heinz, U.W. Suter, and E. Leontidis. Simple and accurate computations of solvatochromic shifts in $\pi \rightarrow \pi^*$ transitions of aromatic chromophores. *J. Am. Chem. Soc.*, 123:11229–11236, 2001.

[102] N.S. Bayliss. The effect of the electrostatic polarization of the solvent on electronic absorption spectra in solution. *J. Chem. Phys.*, 18:292–296, 1950.

[103] H.C. Longuet-Higgens and J.A. Pople. Electronic spectral shifts of nonpolar molecules in nonpolar solvents. *J. Chem. Phys.*, 27:192–194, 1957.

[104] D. Bauman and D. Wrobel. Dichroism and polarized fluorescence of chlorophyll *a*, chlorophyll *c* and bacteriochlorophyll *a* dissolved in liquid crystals. *Biophys. Chem.*, 12:83–91, 1980.

[105] S. Georgakopoulou, R.N. Frese, E. Johnson, C. Koolhaas, R.J. Cogdell, R. van Grondelle, and G. van der Zwan. Absorption and CD spectroscopy and modeling of various LH2 complexes from purple bacteria. *Biophys. J.*, 82:2184–2197, 2002.

[106] M. Fragata, B. Norden, and T. Kurucsev. Linear dichroism (250-700 nm) of chlorophyll *a* and pheophytine *a* oriented in a lamellar phase of glycerylmonooctanoate/H2O. *Photochem. Photobiol.*, 47:133–143, 1988.

[107] F.J. Kleima, E. Hofmann, B. Gobets, I.H.M. van Stokkum, R. van Grondelle, K. Diederichs, and H. van Amerongen. Förster excitation energy transfer in peridinin-chlorophyll-*a*-protein. *Biophys. J.*, 78:344–353, 2000.

[108] S.I.E. Vulto, M.A. de Baat, S. Neerken, F.R. Nowak, H. van Amerongen, J. Amesz, and T.J. Aartsma. Excited-state dynamics in FMO antenna complexes from photosynthetic green sulfur bacteria: A kinetic model. *J. Phys. Chem. B*, 103:8153–8161, 1999.

[109] M. Cho, H.M. Vaswani, T. Brixner, J. Stenger, and G.R. Fleming. Exciton Analysis in 2D Electronic Spectroscopy. *J. Phys. Chem. B*, 109:10542–10556, 2005.

[110] T. Pullerits, R. Monshouwer, F. van Mourik, and R. van Grondelle. Temperature dependence of electron-vibronic spectra of photosynthetic systems. *Chem. Phys.*, 194:395–407, 1995.

[111] J. Pieper, J. Voigt, G. Renger, and G.J. Small. Analysis of phonon structure in line-narrowed optical spectra. *Chem. Phys. Lett.*, 310:296–302, 1999.

[112] S.I.E. Vulto, A.M. Streltsov, and T. . Aartsma. Excited state energy relaxation in the FMO complexes of the green bacterium *Prosthecochloris aestuarii* at low temperatures. *J. Phys. Chem. B*, 101:4845–4850, 1997.

[113] S.I.E. Vulto, S. Neerken, R.J.W. Louwe, M.A. de Baat, J. Amesz, and T.J. Aartsma. Excited-state structure and dynamics in FMO antenna complexes from photosynthetic green sulfur bacteria. *J. Phys. Chem. B*, 102:10630–10635, 1998.

[114] T. Renger and R.A. Marcus. Photophysical Properties of PS-2 Reaction Centers and a Discrepancy in Exciton Relaxation Times. *J. Phys. Chem. B*, 106:1809–1819, 2002.

[115] T. Brixner, J. Stenger, H.M. Vaswani, M. Cho, R. Blankenship, and G.R. Fleming. Two-dimensional spectroscopy of electronic couplings in photosynthesis. *Nature*, 434:625–628, 2005.

[116] S. Jang, M.D. Newton, and R.J. Silbey. Multichromophoric Förster resonance energy transfer. *Phys. Rev. Lett.*, 92:218301, 2004.

[117] O. Kühn, V. Sundström, and T. Pullerits. Fluorescence depolarization dynamics in the B850 complex of purple bacteria. *Chem. Phys.*, 275:15–30, 2002.

[118] P. Kjellberg and T. Pullerits. Tree-pulse photon echo of an excitonic dimer modeled via Redfield theory. *J. Chem. Phys.*, 124:024106(1)–024106(9), 2006.

[119] A. Damjanovic, H.M. Vaswani, P. Fromme, and G.R. Fleming. Chlorophyll excitations in Photosystem I of *Synechococcus elongatus*. *J. Phys. Chem. B*, 106:10251–10262, 2002.

[120] R.P. Sheridan, R.M. Levy, and F.R. Salemme. α-helix dipole model and electrostatic stabilization of 4-α-helical proteins. *Proc. Natl. Acad. Sci. USA*, 79:4545–4549, 1982.

[121] H. Ishikita, W. Saenger, J. Biesiadka, B. Loll, and E.W. Knapp. How photosynthetic reaction centers control oxidation power in chlorophyll pairs P680, P700 and P870. *Proc. Natl. Acad. Sci. USA*, 103:9855–9860, 2006.

[122] G.J.S. Fowler, R.W. Visschers, G.G. Grief, R. van Grondelle, and C.N. Hunter. Genetically modified photosynthetic antenna complexes with blueshifted absorbance bands. *Nature*, 355:848–850, 1992.

[123] J.C. Phillips, R. Braun, W. Wang, J. Gumbart, E. Tajkhorshid, E. Villa, C. Chipot, R.D. Skeel, L. Kale, and K. Schulten. Scalable molecular dynamics with NAMD. *J. Comput. Chem.*, 26:1781–1802, 2005.

[124] B.R. Brooks, R.E. Bruccoleri, B.D. Olafson, D.J. States, S. Swaminathan, and M. Karplus. CHARMM: A program for macromolecular energy, minimization, and dynamics calculations. *J. Comp. Chem.*, 4:187–217, 1983.

[125] M. Byrdin, P. Jordan, N. Krauss, P. Fromme, D. Stehlik, and E. Schlodder. Light Harvesting in Photosystem I: Modeling Based on the 2.5-Å Structure of Photosystem I from *Synechococcus elongatus*. *Biophys. J.*, 83:433–457, 2002.

[126] E. Schlodder, V.V. Shubin, E. El-Mohsnawy, M. Roegner, and N.V. Karapetyan. Steady-state and transient polarized absorption spectroscopy of photosystem I complexes from the cyanobacteria *Arthrospira platensis* and *Thermosynechococcus elongatus*. *Biochim. Biophys. Acta*, 1767:732–741, 2007.

[127] M.E. Madjet, F. Müh, and T. Renger. Calculation of short-range pigment-pigment coupling in photosynthetic reaction centers. *In preparation*, 2008.

[128] H. Witt, E. Bordignon, D. Carbonera, J.P. Dekker, N. Karapetyan, C. Teutloff, A. Webber, W. Lubitz, and E. Schlodder. Species–specific Differences of the Spectroscopic Properties of P700: analysis of the influence of non–conserved amino acid residues by site–directed mutagenesis of photosystem I from *Chlamydomonas reinhardtii*. *J. Biol. Chem.*, 278(47):46760–46771, 2003.

[129] H. Käß, P. Fromme, H.T. Witt, and W. Lubitz. Orientation and electronic structure of the primary electron donor radical cation in photosystem I: a single crystal EPR and ENDOR study. *J. Phys. Chem. B*, 105:1225–1239, 2001.

[130] H. Witt, E. Schlodder, C. Teutloff, J. Niklas, E. Bordignon, D. Carbonera, S. Kohler, A. Labahn, and W. Lubitz. Hydrogen bonding to P700: Site-directed mutagenesis of threonine A739 of Photosystem I in *Chlamydomonas reinhardtii*. *Biochemistry*, 41:8557–8569, 2002.

[131] A.W. Rutherford and P. Sétif. Orientation of P700, the primary electron donor of photosystem I. *Biochim. Biophys. Acta*, 1019:128–132, 1990.

[132] S. Yin, M.G. Dahlbom, P.J. Canfield, N.S. Hush, R. Kobayashi, and J.R. Reimers. Assignment of the Q_y Absorption Spectrum of Photosystem-I from *Thermosynechococcus elongatus* Based on CAM-B3LYP Calculations at the PW91-Optimized Protein Structure. *J. Phys. Chem. B*, 111:9923–9930, 2007.

[133] R.M. Pearlstein and R.P. Hemenger. Bacteriochlorophyll electronic-transition moment directions in bacteriochlorophyll *a*-protein. *Proc. Natl. Acad. Sci. USA*, 75:4920–4924, 1978.

Publications

Journals

Adolphs J and Renger T. How proteins trigger excitation energy transfer in the FMO complex of green sulfur bacteria. *Biophys. J.* **91**: 2778-2797 (2006).

Müh F, Madjet ME, Adolphs J, Abdurahman A, Rabenstein B, Ishikita H, Knapp EW and Renger T. α-Helices Direct Excitation Energy Flow in the Fenna-Matthews-Olson Protein. *Proc. Natl. Acad. Sci. USA* **104** (43): 16862-16867 (2007).

Adolphs J, Müh F, Madjet ME and Renger T. Calculation of Pigment Transition Energies in the FMO Protein: From Simplicity to Complexity and Back. *Photosynth. Res.* **95** (2-3): 197-209 (2008).

Adolphs J and Renger T. Theory of Excitonic Couplings in Dielectric Media. *In Preparation* (2008).

Book Chapters

Adolphs J. Photosynthesis: How Proteins Control Excitation Energy Transfer. In: *Handbook of Research on Systems Biology Applications in Medicine*. Daskalaki, A. Ed (*in press*).

Conferences

Poster: PS2007, XIVth international congress on photosynthesis. Glasgow, July 22-27, 2007. *Dynamic modulation of pigment transition energies by the protein.*

Poster: Light harvesting systems workshop 2007 (satellite meeting to PS2007). Drymen (Scotland), July 19-22, 2007. *Dynamic modulation of pigment transition energies by the protein.*

Poster: Light Harvesting Processes 2007. Banz Monastery, March 21-24, 2007. *Dynamic modulation of pigment transition energies by the protein.*

Poster: Bunsentagung 2006. Erlangen, May 25-27, 2006. *Tuning of Excitation Energies of Pigments by the Protein: Application to the FMO Complex.*

Poster: Protein cofactor interactions in biological processes (international symposium). Caputh, May 13-15, 2004. *Dynamical theory and a genetic algorithm for the extraction of site energies of pigments in photosynthetic antennae*.

Danksagung

Mein Dank geht an . . .

. . . Thomas Renger für die angenehme Zusammenarbeit, seine Unterstützung, die fruchtbaren Diskussionen und nicht zuletzt für die gewissenhafte Betreuung meiner Arbeit.

. . . Walter Knapp für seine Unterstützung und die freundliche Aufnahme in seiner Arbeisgruppe.

. . . Volkhard May für die Erstellung des zweiten Gutachtens.

. . . Jorge Numata für die Zusammenarbeit an den MD Simulationen und das unterhaltsame Büroteilen.

. . . Björn Kolbeck, Henning Riedesel, Artur Galstyan und Florian Krull
für die Hilfe bei Computerproblemen und die Betreuung des Rechner-Clusters.

. . . Frank Müh und El-Amine Madjet für die gute Zusammenarbeit.

. . . alle MitarbeiterInnen der AG Knapp / Renger für die angenehme Arbeitsatmosphäre.

Finanziert durch:

Die Deutsche Forschungsgemeinschaft,
Sonderforschungsbereich 498.